# COMPUTATIONAL STUDIES OF ENVIRONMENTALLY IMPORTANT PROCESSES AT AQUEOUS INTERFACES

by

SHACHAR SHAMAY

A DISSERTATION

Presented to the Department of Chemistry
and the Graduate School of the University of Oregon
in partial fulfillment of the requirements
for the degree of
Doctor of Philosophy

March 2012

# DISSERTATION APPROVAL PAGE

Student: Shachar Shamay

Title: Computational Studies of Environmentally Important Processes at Aqueous Interfaces

This dissertation has been accepted and approved in partial fulfillment of the requirements for the Doctor of Philosophy degree in the Department of Chemistry by:

| | |
|---|---|
| Dr. Mark Lonergan | Chair |
| Dr. Geraldine Richmond | Advisor |
| Dr. Jeffrey Cina | Member |
| Dr. Marina Guenza | Member |
| Dr. Miriam Deutsch | Outside Member |

and

| | |
|---|---|
| Kimberly Andrews Espy | Vice President for Research & Innovation/ Dean of the Graduate School |

Original approval signatures are on file with the University of Oregon Graduate School.

Degree awarded March 2012

# DISSERTATION ABSTRACT

Shachar Shamay

Doctor of Philosophy

Department of Chemistry

March 2012

Title: Computational Studies of Environmentally Important Processes at Aqueous Interfaces

Undoubtedly, water is the most abundant and important molecular liquid and is likely the most necessary for life on Earth. The pursuit of understanding water's properties and behaviors has placed it in a unique scientific and even mythical position throughout human history. It is no surprise that much scientific research today centers around this molecule and its interactions with others. The interfacial region between liquid water solutions and other phases is still poorly understood, and only recently have experiments developed to where we can probe this unique environment. Water surfaces exist throughout the Earth's atmosphere and oceans but also make up many of the microscopic interfaces necessary for metabolic processes within living cells. Yet, the influence of water surfaces on the chemistry that drives life and terrestrial processes is still largely unknown, and many research efforts today are attempting to gain insight to this critically important frontier.

This dissertation documents several unique computational studies aimed to further our understanding of the complex interactions within a water system and between water and simple, common solutes. Reported herein are the results of molecular dynamics (MD) simulations and computational analysis of interfacial aqueous systems of small hydrated acids, ionic aqueous salt solutions interfaced with

a liquid oil, and gas molecules adsorbing onto water surfaces. The composition of the systems chosen for the studies reported in this dissertation reflect environmentally relevant interfaces and also complement recent experimental efforts by the Richmond laboratory. Classical and quantum ab initio MD techniques were used for simulation of the molecular systems, and the subsequent analyses provided new information regarding molecular interactions, geometries, orientations, and surface behaviors of water and hydrated interfacial solute molecules.

This dissertation includes both previously published and unpublished co-authored material.

## CURRICULUM VITAE

NAME OF AUTHOR: Shachar Shamay

GRADUATE AND UNDERGRADUATE SCHOOLS ATTENDED:
University of Oregon, Eugene, OR
California Polytechnic State University, San Luis Obispo, CA

DEGREES AWARDED:
Doctor of Philosophy in Chemistry, 2012, University of Oregon
Bachelor of Science in Chemistry, 2004, California Polytechnic State University, San Luis Obispo
Bachelor of Science in General Engineering, 2004, California Polytechnic State University, San Luis Obispo

AREAS OF SPECIAL INTEREST:
Computational Chemistry
Scientific Computing
High Performance Computing
Algorithm Design
Molecular Dynamics
Aqueous Surface and Interfaces

PROFESSIONAL EXPERIENCE:

Research Assistant, Richmond Research Group, Department of Chemistry, University of Oregon, Eugene, OR, 2005-2012

Visiting Researcher, Hore Research Group, Department of Chemistry, University of Victoria, B.C., 2008

Visiting Researcher, Parrinello Research Group, USI-Campus, Lugano, Switzerland, 2006

Engineer, Channel Islands Opto-Mechanical Engineering, Inc., Ventura, CA, 2004-2005

Undergraduate Research Fellow, Thermodynamics and Kinetics Group, NIST, Gaithersberg, MD, 2004

Research Assistant, Gragson Research Group, Calpoly, SLO, 2003-2004

## GRANTS, AWARDS AND HONORS:

GK12 Graduate Outreach Fellowship, University of Oregon, Eugene, OR, 2009-2011

IGERT International Travel Grant, USI-Campus, Lugano, Switzerland, 2006

Chemistry Student of the Year, Calpoly, SLO, 2004

Physical Chemistry Student of the Year, Calpoly, SLO, 2004

## PUBLICATIONS:

**E. S. Shamay**, K. E. Johnson, and G. L. Richmond. **Dancing on water: The choreography of sulfur dioxide adsorption to aqueous surfaces.** *Journal of Physical Chemistry C*, 115:25304-25314, November **2011**.

**E. S. Shamay** and G. L. Richmond. **Ionic disruption of the liquid-liquid interface.** *Journal of Physical Chemistry C*, 114(29):12590-12597, July **2010**.

**E. S. Shamay**, V. Buch, M. Parrinello, and G. L. Richmond. **At the water's edge: Nitric acid as a weak acid.** *Journal of the American Chemical Society*, 129(43):12910-12911, October **2007**.

# ACKNOWLEDGEMENTS

This journey ends far from where it began. My foundation and support, my wife Batya, brought me through the long periods of quiet, and the brief moments of terror, with love and grace. Our son, Ira, was my wellspring of motivation long before he arrived, and without my knowing it. We now set off, b'yachad, as a family, bringing new meaning to happiness, love, dedication. I love you both, and my work is always for you.

*And I watch my words from a long way off*
*They are more yours than mine*

Pablo Neruda, *So That You Will Hear Me*

To my parents I owe the deepest gratitude for their years of support. Their unique perspectives on life give me constant challenge to re-evaluate my thoughts and actions, and inevitably I grow, flourish, and live mindfully, present, and learning. Their little mensch is thankful for all they've done, and the struggles they overcame to make our family thrive.

I would like to thank all the mentors and teachers that have helped shape my scientific and personal lives both formally and informally. Derek Gragson, my undergraduate teacher and advisor, led me into my graduate program, and had faith in me as a scientist and student before I found it on my own. Dr. Victoria Buch shaped my career as a computational scientist and world traveler more than any other colleague during the brief months we worked together in the Swiss labs of Dr. Michelle Parrinello. Dr. Dennis Hore was a friend and teacher to me in Eugene, and a wonderful host and collaborator at his lab in Victoria. Dr. Fred Moore graced me with his humor, knowledge, attention to detail, drive, and endless assistance with editing. Dr. Kevin Johnson and his students were pivotal in the work on publications listed herein, and I thank him for his patience, dedication, and friendship.

Spending much of my time writing or hacking code in a cafe, at home, or out of town, I was often absent from the lab. However, I'm thankful to the Richmond lab members, past and present, for their motivation and comraderie during our times together.

I thank Geri for guidance and attitude, support and wisdom. She gave me the freedom to accomplish, the direction to produce, and the support to take for myself the opportunities that defined my graduate career, and my life.

Always for Batya and Ira

TABLE OF CONTENTS

Chapter Page

I. INTRODUCTION . . . . . . . . . . . . . . . . . . . . . . . . . . . . . 1

II. NITRIC ACID BEHAVIOR ON A WATER SURFACE . . . . . . . . . . 6

2.1. Introduction . . . . . . . . . . . . . . . . . . . . . . . . . . . . 6
2.2. Computational Methods . . . . . . . . . . . . . . . . . . . . . . 8
2.3. Nitric Acid Surface Dissociation Behavior . . . . . . . . . . . . 8
2.4. Summary . . . . . . . . . . . . . . . . . . . . . . . . . . . . . 11

III. IONIC DISTURBANCE OF THE OIL-WATER INTERFACE . . . . . 13

3.1. Introduction . . . . . . . . . . . . . . . . . . . . . . . . . . . . 13
3.2. Computational Method . . . . . . . . . . . . . . . . . . . . . . 19
3.3. Component Densities . . . . . . . . . . . . . . . . . . . . . . . 21
3.4. Water Orientation . . . . . . . . . . . . . . . . . . . . . . . . . 26
3.5. Calculated Sum-Frequency Spectra . . . . . . . . . . . . . . . . 32
3.6. Summary . . . . . . . . . . . . . . . . . . . . . . . . . . . . . 35

IV. SULFUR DIOXIDE ADSORPTION TO AQUEOUS SURFACES . . . 38

4.1. Introduction . . . . . . . . . . . . . . . . . . . . . . . . . . . . 38

4.2. Computational Approach . . . . . . . . . . . . . . . . . . . . . . 41
4.3. Surface Density Distributions . . . . . . . . . . . . . . . . . . . . 48
4.4. Equilibrium Simulations of Adsorbed $SO_2$ . . . . . . . . . . . . 50
4.5. Steered MD Transit Simulations of Adsorbing $SO_2$ . . . . . . . 57
4.6. Summary . . . . . . . . . . . . . . . . . . . . . . . . . . . . . 60

V. SULFUR DIOXIDE SURFACE HYDRATION BEHAVIOR . . . . . . 64

5.1. Introduction . . . . . . . . . . . . . . . . . . . . . . . . . . . . 64
5.2. Computational Methods . . . . . . . . . . . . . . . . . . . . . . 72
5.3. Sulfur Dioxide Bonding Coordinations . . . . . . . . . . . . . . . 73
5.4. Cyclic $SO_2$ Hydrate Structures . . . . . . . . . . . . . . . . . . 84
5.5. Summary . . . . . . . . . . . . . . . . . . . . . . . . . . . . . 91

VI. DICARBOXYLIC ACID ON A WATER SURFACE . . . . . . . . . . . 95

6.1. Introduction . . . . . . . . . . . . . . . . . . . . . . . . . . . . 95
6.2. Experimental Methods . . . . . . . . . . . . . . . . . . . . . . . 98
6.3. Computational Methods . . . . . . . . . . . . . . . . . . . . . . 102
6.4. Spectroscopic Response of Carboxylic Acid . . . . . . . . . . . . 103
6.5. Malonic Acid Orientation . . . . . . . . . . . . . . . . . . . . . . 115
6.6. Summary . . . . . . . . . . . . . . . . . . . . . . . . . . . . . 126

Chapter Page

VII. MALONIC ACID CONFORMERS AND HYDRATION . . . . . . . . . 129

7.1. Introduction . . . . . . . . . . . . . . . . . . . . . . . . . . . . 129

7.2. Computational Methods . . . . . . . . . . . . . . . . . . . . . 132

7.3. Hydration Structure . . . . . . . . . . . . . . . . . . . . . . . . 133

7.4. Bond Lengths . . . . . . . . . . . . . . . . . . . . . . . . . . . . 134

7.5. Molecular Orientation . . . . . . . . . . . . . . . . . . . . . . . 140

7.6. Bond Spectra . . . . . . . . . . . . . . . . . . . . . . . . . . . . 149

7.7. Summary . . . . . . . . . . . . . . . . . . . . . . . . . . . . . . 152

VIII. CONCLUSIONS . . . . . . . . . . . . . . . . . . . . . . . . . 155

APPENDIX: HETERODYNE DETECTED SFG . . . . . . . . . . . . . . . . 158

REFERENCES CITED . . . . . . . . . . . . . . . . . . . . . . . . . . 161

# LIST OF FIGURES

Figure Page

2.1. Snapshot of initial bonding configurations of $HNO_3$ molecules. $HNO_3$ molecular plane containing the three NO bonds was initially placed (left) perpendicular to the surface, and (right) with its molecular plane initially parallel to the water surface plane. . . . . 7

2.2. (red) $HNO_3$ OH bond length trajectories and (blue, black) the unprotonated NO bondlengths during a dissociation event in a bulk water system. . . . . . . . . . . . . . . . . . . . . . . . . . . . . . 9

2.3. Nitric acid proton excursions and a near-dissociation event. (red dashed) Distances from the proton to the nearest water-oxygen and (black solid) the nitric acid OH bond length. . . . . . . . . . . . . . . . . . 11

3.1. Angles used to define molecular orientation of $H_2O$. . . . . . . . . . . . 16

3.2. Aqueous salt solution (1.2 M) and $CCl_4$ surface density profiles. (A) Neat-$CCl_4$-$H_2O$, (B) NaCl, (C) $NaNO_3$, and (D) $Na_2SO_4$ aqueous solution densities and the (solid black) fitted lineshape. (dashed blue) The $CCl_4$, (dashed green, 10x) $Na^+$ cation, and (scaled 5x) respective anion densities. . . . . . . . . . . . . . . . . . . . . . . . . . . . . 22

3.3. Orientation profiles of interfacial water molecules at different depths from the GDS. (left) Molecular bisector and (right) molecular planar normal profiles. Neat-$CCl_4$-$H_2O$, NaCl, $NaNO_3$, and $Na_2SO_4$ system water orientation profiles top to bottom row, respectively. . . . . . 27

3.4. Depictions of water orientation ranges spanning values of $\theta$ and $\phi$. Ranges of $\theta$ are (A) $0 < \cos\theta < 1$, (B) $0.7 < \cos\theta < 1$, (C) $-0.5 < \cos\theta < 0.5$. (D) The $\phi$ range of $0.7 < \cos\phi < 1$. . . . . . . . 29

3.5. Vibrational SFG spectra of the water-OH stretching region for each interfacial aqueous-salt-$CCl_4$ system. (black-dashed) The reference $CCl_4$-$H_2O$ interface spectrum. Insets are reproductions of the experimental spectra ($\chi^{(2)}_{eff}$) from McFearin et al.[1] . . . . . . . . . 33

4.1. Sample starting configurations for the (left) neat-water and (right) saturated SMD simulations. . . . . . . . . . . . . . . . . . . . . . . . 44

4.2. (A) Density profiles of $H_2O$ (Gray) and $SO_2$ (red) from a 10 ns simulation of the neat-water system with a single $SO_2$. (B) The instantaneous location of the outer $H_2O$ monolayer for each simulation time step (blue), and the surface location extracted from the density fitting (horizontal dashed line). . . . . . . . . . . . . . . . . . . . . . . . . 46

4.3. Definition of molecular body-fixed axes for the two $C_{2v}$ molecules: $SO_2$ and $H_2O$. . . . . . . . . . . . . . . . . . . . . . . . . . . . . 48

4.4. (A) The definition of the molecular orientation angles $\theta$ and $\phi$. (B) $\theta$, the bisector "tilt" angle, (C) $\phi$, the bisector "twist" angle. . . . . . 49

4.5. Density distributions of (black) $H_2O$ and (red) $SO_2$ (neat-water system on left scaled 10x, saturated on right) near a water surface. . . . . . 49

4.6. Molecular orientation histograms of $H_2O$ throughout the surface equilibrated systems at various depths. . . . . . . . . . . . . . . . 52

4.7. Molecular orientation distributions for $SO_2$ molecules adsorbed to the water slab surface. . . . . . . . . . . . . . . . . . . . . . . . . . 53

4.8. Molecular orientation distributions of an $SO_2$ at different interfacial depths of an aqueous slab during SMD transit simulations. . . . . . 58

4.9. Proposed orientations of $H_2O$ and $SO_2$ in the regions near the (A) neat-water and (B) saturated liquid-gas interface. . . . . . . . . . . . . . 63

5.1. Example cyclic $SO_2$ hydrate structure, formed by the covalent, S-O, and hydrogen bonds of the two molecule types. . . . . . . . . . . . . . . 69

5.2. $SO_2$ in various cyclic hydrate structures encountered during MD simulations with water. . . . . . . . . . . . . . . . . . . . . . . . . . . 71

5.3. Two conformations of Type III $SO_2$ cyclic hydrate structures. . . . . . 72

5.4. The distribution of bonding coordinations of the (blue) cold and (red) hot $SO_2$. . . . . . . . . . . . . . . . . . . . . . . . . . . . . . . . . 74

5.5. RDFs of (blue) cold and (green) hot simulations. (left) $S_{SO_2}$–$O_{H_2O}$, and (right) $O_{SO_2}$–$H_{H_2O}$. . . . . . . . . . . . . . . . . . . . . . . . . . . 78

5.6. A graph of the $SO_2$ bonding coordinations showing (directed edges) the number of times the coordination transition occurred. . . . . . . . . 80

5.7. Time $SO_2$ spent in each bonding coordination. The total amount of consecutive timesteps in a coordination corresponds to the vertical position along the lifespan axis, in ps. . . . . . . . . . . . . . . . . . 82

Figure Page

5.8. Different $SO_2$ cyclic hydrate structures (up to 4 waters), and occurrence rates as a percentage of total simulation time. . . . . . . . . . . . . 85

5.9. (dashed black) A cyclic $SO_2$ hydrate formation time function, $C(t)$, (red) a smoothed $C_s(t)$, (green) the debounced cycle formation function, $f(t)$. . . . . . . . . . . . . . . . . . . . . . . . . . . . . . . . . . . 89

5.10. Cyclic $SO_2$ hydrate structure lifetimes of (blue) cold and (red) hot simulations. . . . . . . . . . . . . . . . . . . . . . . . . . . . . . . . 91

6.1. VSFS-SSP spectra of the carboxylic C=O of aqueous malonic acid at concentrations of 0.1 M, 0.5 M, 1 M, and 3 M. . . . . . . . . . . . . 105

6.2. VSFS-SPS spectra of carboxylic C=O of aqueous malonic acid at 1 M, 3.5 M, and 4.5 M. . . . . . . . . . . . . . . . . . . . . . . . . . . . 107

6.3. VSFS of water/CH region for 0.1 M, 1 M, and 3.5 M aqueous malonic acid. The gray spectra are neat water. . . . . . . . . . . . . . . . . 109

6.4. Plot of malonic acid concentration vs fitted VSFS amplitudes (left axis) and surface tension (right axis). . . . . . . . . . . . . . . . . . . . . 111

6.5. VSFS-SSP spectra of carboxylic C=O of aqueous malonic acid at 1 M with bulk adjusted pH values from native (top) to >8 (bottom). The spectra are offset for clarity. . . . . . . . . . . . . . . . . . . . . . . 113

6.6. VSFS-SPS spectra of carboxylic C=O of aqueous malonic acid at 1 M with bulk adjusted pH values from native (top) to 6 (bottom). The spectra are offset for clarity. . . . . . . . . . . . . . . . . . . . . . . 114

6.7. Plot of fitted VSFS amplitude vs surface pressure for bulk adjusted pH 1M malonic acid. . . . . . . . . . . . . . . . . . . . . . . . . . . . . 116

6.8. Definitions of the angles used to orient malonic acid molecules in space, (left) $\theta$ and $\phi$, and (right) internally, $\psi$. . . . . . . . . . . . . . . . 118

6.9. Bivariate distributions of the "tilt" and "twist" of the malonic acid carbon chain at different interfacial depths. . . . . . . . . . . . . . . 120

6.10. Bivariate orientation distributions of the two internal dihedral angles of malonic acid. . . . . . . . . . . . . . . . . . . . . . . . . . . . . . 123

6.11. Orientational depth profile of malonic acid carbonyl C=O tilt angle, $\theta_{C=O}$, plotted against the molecular center of mass position. . . . . 125

7.1. RDFs of malonic acid oxygens and water hydrogens. . . . . . . . . . 134

Figure Page

7.2. Bond trajectories of malonic acid intramolecular distances between the acid (green and dark blue) O-H distances, and (light blue and red) protons and carbonyl oxygens on the opposite ends of the molecule. (top) an example of an IHB bond trajectory, and (bottom) an IUB trajectory. . . . . . . . . . . . . . . . . . . . . . . . . . . . . . . 135

7.3. Two conformations of malonic acid encountered during simulation. (left) IUB and (right) IHB conformations. . . . . . . . . . . . . . . . . . 136

7.4. Distributions of inter-atomic distances for the O-H and $O_{carb}$-$H_{acid}$ bonds, and also for the two carbonyl C=O bonds of each malonic acid. (top) IUB, (bottom) IHB. (insets) expanded regions of the two alcohol O-H, and carbonyl C=O bondlengths. . . . . . . . . 138

7.5. Average inter-atomic distances (i.e. bondlengths) between various pairs of atoms in malonic acid, and their standard deviations. . . . . . . 140

7.6. Intensity plots of the bivariate distributions of the two carbon group angles, $\theta$ and $\phi$. (right) plots of the contributions from the (top) IUB and (bottom) IHB malonic acids. . . . . . . . . . . . . . . . 142

7.7. Intensity plots of the bivariate $\psi$-$\psi$ distribution of the two malonic acid O=C-C-C dihedral angles. . . . . . . . . . . . . . . . . . . . . . 145

7.8. The tilt angle, $\theta_{C=O}$, of the two carbonyl C=O bonds of malonic acid (black) for all simulations, (blue) for IUB simulations, (red) IHB simulations. . . . . . . . . . . . . . . . . . . . . . . . . . . . . . . 147

7.9. Vibrational power spectra of the carbonyl C=O bond trajectories with (inset) experimental results. . . . . . . . . . . . . . . . . . . . . . . 150

# LIST OF TABLES

Table Page

3.1. Aqueous molecule and ion numbers. Listed are the populations of each component for the 4 simulated aqueous phases. All systems were simulated at near 1.2 M salt concentrations. . . . . . . . . . . . . . . 20

3.2. Aqueous salt system density parameters. . . . . . . . . . . . . . . . . . . . 22

# CHAPTER I

# INTRODUCTION

To the lay person's eye peering in on modern scientific research there would be a surprising amount of activity in the study of water. To many, this most abundant and simple molecular liquid is part of the mundane. For chemists, water is still poorly understood, and many questions remain regarding properties of aqueous systems, and water's interesting bonding behaviors. This simple, triatomic molecule still holds secrets that drive the state-of-the-art in scientific research. The full nature of even the most simple neat-water system has not yet been captured, and certainly less is known about more interesting systems with many added constituents and phase boundaries. This dissertation is a compilation of several research projects executed to gain knowledge about water's interactions with other simple, environmentally relevant molecules at the region of the water surface.

Unlike the bulk of aqueous solutions, the water surface is a dynamic frontier between two phases where orientational isotropy is broken, and the formation of unique electric field conditions dominate molecular interactions. The interfacial liquid region functions as a "black-box" doorway where solute adsorption, hydration, chemical reactions, and absorption take place. These mysterious liquid surfaces are the foundations of numerous processes underlying chemistry ranging from metabolic pathways to atmospheric reactions. Each of the computational studies documented herein were formed to further our understanding of environmentally and anthropogenically important interfacial systems. The research presented was carried out computationally, making use of molecular dynamics (MD) simulations of liquid surface regions.

From their humble beginnings only half a century ago, computational simulations have developed rapidly in scale and complexity. Scientific experiments, once reserved for laboratories and apparatus, are now being conducted more often *in silico* (i.e. via computational methods). Molecular dynamics and computational modeling have become invaluable tools for the chemist and physicist; they have even begun replacing complex and expensive physical experiments, and are now probing phenomena that are otherwise impossible to capture in a physical laboratory. This dissertation documents a series of computational studies of solute and solvent behavior in aqueous systems using molecular dynamics simulations. A complete introduction to molecular dynamics and molecular modeling techniques is beyond the scope of this dissertation, but several recent publications are available for one's own edification.[2–9]

MD simulation is a well established technique with a multitude of packaged software options for carrying out the complex calculations involved. Two methods of simulation were used in the research of this dissertation to model aqueous systems with added constituents: 1) classical MD simulations using empirical or semi-empirical interaction potentials, and 2) ab initio MD using DFT (DFT-MD) calculations and quantum interaction potentials. All of the simulations were performed using either the Amber 11 MD package (classical interaction potential),[10, 11] or the CP2K ab initio MD package (DFT potential).[12, 13] These simulation software suites facilitate most of the process involved in defining and running MD simulations, freeing researchers to pursue the physical analysis of the simulated systems without requiring further software development for MD.

The first system reported in Chapter II is that of a nitric acid molecule bound to a neat-water surface.[14] This was the first ab initio MD project undertaken by the Richmond laboratory, and was co-authored with Drs. Victoria Buch and Michele

Parrinello. The textbook definition of nitric acid as a strong acid was challenged by looking at its behavior in the interfacial water region that classroom chemistry experiments do not access. This work introduces the concepts involved in analyzing the protonation state of an acid from MD data, and takes a first look at the hydration of solute molecules adsorbed to a water surface.

Soon after the first computational study of surface $HNO_3$ was completed, a second project making use of classical MD simulations was undertaken on the more complex liquid-liquid $H_2O$-$CCl_4$ interfacial region, documented in Chapter III.[15] This work is published and co-authored with Dr. Geraldine Richmond. Various sodium halide salts were introduced into the aqueous phase of a water system adjacent to a $CCl_4$ phase. The simulated conditions were set to complement those used in the experimental work that was performed previously by Catherine McFearin in the same laboratory.[1] The unique double-layering behavior of the salts is reported through the use of density profiling. Additionally, the molecular orientation of interfacial water interacting with the $CCl_4$ in the presence of different salts is analyzed. Lastly, the vibrational sum frequency (VSF) spectra of the interfacial water molecules is computed and presented as a link to, and further verification of the experimental results and conclusions.

Two computational studies were initiated to complement a series of experiments in the Richmond laboratory to study the adsorption behavior of $SO_2$ on a water surface.[16–18] The first simulation study, documented in Chapter IV, made use of a classical interaction potential and a unique steered MD (SMD) technique to describe the adsorption process of a gaseous $SO_2$ as it first makes contact with a water surface.[19] The orientations of both the adsorbing $SO_2$ and the surface waters were described throughout the gaseous adsorption MD trajectory to understand how each molecule reacts to the movements of incoming gas molecules. The work was produced in collaboration with Dr. Kevin E. Johnson of Pacific University during his sabbatical time with the Richmond laboratory. A follow-up study of $SO_2$ made use of DFT-MD simulations to further characterize a surface-bound $SO_2$ molecule, and is reported in Chapter V.[20] This work was co-authored with Dr. Geraldine Richmond. The DFT-MD calculates molecular geometries and energies more accurately, but is more computationally intensive. A series of simulations and analyses probed the orientations and interactions of $SO_2$ with water. Additionally, a unique cyclic hydrate structure was discovered and first reported in the study, as well as a novel graph-theoretical technique for analyzing the interconnectedness of the hydrate structures formed throughout the simulations.

The final studies documented in this dissertation examine the nature of small dicarboxylic acid molecules at an aqueous surface. In the first study, documented in Chapter VI, classical MD simulations were performed in tandem with VSF spectroscopic experiments of malonic acid solutions.[21] That work took a first look at the surface behavior of malonic acid, a small dicarboxylic acid of environmental importance. Patrick Blower and Stephanie Ota are co-authors that contributed experimental results that paralleled the simulations of the same systems. The second project detailed in Chapter VII was solely a computational one, using ab initio MD simulations of small water clusters with a surface-bound malonic acid.[22] This follow-up study, co-authored with Dr. Geraldine Richmond, verifies the classical force field parameters and resulting geometries of the first malonic acid study, and further examines the microscopic hydration structures, geometries, and unique internal bonding conformations of malonic acid bound to water.

Water surfaces are as important as they are abundant. Our understanding of the interactions between water and other environmental molecules remains mostly undeveloped, and the nature of interfacial chemistry is still poorly understood. The projects and results presented herein advance our understanding of some simple, yet fundamental and environmentally relevant aqueous systems. Using MD simulations and computational analysis, many properties of surface-bound solutes are elucidated. The results of these studies help build the scientific foundations of the surface science necessary to make analysis of more complex systems possible in future work.

# CHAPTER II

# NITRIC ACID BEHAVIOR ON A WATER SURFACE

This work was published in volume 129(43) of the Journal of the American Chemical Society in October 2007. Dr. Victoria Buch initially defined the simulated system, aided greatly with the computational setup of the CP2K simulation package, and provided guidance in programming and editing of the final manuscript.[12, 13] Dr. Michele Parrinello contributed computational resources and laboratory facilities at the Universit della Svizzera Italiana, in Lugano, Switzerland. Eric Shamay was the principle investigator for this work.

## 2.1. Introduction

Nitric acid plays a key role in many important heterogeneous chemical reactions in our upper and lower atmosphere.[23] At the surface of aerosols and cloud droplets it has the opportunity to inflict its highly reactive nature on a host of organic and inorganic species.[24] But how applicable is our knowledge of nitric acid in solution to predicting its behavior at an aqueous surface? This chapter reports the distinctly different behavior of nitric acid on a water surface relative to its bonding and acidic behavior in bulk water. It was found through molecular dynamics calculations that nitric acid orients and bonds to a water surface in a way that reduces its ability to be a strong dissociating acid. Altered hydrogen bonding to surface water molecules plays a key role in this molecular behavior. The results throw into question how we should think about the reactivity of nitric acid on aqueous surfaces if we rely on models solely derived from its behavior in bulk.

Recent computational,[25, 26] and experimental[27–32] studies have suggested that molecular nitric acid and nitrate anion can be found at or below an aqueous surface, but there were uncertainties from these as to the bonding and orientation of the molecular form. Reported here is confirmation by simulation of the altered bonding of surface nitric acid. In these simulations nitric acid molecules were introduced to the surface in the two different orientations shown in Figure 2.1.: with the molecular plane perpendicular and the other parallel to the surface. Many characteristics of nitric acid were investigated, including molecular orientation (defined by the tilt angle between the vector normal to the molecular plane of the nitric acid containing the three NO bonds, and the interface normal), $HNO_3$ coordination to solvating water molecules, OH-bond and NO-bond lengths, and the acid distances to solvating water molecules. Comparison was carried out of the behavior of the nitric acid at the surface and in the bulk solution.

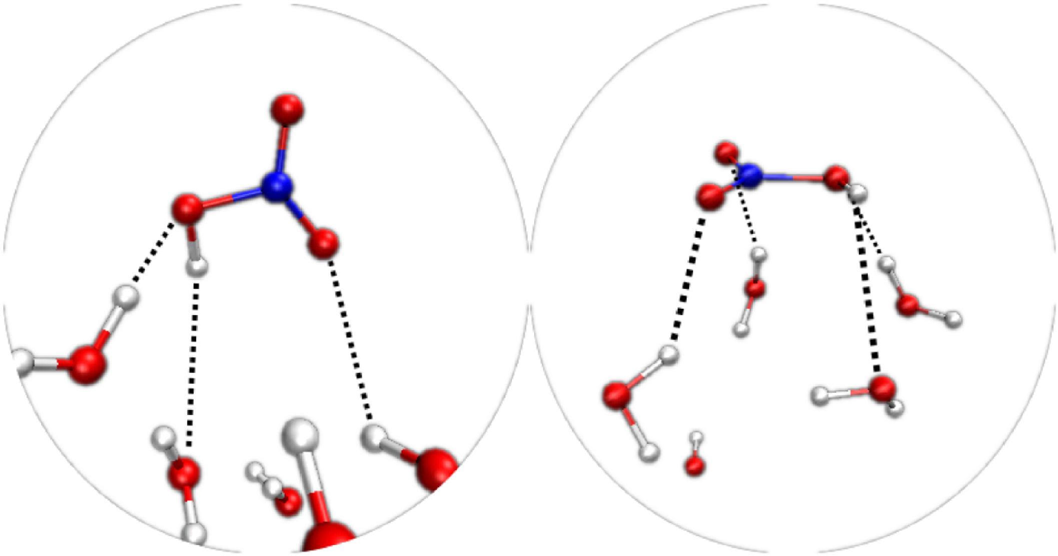

FIGURE 2.1. Snapshot of initial bonding configurations of $HNO_3$ molecules. $HNO_3$ molecular plane containing the three NO bonds was initially placed (left) perpendicular to the surface, and (right) with its molecular plane initially parallel to the water surface plane.

## 2.2. Computational Methods

Ab initio molecular dynamics simulations were performed using density functional theory (DFT)[13] with the help of the QUICKSTEP package.[12] Energies and forces corresponding to the system Born-Oppenheimer surface were calculated for each MD step using the atom pseudo-potentials of the Goedecker, Teter, and Hutter type,[33] the exchange-correlation functional of Becke, Lee, Yang and Parr (BLYP),[34] and a Gaussian valence basis set of double-$\zeta$ quality augmented by one set of polarization functions (DZVP). This technique follows the classical motion of the atomic nuclei in time, solving for quantum mechanical motion of electrons *ab initio*. A simulation time step of 1.0 fs was used. A starting point was a periodic box with 64 water molecules. To simulate the bulk solution, two water molecules were replaced by an acid molecule. To generate the surface model, two dimensional periodic boundaries were set for the x and y axes of the water box. The resulting infinite slab model includes two open surfaces interfacing with the vacuum. An acid molecule was placed above one of them. Two "extreme" initial configurations were tested for the acid, with the molecular plane either parallel or perpendicular to the liquid surface, as shown in Figure 2.1. (trajectory I and II). The initial configurations were energy minimized and the systems were equilibrated for 0.5 ps. The two slab systems were then subjected to NVE simulations for a further 20 ps. The bulk system was simulated for 25 ps. The atomic position data were collected at every step.

## 2.3. Nitric Acid Surface Dissociation Behavior

The simulations show that dissociation of the nitric acid in the bulk solution happens very readily just after the equilibration period, consistent with its known high degree of acidity. As shown in Figure 2.2., $HNO_3$ initially placed in the interior of the slab dissociates within 800 fs of simulation time as evidenced by the abrupt lengthening and dissociation of the OH bond. Coincident with the dissociation is the lengthening of the two unprotonated NO bonds. Prior to dissociation, the acid molecule forms two strong H-bonds through the oxygens (primarily the $NO_2$ moiety), and one to water via the proton, with a total of three strong H-bonds. In contrast, a single nitric acid molecule placed on the surface of a neat water slab did not dissociate over the full simulation time and typically formed one strong H-bond to the water phase through the proton, and occasionally a second strong bond via NO (see Supplement).

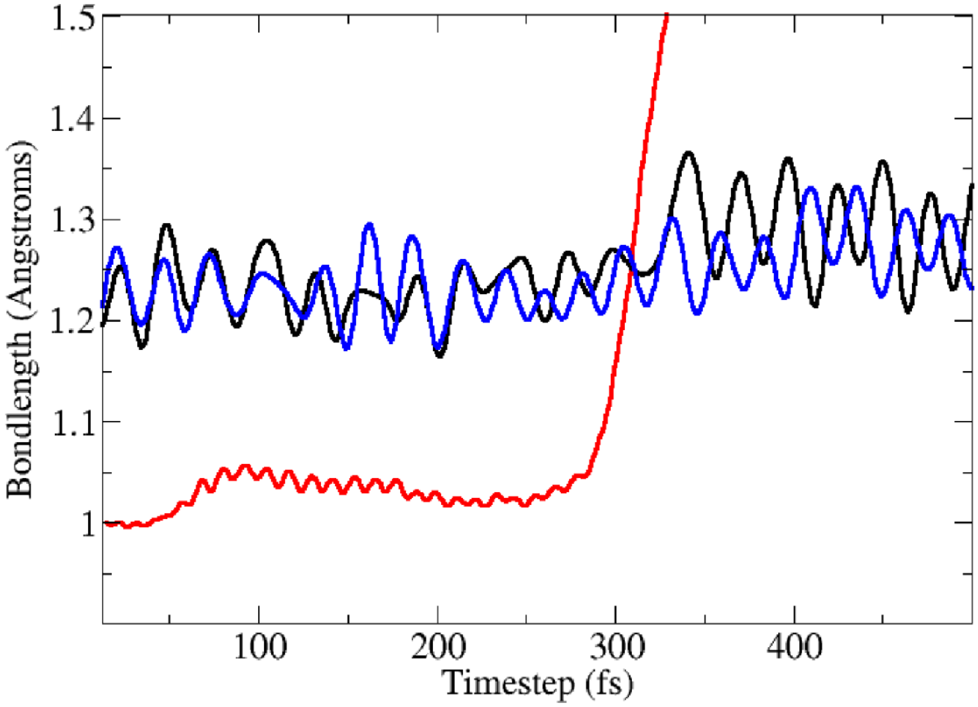

FIGURE 2.2. (red) $HNO_3$ OH bond length trajectories and (blue, black) the unprotonated NO bondlengths during a dissociation event in a bulk water system.

In trajectory I, one NO bond is pointing into the vacuum, and the NOH moiety and second NO bond are both directed into the aqueous phase. The molecular tilt angle oscillates about 90° with amplitude of 62° to either side. The three NO bonds have distinctly different characteristics. The NO pointing towards the vacuum phase shows no interaction with surface water molecules and consequently is the shortest of the three NO bonds at 1.21 Å. The submerged NO (1.24 Å) interacts weakly with water, with O..H distance distribution peaking at 2.24 Å. The H-bond of acid hydrogen to water oxygen appears relatively strong, with H..O distance peaking at 1.87 Å (as compared to 1.74 Å for water-water bonds). The protonated NO bond is longer than the unprotonated ones at 1.51 Å, and the oxygen is only weakly Hbonded ¡ 25% of the trajectory. The OH bondlength remained at 1.01 Å. Although the surface acid forms H-bonds to the water phase, the solvation is insufficient to induce ionization. Past computational studies indicate that only fully solvated $HNO_3$ molecules in the bulk dissociate to ions.[35–37]

In trajectory II, the acid molecule oscillates close to the tilt angle of 0° with the surface normal, but occasionally flips on the surface. The $NO_2$ moiety is weakly H-bonded to water for 60% of the trajectory. The NO lengths were similar (1.22-1.23 Å) to the perpendicular configuration, but the protonated NO was slightly shorter at 1.43 Å. One observes several ultrafast incipient ionization events. The typical OH bond length was 1.01 Å, but during these approximately 50 fs excursions, the proton moves away to a distance of over 1.3 Å from the acid oxygen. It oscillates near an equidistant position with respect to a neighboring water oxygen without fully dissociating. Figure 2.3. shows a section of the surface molecule trajectory during one of these proton excursions. This behavior is indicative of a very strong H-bond through the proton.

These calculated results are consistent with a previous VSF study by the Richmond laboratory,[32] in that the surface molecule was found to bind strongly

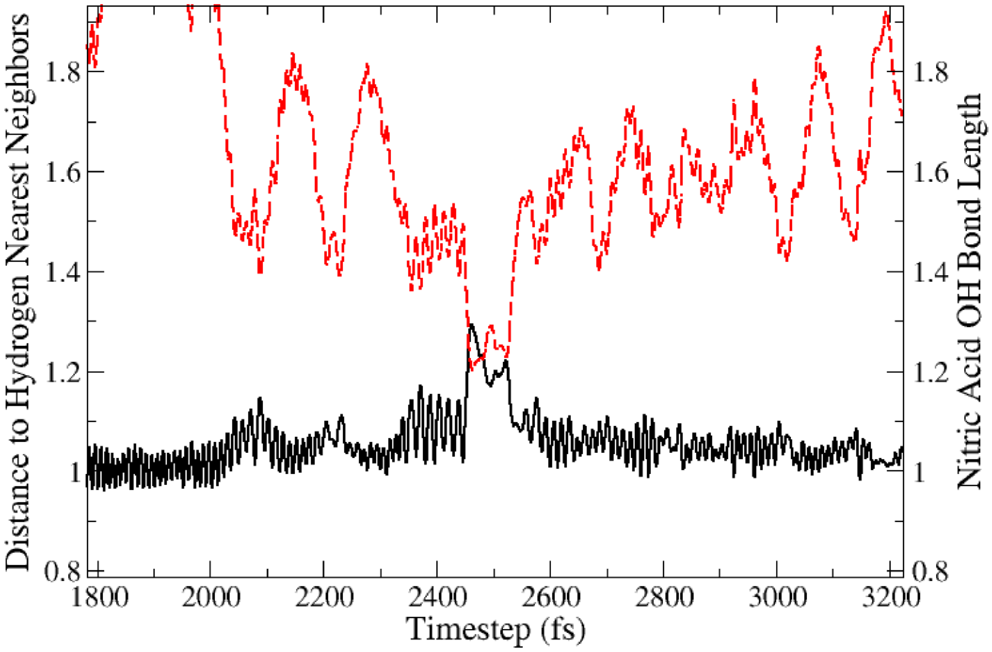

FIGURE 2.3. Nitric acid proton excursions and a near-dissociation event. (red dashed) Distances from the proton to the nearest water-oxygen and (black solid) the nitric acid OH bond length.

to a single water through the acid proton to form the monohydrate species. However, these calculations show varying degrees of weak bonding to the $NO_2$ that may not be observed experimentally through frequency shifts.

## 2.4. Summary

The implications of these results are wide ranging. The molecular nature of nitric acid at a water surface makes it more readily available for reactions with its ambient surroundings. However, this exposure also brings with it a dramatic change in its chemical propensity to dissociate. As the appreciation for the importance of heterogeneous surface reactions in the atmosphere and our environment continues to grow, so does our need to evaluate predictive models of such surface reactions that might be based on either gas phase or condensed phase reaction conditions.

A more complex aqueous system at an oil-water interface is examined in Chapter III. Sodium halide salts were introduced into an aqueous phase, and subsequent computational analysis was performed to determine the disrupting effect of ions on the surface water molecules and their intermolecular bonding.

# CHAPTER III

# IONIC DISTURBANCE OF THE OIL-WATER INTERFACE

This work was published in volume 114(29) of the Journal of Physical Chemistry C in July 2010. Dr. Geraldine Richmond supplied computational resources and project support. Eric Shamay was the principle investigator for this work.

## 3.1. Introduction

The most important biological and environmental processes depend on the nature of interfacial water molecules and dissolved ions in boundary layers. Only in recent years, and through the development of surface-specific experimental[38–40] and computational[41–43] analytical techniques, have we been able to begin understanding this complex environment comprised of interfacial water and ions. Over this time the field has advanced from studying simple water systems in vacuum and in air, to studying more complex interfaces such as aqueous solutions near a hydrophobic surface that are responsible for such important processes as ion transport, liquid-liquid extraction, drug delivery, and environmental remediation.

The computational studies presented herein have been conducted to gain a more precise molecular-level picture of how ions affect waters within a liquid-liquid interface. Molecular dynamics (MD) simulations allow us to look at the specific ion and water locations, geometries, and bonding environments within the interface region, unlike experimental techniques currently used for similar surface studies. Consequently, the work presented here is compared to conclusions from a recent experimental study that showed how ions affect the interfacial region between an aqueous ionic solution and a hydrophobic organic liquid.[1] Classical molecular dynamics simulations have been performed to analyze the interface formed between various aqueous salt solutions and the organic liquid carbon tetrachloride ($CCl_4$). Analyses were conducted to contrast the behavior of different aqueous salt solutions as well as for comparison with previous computational efforts.[44–49] Three salt solutions were simulated containing NaCl, $NaNO_3$, $Na_2SO_4$. These were chosen to show the effects of both atomic and molecular, as well as monovalent and divalent anions on the interfacial environment. The simulation data has been used here to extract ionic and molecular density data across organic interfaces, information about water orientation near the interfaces, and simulated SFG spectra.

### 3.1.1. Density Profiles

Density histograms of simulated interfaces have been used in previous publications to show ionic and molecular distribution behavior in various systems.[45, 47, 49–54] In this chapter the density profile of water throughout the interface is fit to a hyperbolic tangent function[53, 55] as shown below in Equation 3.1.:

$$\rho(z) = \frac{1}{2}(\rho_1 + \rho_2) - \frac{1}{2}\left(\rho_1 - \rho_2\right)\tanh\left(\frac{z - z_0}{d}\right) \qquad \text{(Equation 3.1.)}$$

Equation 3.1. relates the interfacial density, $\rho$, as a function of position, $z$, along a given system reference axis, to the densities of the phases, $\rho_1$ and $\rho_2$, on either side of the Gibb's dividing surface (GDS), $z_0$. The interfacial width, $d$, is related to the "90-10" thickness that is often reported by $t_{90-10} = 2.197d$.

These measures of interfacial thickness provide a means of comparing the depths to which the water phase is affected by ions located at the interface. The density distributions of the salts depict concentration and depletion phenomena throughout the interfacial region, and also serve to illustrate ionic surface affinity within this region. Previous work has been performed on the air-$H_2O$ interface with ions of different levels of interfacial affinity, with the more polar ions being the most interfacially active.[40, 54, 56–61] Presented in this chapter are the density distribution results for the neat $CCl_4$-$H_2O$ and salt solutions adjacent to an organic $CCl_4$ phase.

### 3.1.2. Molecular Orientation

Several methods have been used previously to show molecular orientation profiles of water molecules throughout simulated interfacial regions.[25, 43–45, 53, 62–65] Studies have utilized various internal coordinate definitions and a number of angle definitions, orientational order parameters, and probability distributions to relate molecular, or averaged, orientations. This chapter introduces the computations of the orientation of water using two vectors that intuitively describe the orientation in space, given the locations of the three atoms comprising the molecule. The molecular bisector, a vector that points along the axis of symmetry of the water molecule from the hydrogen-end to the oxygen, provides directional orientation similar to the water molecule's dipole. A second vector, that is referred to here as the molecular normal vector, is established as the vector pointing normal to the plane formed by the three atoms of the water molecule and establishes its planar "tilt". Analyzing the angle made between these two vectors and a given space-fixed reference axis (herein defined as the long-axis of the simulation cells, oriented perpendicular to the interfacial plane and pointing out of the aqueous phase) is a means of finding the orientation of waters within these simulated systems as illustrated in Figure 3.1. The angle formed between the molecular bisector and the reference axis will hereafter be referred to as $\theta$, and the angle between the reference axis and the molecular normal vector as $\phi$. The analysis in this chapter reports the cosines of these two angles, and because of the symmetry of the water molecule where the hydrogens are not uniquely identified, the cosines of the two angles are limited as follows: $-1 \leq \cos\theta \leq 1$ and $0 \leq \cos\phi \leq 1$. Reported here are the orientation profiles of $\theta$ and $\phi$ as functions of the distance from the GDS of the interface, as found from the fitting in the density profile analyses.

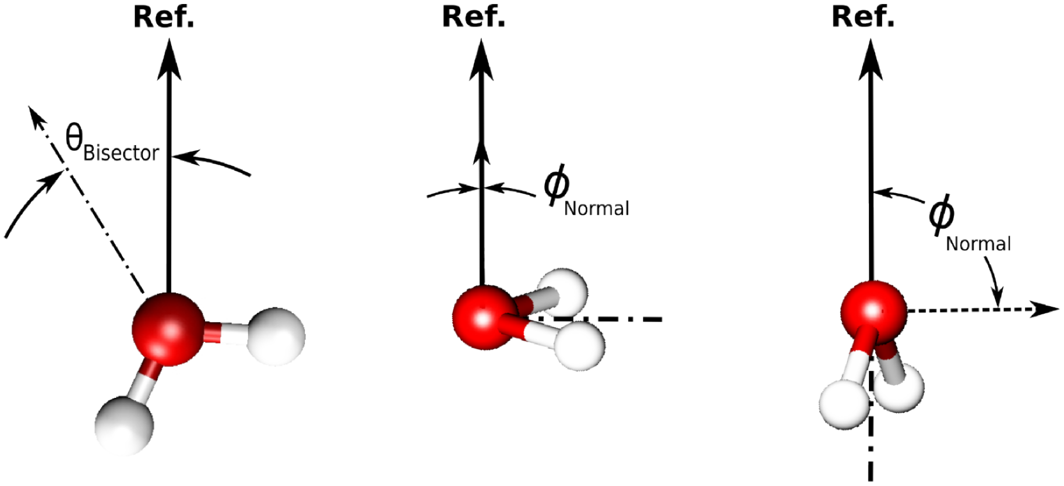

FIGURE 3.1. Angles used to define molecular orientation of $H_2O$.

### 3.1.3. Computational SFG

A difficult challenge for experimental surface studies is in understanding the vibrational spectroscopy of liquid water. Hydrogen bonding between water molecules causes inter- and intramolecular couplings that lead to broad spectral envelopes, each containing a distribution of water-bonded species. Simulations provide the analytical capacity to relate the broad lineshapes, and the often difficult-to-assess impact of hydrogen bonding as a function of OH vibrational frequency, to microscopic geometries, forces, and environments. In this chapter SFG spectra are computed of the interface between the salt solutions and an organic phase to compare with the experimental results of similar systems.[1] More recent developments in SFG experiments have led to heterodyne-detected methods (HD-VSFG) that capture phase and sign of the $\chi^{(2)}$ response. Water models developed specifically for the computation of SFG signals from MD data have also improved and now provide a near-quantitative match with the experimental results. These developments are being explored in many surface systems. The HD-VSFG technique, its computational counterpart, and recent developments to water models are discussed further in the appendix.

The computational method used here is based on that of Morita and Hynes[66] as outlined in a previous study by the Richmond laboratory utilizing the same technique.[67] The computational SFG technique has been improved in more recent studies by Morita et al.[68, 69] by their use of an improved water model and use of time-dependent calculations. The technique used here matches qualitatively the experimental spectra to a sufficient degree, and qualified conclusions about lineshape and intensity are made. The fundamental computations are described briefly below:

Water's OH vibrational frequencies in the gas-phase are $3657\,cm^{-1}$ and $3756\,cm^{-1}$. The uncoupled frequency of the gas-phase OH vibrations is $\omega_{gas} = 3706.5\,cm^{-1}$, with an intramolecular coupling constant of $V_{12} = 49.5\,cm^{-1}$. By expanding the simple spring oscillator force model to include the first anharmonicity, the vibrational frequency as a function of solvation can be by Equation 3.2.

$$(\omega_{gas} - \omega) = \Delta\omega \approx \left(\frac{k_0}{m}\right)^{1/2} \left(\frac{l_0 F}{2k_0^2}\right) \qquad \text{(Equation 3.2.)}$$

in Equation 3.2. $k_0$ and $l_0$ are the harmonic and anharmonic force constants, respectively, and $m$ is the reduced mass of the OH. $F$ represents the force acting on the center of mass of the OH, output from the MD simulation data. The two-state eigenvalue equation is solved with the two uncoupled frequency shift values to determine lower and upper energies of water. The eigenvectors, $C_1$ and $C_2$, are defined in Equation 3.3.

$$\begin{bmatrix} \Delta\omega_1 & V_{12} \\ V_{12} & \Delta\omega_2 \end{bmatrix} \begin{bmatrix} C_1 \\ C_2 \end{bmatrix} = 0 \qquad \text{(Equation 3.3.)}$$

In similar environments, each OH of a water molecule will contribute equally towards both eigenstates resulting in symmetric and antisymmetric OH vibrational stretch modes. Application of perturbation theory and the electric dipole approximation to the lorentzian distribution for a given OH vibrational energy state results in an equation for the molecular hyperpolarizability, as in Equation 3.4.

$$\beta^{(2)}_{pqr,\nu} = \frac{\langle g|\alpha_{pq}|\nu\rangle\langle\nu|\mu_r|g\rangle}{\omega_\nu - \omega_{IR} - i\Gamma_\nu} \qquad \text{(Equation 3.4.)}$$

$\langle\nu|\mu_r|g\rangle$ represents the infrared transition from ground state to an OH vibrational state, and $\langle g|\alpha_{pq}|\nu\rangle$ is the Raman polarizability transition from a vibrational state back to ground for an OH vibrational mode of water with a frequency of $\omega_\nu$, a natural line-width of $\Gamma_\nu$, in a frame defined by the coordinates $pqr$.

By applying the harmonic oscillator approximation to Equation 3.4., the equation for the hyperpolarizability is transformed as in Equation 3.5.

$$\beta_{pqr} \approx \frac{1}{2m\omega}\left(\frac{\partial\alpha_{pq}}{\partial Q}\right)\left(\frac{\partial\mu_r}{\partial Q}\right)\left[\frac{\omega - \omega_{IR}}{(\omega - \omega_{IR})^2 + \gamma^2} + \frac{i\gamma}{(\omega - \omega_{IR})^2 + \gamma^2}\right] \qquad \text{(Equation 3.5.)}$$

The derivatives $\frac{\partial\mu_r}{\partial Q}$ and $\frac{\partial\alpha_{pq}}{\partial Q}$ represent infrared transition dipole moments and Raman transition polarizability derivatives, respectively, for an OH normal mode (Q).

The spectrum has a homogenous line-width of $\gamma$. The derivatives are related to the elements of the uncoupled OH mode tensors through Equation 3.6.

$$\frac{\partial A}{\partial Q} = C_1 \frac{\partial A}{\partial r_1} + C_2 \frac{\partial A}{\partial r_2} \quad A = \alpha_{pq}, \mu_r \qquad \text{(Equation 3.6.)}$$

The derivatives $\frac{\partial A}{\partial r_i}$ are respective to individual OH bonds. The static elements of the derivatives in Equation 3.6. are provided in the original Morita-Hynes treatment in the molecular frame.[66] Additionally, the original Morita-Hynes work treats $\frac{\partial \mu_r}{\partial r_i}$ to include the perturbation effects of hydrogen bonding to the vibrational OH modes. The actual sum frequency response is obtained from the macroscopic susceptibility, $\chi^{(2)}$, without including the constribution from the non-resonant susceptibility, as shown in Equation 3.7.

$$I_{SFG} = \left|\chi^{(2)}\right|^2 \approx \left|N\langle\beta_{pqr}\rangle\right|^2 \qquad \text{(Equation 3.7.)}$$

where $I_{SFG}$ is the sum frequency intensity, $N$ is the number of molecules, and the angles surrounding the hyperpolarizability imply an orientational averaging.

## 3.2. Computational Method

The molecular dynamics methods used in this chapter are similar to those from previous computational efforts with some modifications described below.[44, 45, 47] Simulations were carried out using the Amber 9 software package. The polarizable ion model parameters are taken from previous works on similar systems.[25, 50, 70–72] The polarizable POL3 model was used for water molecules.[73] Fully polarizable models have been used in previous interface simulation studies because they are known to more accurately reproduce interfacial structure and free energy profiles.[62, 74–77]

A total of 4 systems were simulated consisting of aqueous salt and $CCl_4$ phases. A slab geometry was used to produce two interface regions within each simulation cell.[44] The results of the analyses performed herein on each simulated system made use of the natural symmetry of the two interfaces by averaging the results from the two surfaces. The organic region was formed in a box 30 Å on a side with 169 $CCl_4$ molecules to reproduce a standard temperature density of 1.59 $\frac{g}{mL}$. The aqueous region was formed in a box 30x30x60 Å$^3$, with the long axis perpendicular to the interfaces. The number of water molecules and ions varied for each system in order to reproduce a concentration of 1.2 M. The specific populations of each molecule are listed in Table 3.1. The organic and aqueous boxes were then joined to form a system 90 Å long with interface areas of 30x30 Å$^2$.

| System | $H_2O$ | Cation | Anion |
|---|---|---|---|
| Neat Water | 1800 | 0 | 0 |
| NaCl | 1759 | 40 | 40 |
| $NaNO_3$ | 1732 | 40 | 40 |
| $Na_2SO_4$ | 1740 | 86 | 43 |

TABLE 3.1. Aqueous molecule and ion numbers. Listed are the populations of each component for the 4 simulated aqueous phases. All systems were simulated at near 1.2 M salt concentrations.

The water, salts, and $CCl_4$ were each randomly packed into their respective boxes with a minimum packing distance of 2.4 Å. After joining the aqueous and organic phases and forming the two interfaces, the total system was energy minimized using a conjugate gradient method. Following minimization, the system was equilibrated at a constant temperature of 298 K with weak coupling to a heat bath for a period of 10 ns, using a simulation timestep of 1.0 fs. A non-bonded potential cutoff of 9.0 Å was used. Following equilibration the system was simulated with the same parameters for a further 10 ns with atomic position data recorded every 50 fs. This resulted in a total of 200,000 snapshots which were used in the data analysis.

### 3.3. Component Densities

The component density profiles of each system were calculated to study the effects of added salts on water's density profile, and to find any deviations in the behavior of water from the neat-$CCl_4$-$H_2O$ system. The water density profile of each system was fitted to a hyperbolic tangent function (Equation 3.1.). The resulting profiles are plotted in Figure 3.2. The profiles were centered about the GDS locations, $z_0$, at 0.0 Å, and all lineshapes are plotted as distances to the GDS. Each interfacial width, $d$, is designated as a highlighted blue region of width $d$ centered about $z_0$. The widths of the interfacial regions for the neat-$CCl_4$-$H_2O$ (A), NaCl (B), $NaNO_3$ (C), and $Na_2SO_4$ (D) systems are 2.16, 2.62, 2.20, 3.69 Å, respectively. In each of the salt solutions, the anion density profile shows higher density near the interface, appearing as a peak in the density profile. These anion enhancements all occur closer to the interface than the corresponding counter-cation density enhancement. Various parameters of interest such as the interfacial thicknesses, ionic enhancement locations (taken to be the location of the maxima in the ion profiles), and relative distances between the peaks of the ion profiles are collected in Table 3.2. Unlike experimental surface studies, the simulation results provide a full microscopic view of ion location and stratification within the interfacial region.

The oscillations in the surface density profiles of water and the adjoining organic $CCl_4$liquid phase have been noted previously and attributed to thermal capillary waves on a larger length-scale than the simulated system size.[78] The same work also made note that the interfacial thickness is size-dependent on the interfacial surface

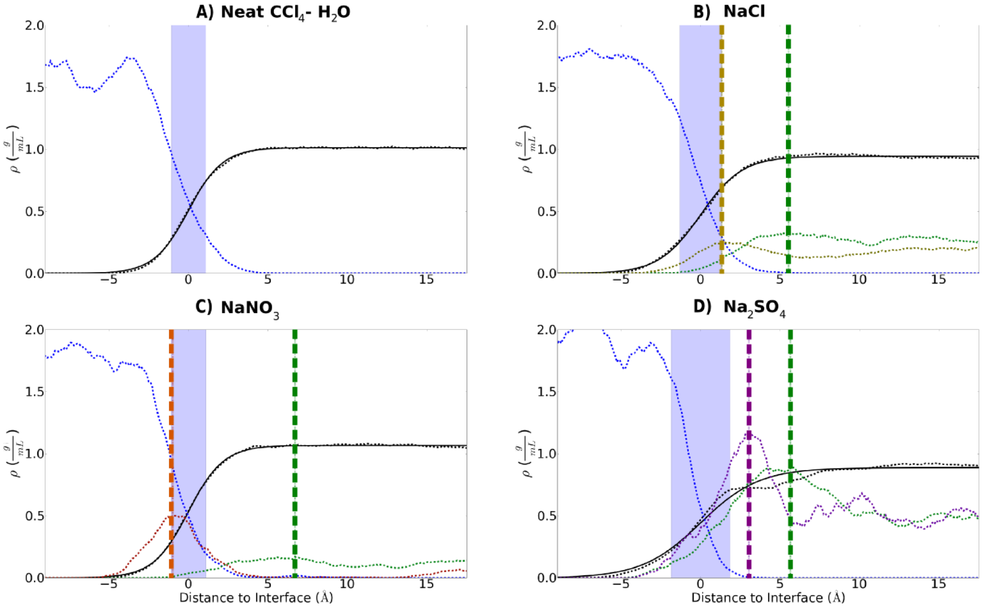

FIGURE 3.2. Aqueous salt solution (1.2 M) and $CCl_4$ surface density profiles. (A) Neat-$CCl_4$-$H_2O$, (B) NaCl, (C) $NaNO_3$, and (D) $Na_2SO_4$ aqueous solution densities and the (solid black) fitted lineshape. (dashed blue) The $CCl_4$, (dashed green, 10x) $Na^+$ cation, and (scaled 5x) respective anion densities.

area. Increasing the surface area dimensions should therefor cause a proportional increase in the interfacial width. As a consequence, care must be taken when making quantitative comparisons between widths and locations found in differing simulation studies. However, relative width ordering between similarly-sized systems should remain, as shown in two separate works on the $CCl_4$-$H_2O$ surface.[45, 78]

| System | $d$ | Anion ( Å) | Cation ( Å) | Anion-Cation Distance ( Å) |
|---|---|---|---|---|
| Neat-$H_2O$ | 2.16 | - | - | - |
| NaCl | 2.62 | 1.33 | 5.53 | 4.20 |
| $NaNO_3$ | 2.20 | -0.99 | 6.71 | 7.70 |
| $Na_2SO_4$ | 3.69 | 3.04 | 5.64 | 2.60 |

TABLE 3.2. Aqueous salt system density parameters.

In comparing the three salt solutions studied here, any differences in these systems are the result of the anion because the same cation was used in each system. NaCl is the simplest of the three salts with a monatomic and monovalent anion. The peak of the anion density profile is within the aqueous phase (i.e. it is found on the aqueous-side of the interfacial width). The location of the cation density peak is, as mentioned above, deeper into the aqueous phase than the anion by over 4 Å. This layering of ions within the aqueous phase is attributed to the break in the isotropy of the field of the bulk region upon introduction of the organic phase. From the studies it is clear that polarizable monovalent anions move towards the interface and effectively screen the induced field from the organic phase. The counter-ions then are drawn towards the negative charge built up by the anions to create the second ion density peak deeper in the aqueous phase. The overall shape of the water profile in the NaCl system is relatively unaffected (compared to the reference $CCl_4$-$H_2O$ system Figure 3.2.a) by the presence of the ions. The width of the interface is slightly increased above that of the reference system. The behavior at a $CCl_4$-$H_2O$ surface is markedly similar to that of NaCl at the air-$H_2O$ interface, as determined by a previous MD study.[43]

It is important to note from density calculations that ions that increase the interfacial width at the $CCl_4$-$H_2O$ interface correspond to ions that result in an enhancement of the SFG signal from interfacial water. As discussed later, the SFG calculations show excellent agreement with experimental results that also show this enhancement for such ions. Also, it is found that those ions that are best known to enhance the strength of hydrogen-bonding (i.e. ${SO_4}^{2-}$) produce wider interfaces with greater water penetration into the $CCl_4$ phase.

The $NaNO_3$ system introduces the monovalent, polyatomic nitrate anion. In the simulation a strong surface density enhancement of the nitrate anion is found as shown in Figure 3.2.(c). The nitrate density peak is located the furthest out from the aqueous phase of the three salt systems. The location of the sodium cation peak in this system is a significant distance further into the bulk water relative to the anion than in either of the NaCl or $Na_2SO_4$ systems. The increase in ion-pair distance is likely the result of strong screening of the interfacial field by the surface-active anion, and the solvating waters around it. The interfacial width of the $NaNO_3$ system is the narrowest relative to the other salts in this study. It is likely that slight reorientation of the surface waters near $CCl_4$ enhance the solvation of the ${NO_3}^-$ in the plane of the interface and establish a much more hydrated region for the anion to adsorb. Water reorientation is more fully described later in this chapter. The subsurface waters then continue to screen the charge of the surface-active ${NO_3}^-$, and decrease the coulombic force pulling the cation closer to the surface.

The widest interface is that of the $Na_2SO_4$ solution, indicating that the ${SO_4}^{2-}$ anions act to increase the number of interfacial water molecules on both sides of the GDS, consistent with the highly solvated nature of ${SO_4}^{2-}$ and its larger size. ${SO_4}^{2-}$ density enhancement (the peak of the anion density profile) is furthest into the aqueous bulk of the three anions simulated. The calculations suggest that the divalent and highly polarizable nature of the ${SO_4}^{2-}$ anion attracts its counter-ion closest, leading to the narrowest sub-surface ionic double-layer. This attraction is likely coulombic. Although the greatest anionic concentration enhancement is further into the bulk water region, seemingly outside the region designated by the interfacial width, the water interfacial width is still greatly enhanced. This is in agreement with the experimental $Na_2SO_4$ SFG studies where sulfate ion leads to an enhanced SFG signal throughout the bonded OH stretch region, consistent with a larger interfacial width.[1]

The results of these and related simulations of ions at liquid-liquid interfaces, and the recent experimental results of similar systems, demonstrate that some ions behave at the $CCl_4$-$H_2O$ interface very differently than what has been calculated and observed at air-water interfaces.[79–81] The most striking example is that of the polyatomic nitrate ion which has been investigated at the air-$H_2O$ interface by computer simulation,[25, 82] SHG and SFG spectroscopies,[83–85] and depth resolved X-ray photoemission spectroscopy.[86] In contrast to what is observed here and in the related experimental SFG studies of the $CCl_4$-$H_2O$ interface where nitrate ion shows an enhanced presence in the interfacial region, at the air-$H_2O$ interface the nitrate ion shows no greater affinity for the surface than the bulk water. The large planar geometry of the ${NO_3}^-$ anion and its low charge appear to repel it from the air-$H_2O$ surface where it encounters a reduced solvent cage and seeks a more hydrated solvation state. For ${SO_4}^{2-}$ ion, experiments at both the air-$H_2O$,[87] and $CCl_4$-$H_2O$ interface indicate sulfate does alter the interfacial region, consistent with what is observed in these computations. Unlike the monovalent ions, the divalent sulfate anion has a very large first solvation shell. These calculations indicate that at the $CCl_4$-$H_2O$ interface it prefers a location deeper into the aqueous phase region and affects the interface from a greater distance than the other ions. The comparison of these computations with SFG experimental results will be discussed in more detail later in the chapter.

The experimental SFG study concluded that the accumulation of the ions into the interfacial region resulted in a narrower interfacial width.[1] Results here based on density profile analysis are not in agreement with the experimental conclusions.

The simulations results show that the presence of ions increases the interfacial width above that of the neat $CCl_4$-$H_2O$ system. However, the relative ordering of interfacial widths respective of the anions in solution is preserved. Both studies are in agreement with $NO_3^-$ giving rise to the smallest, and $SO_4^{2-}$ the largest interfacial width, but that of the neat $CCl_4$-$H_2O$ system is different. The fitting function used here does not necessarily correspond to the interfacial cross-section detected in SFG experiments, but instead represents the molecular sharpness of the liquid-liquid transition region. SFG signals are proportional to both the number density and the orientation of molecules in an interface. Thus, the experimentally determined thicknesses will not correspond quantitatively to simulated density profile fitting parameters, but remain an informative metric for comparison.

### 3.4. Water Orientation

Previous studies have provided a detailed overview of water orientation at the interface with both air and organic phases.[1, 43, 45, 53, 63] The topmost water layers are highly disrupted because of their contact with the organic phase, and it has been suggested that ordering of both the organic and water molecules would lead to a field across the boundary of the interface.[1, 45] This can influence charged species, and the ordering and orientation of the H-bond network. Recent experimental SFG results suggest that the accumulation of charged ions leads to a field-screening that affects the orientation of waters in the topmost layers. This is complemented by the results of the current study.

The orientation of water within the aqueous/organic interface of the system was defined using the angles formed by molecular axes and the fixed reference axis of the system (perpendicular to the interfacial plane), as described previously, and as

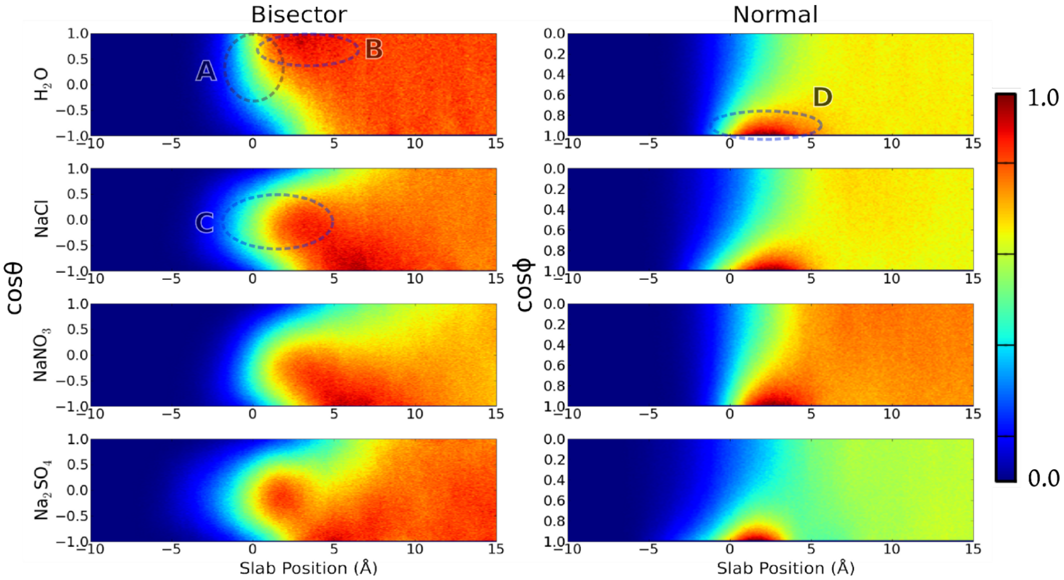

FIGURE 3.3. Orientation profiles of interfacial water molecules at different depths from the GDS. (left) Molecular bisector and (right) molecular planar normal profiles. Neat-$CCl_4$-$H_2O$, NaCl, $NaNO_3$, and $Na_2SO_4$ system water orientation profiles top to bottom row, respectively.

depicted in Figure 3.1. Figure 3.3. shows the angle profiles of both the molecular bisector and the molecular plane normal of water molecules relative to the system reference axis at various depths into the aqueous phase. Darker red regions of the plots indicate higher orientational populations, while homogeneous coloring across the angle range indicates orientational isotropy.

In the left column of Figure 3.3. are the bisector orientation profiles for each of the systems. Coloration of the plots correspond to the normalized populations at each point in the distributions. Highest populations are colored dark red (1.0), and lower populations (0.0) are colored in dark blue. The far-left dark-blue regions of the plots show the $CCl_4$ bulk near the interface where few or no waters are found. The GDS is located at a depth of 0.0 Å. To the far right in the water bulk, the flat, uniformly-colored profile represents the expected isotropic orientation of the bulk waters. The regions of interest lie around the GDS within the interface. The top bisector profile is that of the neat-$CCl_4$-$H_2O$ system, and it shows a transition in the profile beginning approx. 2 Å into the $CCl_4$ phase, and extending up to 5 Å into the aqueous side, at which point the profile becomes orientationally isotropic. At the GDS most of the waters are oriented between $0.0 < \cos\theta < 1.0$, indicating a range of orientations as depicted in Figure 3.4.a In this range one of the OH-bonds points into the aqueous side, and the other straddles the interfacial plane with a slight affinity towards the organic $CCl_4$ phase. Just under the water surface, between 2-4 Å into the neat-$H_2O$ phase, a dark-red region spanning approx. $0.7 < \cos\theta < 1.0$ appears. This narrow orientational range is depicted in Figure 3.4.b, and is similar to the waters in the topmost aqueous layer nearer to the GDS, but further limited such that one OH bond points into the $H_2O$ side, and one straddles the interfacial plane with a tendency to point into the $H_2O$ phase.

The reference $CCl_4$-$H_2O$ bisector orientational profile is comparable to previous simulations of the same system. Using slightly different simulation parameters for the same reference $CCl_4$-$H_2O$ system, Wick and Dang found the free-OH to point slightly into the $CCl_4$ phase at the GDS with an angle of $\cos\theta\ _{free-OH} \approx 0.4$.[53] This corresponds to $\cos\theta\ _{bisector} \approx 0.5$ in the this chapters's angle definition. Similarly, deeper into the surface the angle profile diminishes such that $\cos(\theta_{free-OH}) \approx 0.0$ within 5 Å of the GDS, corresponding to $\cos(\theta_{bisector}) \approx 0.8$ in the current scheme. Those results agree with this chapters's reference $CCl_4$-$H_2O$ profile, further complementing the experimental conclusions performed on the same systems.[1, 88]

Bisector angle profiles for the salt systems show different behavior than that of the reference neat $CCl_4$-$H_2O$ system. The profiles of the salt systems at the GDS all center about the $\cos\theta = 0$ region, with a range of approx. $-0.5 < \cos\theta < 0.5$. This

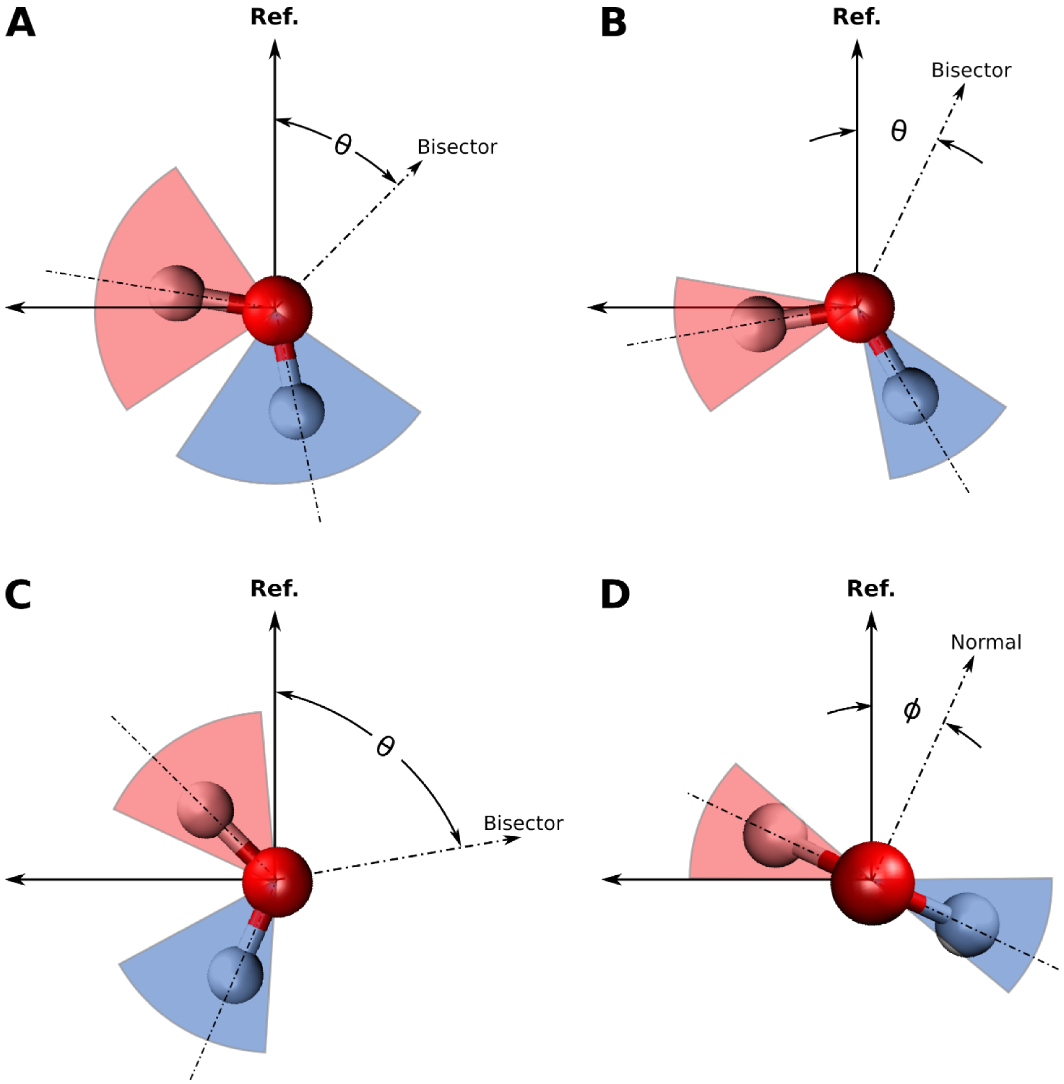

FIGURE 3.4. Depictions of water orientation ranges spanning values of $\theta$ and $\phi$. Ranges of $\theta$ are (A) $0 < \cos\theta < 1$, (B) $0.7 < \cos\theta < 1$, (C) $-0.5 < \cos\theta < 0.5$. (D) The $\phi$ range of $0.7 < \cos\phi < 1$.

indicates a straddling water molecule with the orientational range depicted in Figure 3.4.c. The water in that range is clearly oriented such that one OH-bond always points out of the aqueous phase into the $CCl_4$, and the other always points in to the water bulk. The OH-bond that would straddle the interface in the reference system points out of the interface with a greater angle. This orientation, centered about

$\cos\theta \approx 0$, extends into the water phase up to 3 Å, at which point the profile shifts to the darker region near -1.0 < $\cos\theta$ < 0.7. The sub-surface region of the profile between 4-7 Å in each system corresponds to a flip of the water orientation, as referred to in a recent SFG study as a "flip-flop" model where water orients to counteract the field of charged species at interfaces.[89] The cation density enhancement in each salt system is within the region approx. 5-7 Å below the GDS. The waters may be orienting with the negatively charged oxygen end towards those cations, and with the field established by the ion double-layer within the interface. In each of the salt bisector profiles there is a clear depletion of waters oriented towards $\cos\theta = 1$ suggesting that alignment of the bisector with the reference axis is not preferred. The effect is most pronounced in the $Na_2SO_4$ system where the distance between counter-ion density enhancements is smallest, and the transition in the bisector profile is the most abrupt, changing from a profile mostly in the range of -1.0 < $\cos\theta$ < 0.5 to isotropic orientation quickly near 8 Å into the aqueous phase. The $NaNO_3$ system bisector profile shows the effect furthest into the water bulk, extending almost to 13 Å. Counter-ion density enhancement is most separated in $NaNO_3$, however, and most of the orientational affinity for -1.0 < $\cos\theta$ < 0.5 occurs within the first 10 Å of the surface. The bisector profile of the NaCl system is broadest with -1.0 < $\cos\theta$ < 0.7 starting near the GDS. Also, orientational isotropy is shallowest in the NaCl system starting near 7 Å into the aqueous phase.

It appears that the field established by the anion-cation pairing within the interface affects the depth to which waters are oriented before the bulk isotropic profile begins. Also, the range of orientations beneath the surface is dependent on the properties of the anion. The weakly polarizable $Cl^-$ anion does not restrict the orientational range as much as the more polarizable ${NO_3}^-$ and ${SO_4}^{2-}$. Anions also appear to control the depth to which the water orientation is felt, with the most surface-active $NO_3^-$ anion causing the deepest effect. $SO_4^{2-}$ anion shows the strongest restriction on the range of bisector angles, and the sharpest orientational transition to the bulk, which may be attributed to the higher charge of the anion, and thus the stronger field established between the counter-ions in the system.

Orientational profiles for the molecular plane normal of the water molecules ($\phi$-profiles) are found in the right-column of Figure 3.3. The range of a $\phi$-profile is limited to $0.0 < \cos\phi < 1.0$ because of the inherent symmetry of the plane of the water molecule. More similarity is shared between the $\phi$-profiles than the bisector profiles for the different systems. The neat $CCl_4$-$H_2O$ $\phi$-profile is typical of the other systems in appearance, with a large clustering of water population in the range of $0.7 < \cos\phi < 1.0$ between the GDS and up to 7 Å into the aqueous phase. This particular $\phi$ range is depicted in Figure 3.4.d, showing the mostly flat (i.e. parallel to the interface) orientation of the molecular plane. It is notable that the $\phi$-orientation is affected to the same depth as the first peak (dark-red region) of the bisector profile. However, in the salt systems the second peak near to $\cos\theta = -1.0$ begins at a depth where the $\phi$-profile has already become isotropic. Thus, in the salt systems, the first water layer (between the GDS and almost 4 Å into the surface) has a defined $\phi$-orientation that is rather flat on the interfacial plane, but the deeper waters (4-7 Å into the interface) are isotropic in $\phi$, and oriented with $\cos\theta$ closer to -1.0 (an orientation with oxygen pointing into the water bulk, and hydrogens more towards the interface).

By virtue of the interdependence of $\theta$ and $\phi$ (the bisector is perpendicular to the molecular plane normal at all times) a value of $\cos\phi = 1.0$ implies $\cos\theta = 0$, and vice-versa. However, a broad $\theta$-range allows for a full range of $\phi$ values. Although the second peak of the salt-system bisector profiles is concentrated near to $\cos\theta = -1.0$, the corresponding $\phi$-profile is isotropic. This deeper region (the second water layer) orients with the bisector counteracting the field of the anion-cation double-layer, and the only apparent affinity is that of placing oxygen closer to the cation density enhancement (and hydrogen closer to the anion layer), while the $\phi$-profile spans the entire orientational range.

### 3.5. Calculated Sum-Frequency Spectra

The effect of the varied set of anions on the $CCl_4$-$H_2O$ interface is linked from simulation to empirical data through the computed SFG spectra. The computed spectra for the SSP polarization (polarization schemes are fully described in literature[90]) are presented in Figure 3.5. along with the experimental spectra (inserts) from the previous experimental SFG work with these same salt solutions interfaced with $CCl_4$.[1] Each of the spectra show a salt system response (colored traces) overlayed on the reference $CCl_4$-$H_2O$ spectrum (black or dashed-black traces). On first look, the overall computed intensities and lineshapes follow remarkably similar trends as in the experimental systems. All the spectra have a strong feature near 3660 $cm^{-1}$coinciding with the "free-OH" vibrations as defined previously,[1] and corresponding to one of the uncoupled OH stretch modes from water molecules that "straddle" the interface (Figure 3.1. a, b, and c).[1] The broad spectral region from 3200-3500 $cm^{-1}$is attributed to the more highly-coordinated OH-oscillators that are solvated at the surface, or just beneath the surface with stronger hydrogen-bonding. Each of the spectra computed for the salt-solutions differ markedly from each other and from the neat $CCl_4$-$H_2O$ spectrum. The monovalent ions ($Cl^-$ and $NO_3{}^-$) in solution produce a measurable decrease in intensity of the lower-frequencies of the spectra with very little change to the free-OH mode. Like the experimental counterparts, the decrease is greatest around the 3200-3400 $cm^{-1}$region but shows little change from the neat $CCl_4$-$H_2O$ system above 3500 $cm^{-1}$. As in the SFG experiment, the presence of the ${SO_4}^{2-}$ anion causes an opposite effect by significantly enhancing the intensity below 3600 $cm^{-1}$.

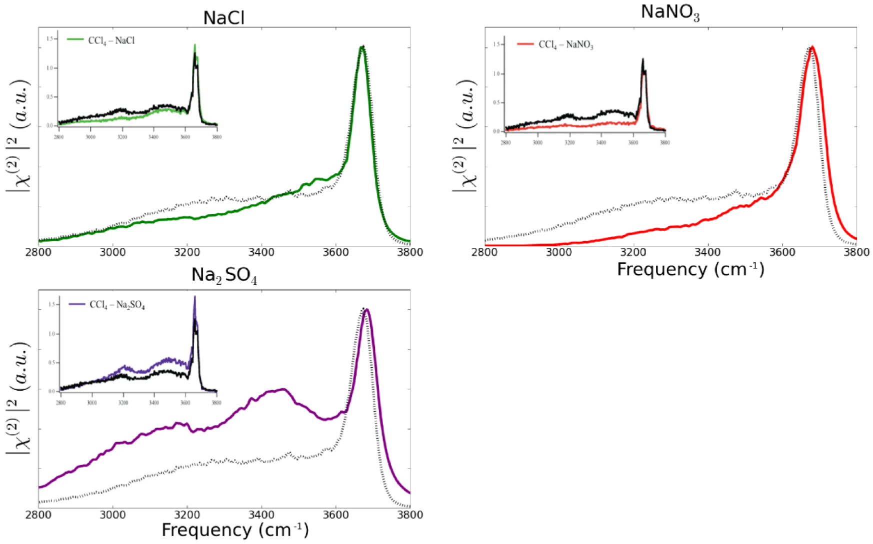

FIGURE 3.5. Vibrational SFG spectra of the water-OH stretching region for each interfacial aqueous-salt-$CCl_4$ system. (black-dashed) The reference $CCl_4$-$H_2O$ interface spectrum. Insets are reproductions of the experimental spectra $(\chi^{(2)}_{eff})$ from McFearin et al.[1]

The reference $CCl_4$-$H_2O$ spectrum reproduces well the lineshape from experiment, but lacks the definition of the two peaks found near 3250 and 3450 $cm^{-1}$. These lower-frequency features have been attributed to the different H-bonding species of water that make up the more highly-coordinated, tetrahedral environments found deeper into the interfacial region. The reference $CCl_4$-$H_2O$ lineshape is quite similar to that of the experiment. The salt-solution spectra show an overall drop in signal when $Cl^-$ and ${NO_3}^-$ are added and an increase in intensity due to ${SO_4}^{2-}$. This suggests that the methods are sound and justified for experimental comparison in this study.

The conclusions drawn from the experiments are that the presence of anions at the interface causes a “field-screening” that decreases the innate interfacial field at the $H_2O$-organic interface, and consequently the number of bonded water molecules contributing to the SFG spectrum. Both of the monovalent anions, $Cl^-$ and ${NO_3}^-$, show this effect in their SFG spectra. For both the experiment and these calculations, comparison to the reference $CCl_4$-$H_2O$ spectrum shows that the added presence of the surface-active anions decreases the lower-frequency intensities. Calculations show that $Cl^-$ affects a notably smaller decrease in the spectral intensities than the ${NO_3}^-$ system, similar to experiment. This result is most likely due to the higher preference for the surface of the larger, and more polarizable nitrate in the presence of $CCl_4$. The ${NO_3}^-$ ion is extremely surface active, as seen in the density profile, and should thus cause the greatest “field-screening” to waters found deeper in the bulk.

The larger divalent ${SO_4}^{2-}$ anion accumulates deeper into the aqueous bulk and exhibits the lowest surface affinity of the ions studied. This is most likely due to the higher charge of the anion that leads to greater solvation. The sulfate provides little or no screening of the interfacial field from the top-most water layer, and more greatly affects the deeper, highly-coordinated waters. The bonding region spanning the lower-frequency features is notably enhanced above the reference spectrum in both experiment and computation. This indicates stronger ordering of deeper interfacial waters, consistent with the anion location.

As concluded in the experimental SFG work, the monovalent anions appear to screen the deeper water molecules from the field produced by the phase change at the aqueous-organic interface. This is supported by the MD simulations showing that monovalent ions show a strong surface affinity and interact with surface waters. The large but more highly charged divalent ${SO_4}^{2-}$ anion experiences stronger solvation and is thus found deeper in the aqueous phase. Deeper anions do not participate as interfacial field screening agents to the same extent as their monovalent counterparts, but act to strongly orient water near the interface, perhaps through the strong field established by the ion double-layering. The distance between the counter-ion density peaks (Table 3.2.) follows the inverse of the trend of SFG signal enhancement. As the ionic double-layer size increases, the SFG signal decreases. Similarly, the smallest double-layer size, that of the ${SO_4}^{2-}$ system, produces the greatest signal enhancement across the lower frequencies of the water OH-stretching SFG spectrum. Although the water density profiles do not change markedly between the different systems, the orientational profiles do show large variation from the neat $CCl_4$-$H_2O$ system, and some slight variation between the salt-solutions. The two factors that alter the SFG intensity are changes in the number of contributing water bonded species, and a change in orientation of various water bonded species. From the water orientation profiles (Figure 3.3.) it is clear that the presence of anions at the $CCl_4$-$H_2O$ interface causes a strong orientation change from the reference $CCl_4$-$H_2O$ system. There appears to be a strong coupling between the presence and size of an ionic double-layer, the subsequent reorientation of surface water molecules, and the resulting SFG signal change.

## 3.6. Summary

The unique environment created by interactions between water and hydrophobic molecules makes ionic adsorption and transport across interfaces possible. Aqueous-hydrophobic surfaces are of prime importance in applications ranging from ion transport, chemical remediation, and catalysis, to chemical synthesis. Complex interfaces between aqueous media and organic phases enhance chemical reactions, and thus motivate research to understand such environments. The study reported in this chapter provides an important step in understanding aqueous-organic surfaces by computationally examining simple aqueous salt solutions interfaced with hydrophobic liquid $CCl_4$. Through a combination of simulations and computational analysis, the nature of ionic adsorption and its effect on water hydrogen-bonding, geometry, and orientation at the liquid-liquid boundary is determined.

Analysis of the component density profiles provides a thorough microscopic picture of ionic surface affinity, double-layering, and effect on interfacial size. The smaller and less polarizable $Cl^-$ anion behaves at the $CCl_4$-$H_2O$ surface much like at the air-$H_2O$ interface, but the larger surface-active anions do not. Density profile analysis shows that the $NO_3{}^-$ anion exhibits a much greater surface affinity near the organic phase than at an air interface, consistent with experimental conclusions. The orientational analysis of the solutions shows the very different effect of the various salts on the water orientation at the $CCl_4$-$H_2O$ boundary. The orientation profiles show a stratification of water geometries consistent with the emerging picture of a multi-layered surface region with varied geometries and interactions. This reorientation subsequently affects the ionic double-layer and subsurface waters. Such effects are manifested in spectroscopic changes to water's vibrational OH modes as seen in both the experimental and computational results. Consequently, SFG spectra computed in this study build the necessary bridge to the previous SFG work by offering direct comparison of the computational and experimental results. The surface spectroscopic signals, measured and calculated, are altered relative to the ion-free signal, indicating a change to the water bonding at the interface due primarily to the presence of the anion. The divalent $SO_4^{2-}$ anion acts to enhance the number and orientation of interfacial waters, while the monovalent ions have the opposite effect. Both the organic phase and the salt anion species in solution contribute to altering the geometry of water's surface.

Progress has been made toward the goal of further understanding the behavior and impact of ions and a hydrophobic phase on water at liquid-liquid interfaces. The complementary results of both simulation and experiment have strengthened the certainty of some of the underlying surface science of these systems, but challenges still remain. A more complete picture would include knowledge of different cation effects, as well as the changes to the surface by different hydrophobic phases. The ability to analyze these important interfacial environments both theoretically and experimentally provides the tools to better develop an understanding of them.

The next two chapters of this dissertation focus on the behaviors of adsorbing gas molecules as they approach and bind to a water surface. Sulfur dioxide was used as a model gas for the studies, and the computational analysis parallels $SO_2$ binding experiments that took place in the Richmond laboratory. In chapter IV $SO_2$ is modelled using fully atomistic classical MD simulations at equilibrium on a water surface, and during an adsorption event as the gas transits into the water phase. Chapter V chronicles a DFT-MD simulation study of $SO_2$ on a water surface and the various hydration structures and interactions it forms with neighboring water molecules.

# CHAPTER IV

# SULFUR DIOXIDE ADSORPTION TO AQUEOUS SURFACES

This work was published in volume 115 of the Journal of Physical Chemistry C in November 2011. Dr. Kevin E. Johnson proposed the use of steered molecular dynamics for simulating a transiting $SO_2$ molecule, and provided great support in developing the simulations and computational analytical techniques used throughout the work. Eric Shamay was the principle investigator for this work.

## 4.1. Introduction

The doorway to the uptake of a gas by an aqueous solution is the water surface. Although we know much about the behavior of a gas on either side of that entrance, far less is known about how that surface acts to attract, facilitate, or thwart the transit of a molecule between the two bulk phases. What is the interplay between the gas and surface water molecules, and when does one begin to influence the behavior of the other? What species form during gas adsorption onto liquid surfaces, and what are the intermediary steps? Is molecular orientation of either the gas or surface molecules a factor in the adsorption process? Are specific gas or liquid molecular orientations necessary for gaseous adsorption? Experimental studies to address such questions are valuable but do not provide the full resolution necessary to determine the geometries of adsorbing gases, or to determine the orientations of the molecules at the liquid surface near the adsorption site. This type of information can be determined computationally, and when coupled to the experimental studies can provide a more comprehensive picture of the gas-liquid surface adsorption process.

An important gas for developing a picture of gaseous adsorption and entry into a water surface is sulfur dioxide.[91–101] $SO_2$ enters the environment as an important industrial product, and also naturally through terrestrial processes. Atmospheric dust particles and gases have been implicated in the oxidation of $SO_2$, and act as reaction surfaces for chemical mechanisms that are still poorly understood.[102–106] $SO_2$ acts as a major component of atmospheric pollution, and is a precursor to acid rain formation, and cloud nucleation. Its high solubility in water makes $SO_2$ an integral compound in many aqueous atmospheric reactions, as well. Obtaining a more complete picture of the $SO_2$ adsorption process is important for understanding gaseous adsorption of this environmentally important gas on water and aerosol surfaces as well as being a model system for understanding the more general nature of gases at aqueous interfaces.

This chapter provides a molecular picture of $SO_2$ adsorption on a water surface; it also demonstrates the strong orientational effect of surface water molecules on the adsorbing gas during the approach and entry into the surface region at both high and low $SO_2$ surface concentrations. These computational studies complement and significantly expand the picture developed in recent experimental vibrational sum frequency spectroscopy (VSFS) studies of $SO_2$ adsorption of aqueous solutions of various compositions and temperatures,[16, 17] and the subsequent studies using both classical and ab initio simulations. The experimental studies showed that an $SO_2$ surface hydrate complex forms when an aqueous surface is exposed to $SO_2$ gas. The computational study by Baer et al.[107] then made a series of predictions of the specific nature of the hydrated complex through classical and ab initio simulations. That work developed a detailed picture of the nature of the $SO_2$ surface complex with water, and related it to the surface water OH vibrational IR spectra. The most recent experimental studies have shown that whereas the binding of gaseous $SO_2$ to a water surface is greatly enhanced at cold temperatures, the reversibility of the adsorption process remains.[18] Complementary experiments showed that low pH aqueous environments inhibit the bulk reactions of $SO_2$, but do not affect the surface binding or its reversibility. What is apparent in the VSF spectra obtained in all of these experiments is the tendency of water to reorient upon surface bonding, with the effect becoming more pronounced at high $SO_2$ surface concentrations. Since the $SO_2$ molecule was not specifically probed, conclusions on how $SO_2$ bonding contributes to reorienting surface water molecules and the orientation of $SO_2$ itself upon approach and surface bonding could only be inferred.

To fill this void, the computational studies described herein provide a detailed picture of the orientation of both $SO_2$ and surface water molecules during the adsorption process. The depth profiling studies which examine the orientation of both species during the approach and entry of the gas into the interfacial region are obtained using equilibrium and steered (SMD) classical molecular dynamics simulations. The latter approach involves steering a gas molecule into the aqueous phase, and characterizing its molecular orientation as it transits through the interfacial region. This unique approach enables new insights into the behaviors of gas molecules as they move near to liquid water. We also simulate how $SO_2$ adsorption occurs on a water surface saturated with adsorbed $SO_2$, analogous to the conditions of the $SO_2$ experimental studies recently performed.[18] The results of the study documented here provide an intimate perspective on the adsorption of $SO_2$ at an aqueous surface, and a more complete picture of gaseous adsorption to liquid interfaces.

## 4.2. Computational Approach

Molecular dynamics simulations were performed using the Amber 11 software suite.[11] Polarizable models for the $H_2O$ and $SO_2$ molecules were used in the simulations, and have been used previously in studies on interfacial systems because they are known to more accurately reproduce interfacial structure and free energy profiles.[62, 74, 77] The $H_2O$ model used is the POL3 water model (also discussed in the supplemental information),[73] and for $SO_2$ we used the model of Baer et al. that places a single polarizable center on the sulfur atom.[107] An intermolecular cutoff of 12 Å was used for long-range electrostatic forces. The simulations were performed in the NVT ensemble using Langevin dynamics for temperature control. Induced dipoles were treated by the polarizable potential functions of the Amber molecular dynamics software.

All simulations began with an equilibrated cube of 900 $H_2O$ molecules, with sides of length 30 Å. The long axis of each simulation cell (the axis normal to the water surface) was then lengthened to 120 Å, and the systems were further equilibrated for 10 ns. The simulations all employed periodic boundaries to create an "infinite-slab" geometry. After equilibrating the neat-$H_2O$ slabs two types of systems were created by introducing $SO_2$: a single-$SO_2$ system, herein referred to as the "neat-water" system, and a "saturated" $SO_2$ system with many gaseous surface and bulk-water $SO_2$ molecules.

The low and high concentration simulated systems, "neat-water" and "saturated", respectively, were created as follows: the neat-water simulation involved the addition of a single $SO_2$ molecule either within the bulk of the water slab (for equilibrium MD), or above the slab surface (in the SMD simulations). The single-$SO_2$ neat-water system was then evolved for 2 ns to produce an equilibrated starting configuration. Because of the extremely low concentration of $SO_2$ in the neat-water system the surface waters behave similarly to a true neat-water air-liquid interface. The neat-water system orientational results shown later in this chapter reproduce well the results of previous orientational studies of surface water behavior.[45, 47] The saturated system had 22 $SO_2$ molecules introduced to the water slab bulk in order to saturate it to a level coinciding with the Henry's law constant for $SO_2$ in water ($k°_H = 1.4$ mol/kg*bar).[108] Additionally, 50 $SO_2$ molecules were introduced into the gas phase outside of the saturated water slab to simulate an added $SO_2$ gas pressure. The additional gas in the vapor phase was added over the course of several ns to keep a constant 1 atm of $SO_2$ pressure above the water surface as $SO_2$ gas molecules adsorbed to the surface. The saturated system with both bulk and gaseous $SO_2$ was then evolved for 2 ns to produce a starting configuration for further saturated simulations.

### 4.2.1. Equilibrium $SO_2$ Surface Simulation

Equilibrium simulations involved adding $SO_2$ to a water slab and equilibrating as outlined above. The neat-water system had a single $SO_2$ added to the center of the water box, representing a concentration of 0.06 M. The more concentrated "saturated" system consisted of 22 $SO_2$ molecules in the bulk corresponding to a concentration 1.35 M. This saturated system was exposed to an additional 50 $SO_2$ in the gas phase above the water surface. After equilibration for 2 ns, both the low and high concentration systems were then evolved for a further 10 ns data collection using a time step of 0.5 fs, with atomic coordinates recorded every 100 fs.

### 4.2.2. Steered Molecular Dynamics Simulations

A second set of simulations began with an equilibrated water slab as in the surface equilibrated method above. However, in both the neat-water and saturated starting systems, a single $SO_2$ was introduced 20 Å above the water slab surface, with the sulfur atom tethered to its initial position. The systems were then evolved for 1 ns, taking coordinate snapshots every 20 ps to create 50 starting points for further simulations. Steered molecular dynamics (SMD) were then performed on the 50 system configurations (in both the neat-water and saturated configurations) to guide the $SO_2$ down towards a tethered water near the water slab's center of mass by applying a small steering force to the $SO_2$-sulfur atom. This steering technique has been previously developed and used to successfully model chemical events.[109–114] The $SO_2$ thus passed through the continuum of environments from gas phase to (neat- and saturated) water surface adsorption, and finally absorption into the bulk of the $H_2O$ slab. Each of the SMD simulations were performed for a total of 200 ps, using a time step of 1 fs, and taking snapshots of the system every 25 fs. Figure 4.1. illustrates two sample starting configurations for the SMD simulations, showing both the neat-water slab and the saturated slab configurations before steering the $SO_2$ towards the water bulk.

A separate set of SMD simulations were performed with tethering of one of the $SO_2$-oxygens to the water slab center of mass. This was done to ensure that the orientation of the $SO_2$ during the adsorption transit was not an artifact of the choice of atom used for tethering. The simulations produced the same results (not shown) for the orientational analyses, so the data from the original tethering scheme was used.

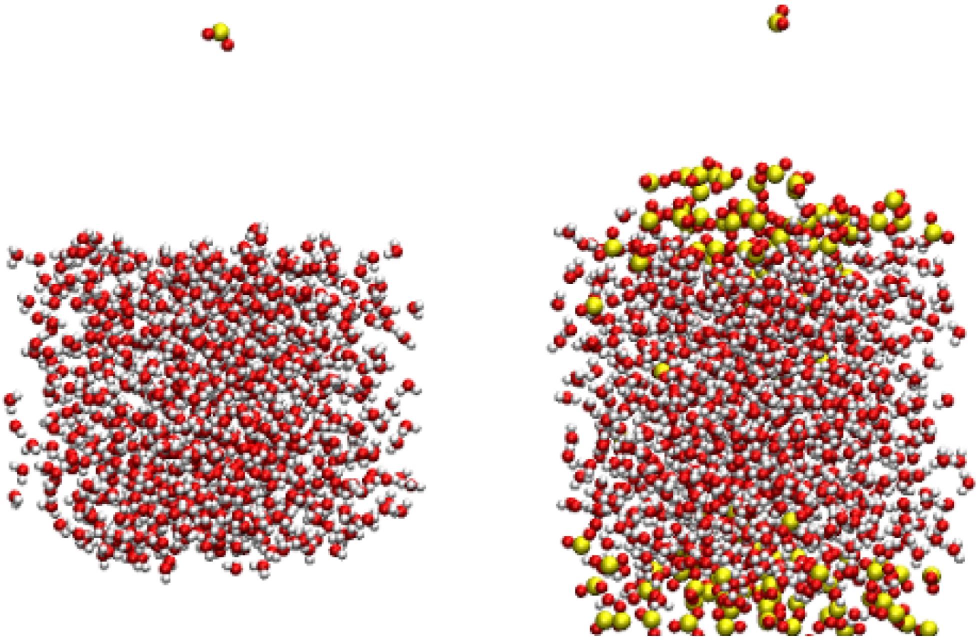

FIGURE 4.1. Sample starting configurations for the (left) neat-water and (right) saturated SMD simulations.

### 4.2.3. Aqueous Surface Location

The first portion of the studies involved creating orientational depth-profiles in the interfacial region comprised of $SO_2$ and $H_2O$ upon exposure and adsorption of the gas. Recognizing that a liquid surface is a dynamic boundary that is neither flat nor stationary, we must define a reference point in the interfacial region which we refer to here as the water surface location. Several previous studies have used the technique of fitting a line shape to the averaged density profile of the water, and extracting interfacial shape and location parameters to define the water surface location.[15, 53, 115] Hyperbolic tangent functions have been used often, and values for the “Gibb’s dividing surface” location, and interfacial width have thus been determined.[55] However, in long simulations the location and shape of the interface changes, and the motion of surface waters alters the interfacial width at any given time step. Thus, the density profile fitting will capture averaged widths and locations, not instantaneous values. Similarly, the averaged values of location and width will obscure information about any drift or deformations the surface undergoes. The analysis presented here attempts to retain these subtleties through the use of a "corrected" coordinate system.

Figure 4.2. demonstrates the problem of surface location drift during a simulation (even with utilizing the Amber NSCM parameter). Figure 4.2.A shows the density profile of water and $SO_2$ over the course of one of the 10 ns trajectories used in this project using the original uncorrected coordinates of the system taken from the raw atomic positions of the molecular dynamics data output. The water density profile and location (thin gray line in Figure 4.2.A) is produced by averaging the instantaneous density profile at each time step in the simulation over all the time steps. The water profile was then fit to a tanh function (black line) to extract the position and width parameters of the water surface. The fitted surface water density profile has a width of 3.77 Å, which is comparable to values reported for similar neat-water systems.[45, 116] A bulge in the gas-phase ($\leq$ 52 Å) side of the water density profile is indicative of the drift of the water slab over the course of the trajectory. Thus the calculated location and width from the tanh line fit are not accurate over long trajectories for defining a stationary reference point.

To overcome this problem we define the water surface location by calculating a reference location at each time step by averaging the positions of the waters contained in the topmost monolayer. This provides a consistent and intuitive reference point in the simulations to which analyses are related, but does not increase the computational burden. The number of waters included in the averaging is determined by taking a few issues into account. First, counting the waters found in the topmost cross-

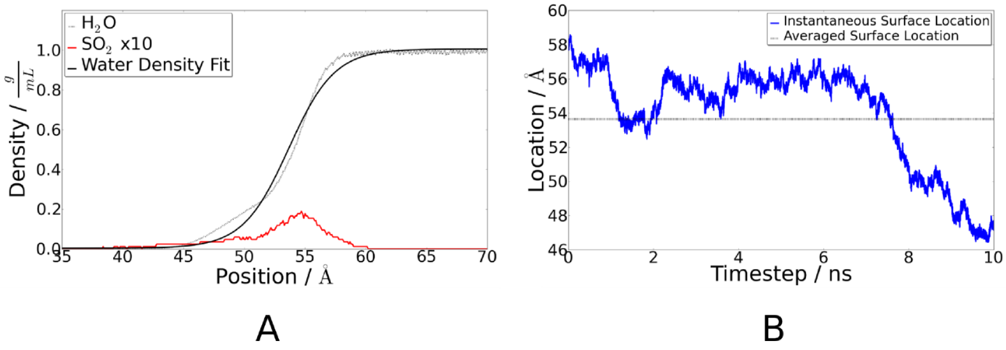

FIGURE 4.2. (A) Density profiles of $H_2O$ (Gray) and $SO_2$ (red) from a 10 ns simulation of the neat-water system with a single $SO_2$. (B) The instantaneous location of the outer $H_2O$ monolayer for each simulation time step (blue), and the surface location extracted from the density fitting (horizontal dashed line).

section of the water slab over several time steps indicated between 65-75 waters that established a full monolayer. This was done by a visual inspection of the slab using the VMD MD visualization package.[117] Alternatively, assuming a spherical model of water with a radius of 2.2 Å, two layers of hexagonally tight-packed spheres yielded a similar number of surface water molecules. Increasing the number of waters used in calculating the surface location diminishes the effects of the few waters that briefly rise above the surface into the gas phase, stabilizing both the surface position and thickness values. Taking the close-packed model as a maximum number of waters fit into a flat surface, the topmost 70 water molecules were used for calculating instantaneous water surface locations for each simulation step.

This method for finding the outer monolayer location was implemented, and the surface location is plotted as a function of simulation time in Figure 4.2.B. It is apparent from the surface location plot that the water slab location, and thus the surface location, drifts over the 10 ns, spanning approximately 12 Å. However, the maximum standard deviation of the positions of the waters comprising the surface layer at each time step is only 1.85 Å. Consequently, all depth locations in the analyses are calculated relative to the instantaneous surface location at the corresponding time step of the trajectories.

### 4.2.4. Molecular Orientation

Knowing the molecular orientation of both the $H_2O$ and $SO_2$ is a prerequisite for understanding the chemistry occurring during the $SO_2$ adsorption process. With the surface location as defined above, the simulated systems were analyzed to characterize the orientation of $H_2O$ and $SO_2$ in various environments above, within, and below the aqueous surface region. The two molecules studied are similarly shaped with a $C_{2v}$ axis along their bisectors, and a molecular plane defined by three atoms. A body-fixed frame is defined for both $H_2O$ and $SO_2$ as shown in Figure 4.3. In each analysis a space-fixed reference axis is used that corresponds to the long axis of the system's periodic cell normal to the plane of the water surface. The orientational analyses presented herein focus on two angles used to define molecular orientation. The molecular orientation angles $\theta$ and $\phi$ are determined from a set reference axis as shown in Figure 4.4.A.

The "tilt" angle, $\theta$, defines the angle formed between the molecular bisector vector (the molecular z-axis, pointing from the central atom in the direction of the other two atoms) and the positive system reference axis. Thus the value of $\theta$ falls within a range of [0°,180°]. An angle of $\theta = 0°$ indicates a molecule with its bisector aligned with the reference axis, while $\theta = 180°$ results from an anti-aligned configuration. Sample representations of molecular orientations resulting from different values of $\theta$ are shown in Figure 4.4.B.

A second angle, $\phi$, defines the molecular "twist" of the molecule. $\phi$ is the angle of rotation around the molecular bisector axis that quantifies the rotation of the

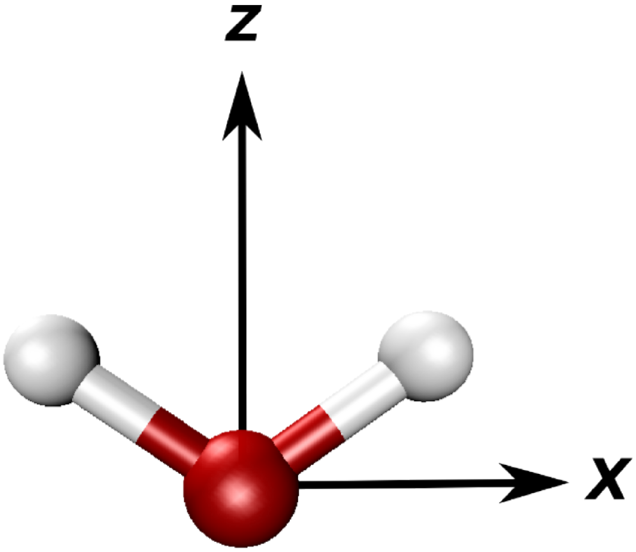

FIGURE 4.3. Definition of molecular body-fixed axes for the two $C_{2v}$ molecules: $SO_2$ and $H_2O$.

molecular plane with respect to a plane perpendicular to the water surface. The values of $\phi$ fall in the interval [0°,90°] because of the symmetry of $H_2O$ and $SO_2$ molecules with respect to twist about their bisector axes. For values of $\theta \approx 90°$, $\phi$ provides additional information about whether the molecular orientation is “flat” to the surface (e.g. the plane of the molecule is aligned with the plane of the surface), or if it is perpendicular. The values of $\phi$ for different molecular orientations are depicted in Figure 4.4.C. Values of $\theta$ close to 0° or 180° result in an isotropic distribution in $\phi$ because of the symmetry of the plane of the surface in directions perpendicular to the surface normal reference axis.

### 4.3. Surface Density Distributions

One measure of surface activity is the spatial distribution of molecules in the interfacial region. The density distributions of both $H_2O$ and $SO_2$ were calculated for

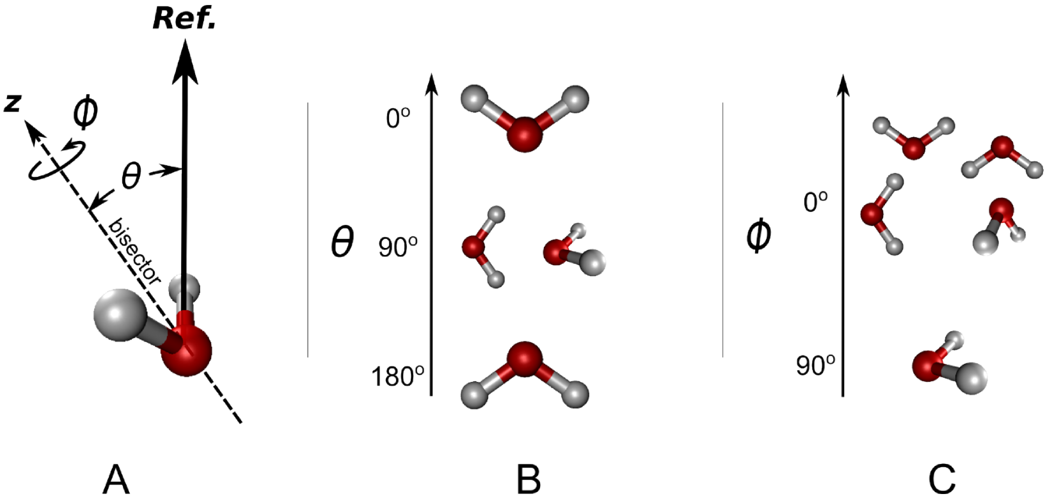

FIGURE 4.4. (A) The definition of the molecular orientation angles $\theta$ and $\phi$. (B) $\theta$, the bisector "tilt" angle, (C) $\phi$, the bisector "twist" angle.

the equilibrium MD simulations. The results presented in Figure 4.5. show both the water (black) and $SO_2$ (red) density distributions, averaged over the two simulated interfaces of each slab. As shown, the single $SO_2$ in the neat-water system remained at the water slab surface. The $SO_2$ in the saturated system accumulated mostly at the surface, but some residual $SO_2$ remained well into the bulk water.

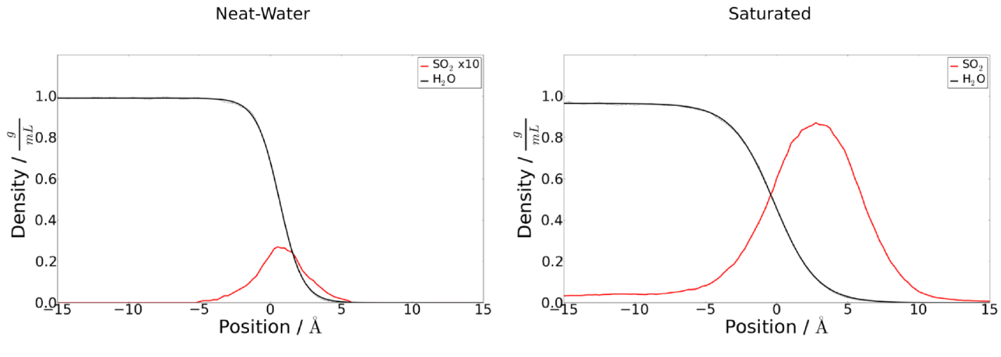

FIGURE 4.5. Density distributions of (black) $H_2O$ and (red) $SO_2$ (neat-water system on left scaled 10x, saturated on right) near a water surface.

In the simulated neat-water slab, the $SO_2$ molecular density distribution concentrates near the water surface location, indicating an affinity for the interfacial region. During the course of the simulation, the $SO_2$ does not venture into the bulk water nor does it escape the water surface into the gas phase, but remains located within 5-Å of the surface region. This is consistent with what was found experimentally in the Richmond laboratory using VSFS,[16, 17] and also supported by the computational simulations and spectral calculations of Baer et al.[107] The experimental studies indicated that upon exposure of $SO_2$ to a $H_2O$ surface, a layer of solvated $SO_2$ forms, modifying the structure of water in the upper surface region. In the experimental system, the $SO_2$ bonding interaction with the free OH oscillators is manifested in a red-shift of the free OH frequency indicative of a bonding interaction.

The saturated solution simulation results indicate that under the high concentration of $SO_2$, the $SO_2$ accumulation at the surface is increased. However, unlike the neat-water slab, the saturated slab has a non-zero bulk concentration of $SO_2$. The added concentration of $SO_2$ creates a layer of molecules bound to the top of the water surface. The center of the $SO_2$ density distribution is further into the gas phase than for the neat-water surface with a single-$SO_2$ molecule. Additionally, the water profile is broader in the saturated system. This indicates that water penetrates into the $SO_2$ layer, and moves further into the gas phase than under the neat-water conditions. Because of the limitations of the classical model in accurately reproducing the first hydration shell around the $SO_2$, we do not draw specific conclusions about the hydrated surface complex's geometry. However, the surface affinity of the hydrated $SO_2$ is well reproduced by both the classical and ab initio methods.[107]

### 4.4. Equilibrium Simulations of Adsorbed $SO_2$

Geometric analyses were performed to characterize the net molecular orientation of $H_2O$ and $SO_2$ molecules at different depths from the water surface location. At each distance from the surface location, an orientation profile was created for both the $H_2O$ and $SO_2$ molecules. The bivariate orientation distributions for the angles $\theta$ and $\phi$ at various depths were combined to form the intensity plots that show how the molecular orientation distributions change with distance to the surface location. These plots (Figures 4.6., 4.7., and 4.8.) allow for a visual interpretation of how the net orientations are affected when moving from the gas phase through the interfacial region and to the surface location, and then further into the aqueous interfacial region and bulk. Both the neat-water, with only a single $SO_2$ introduced, and the high-concentration saturated system were analyzed. In the case of the neat-water system, the introduction of a single $SO_2$ does not greatly affect molecular orientation of water molecules in the interfacial region. These results of the water orientation are very similar to a neat-water system without any adsorbed solutes (not shown).

The depth profile plots are arranged as a grid of 2D histograms. Each histogram is calculated for all molecules falling within a particular depth in the water interfacial region. The depth of each plot is marked (in Å) in the upper-right, with the water surface location set at 0 Å, positive depths lie on the gas-phase side of the surface, and negative depths are on the bulk water side. The horizontal axes of each histogram represent $\theta$ values, and the vertical axes represent $\phi$ values. The populations of the distributions are normalized such that areas of low intensity appear in dark blue (0.0), and highest intensity in dark red (1.0). Regions of the plots where the intensity (coloration) is equally distributed along either the vertical or horizontal axes are considered isotropic in $\phi$ or $\theta$, respectively. Likewise, areas of the plot with high intensity over a small orientational range are considered to exhibit an orientational preference at the given depth. The angle distributions from both simulated slab surfaces were averaged for all the orientation analyses.

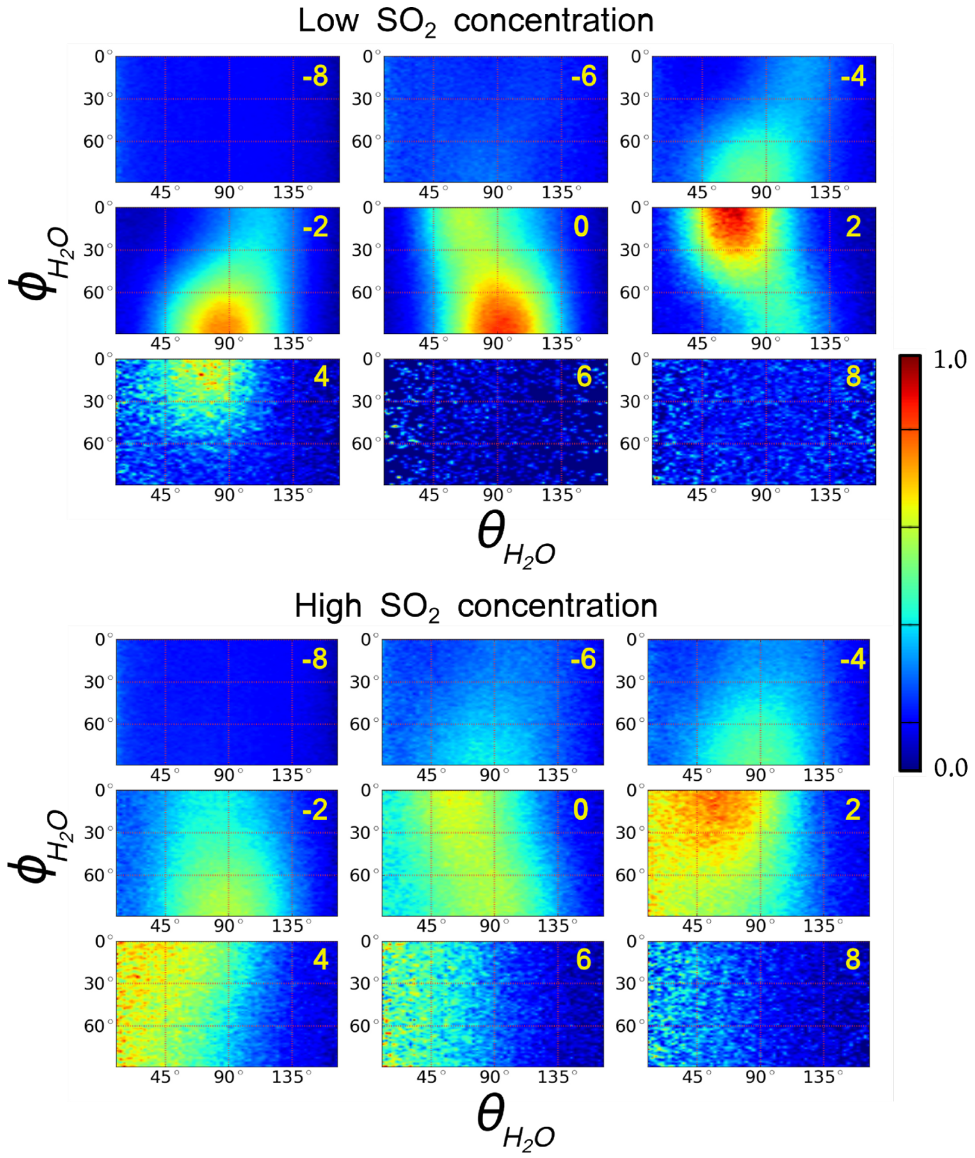

FIGURE 4.6. Molecular orientation histograms of $H_2O$ throughout the surface equilibrated systems at various depths.

### 4.4.1. $H_2O$ Orientation

The orientation depth-profiles for $H_2O$ are shown in Figure 4.6. for both the neat-water (top) and saturated (bottom) systems during the equilibrium MD simulations. The interfacial region for both these calculations and the VSF experiments is defined

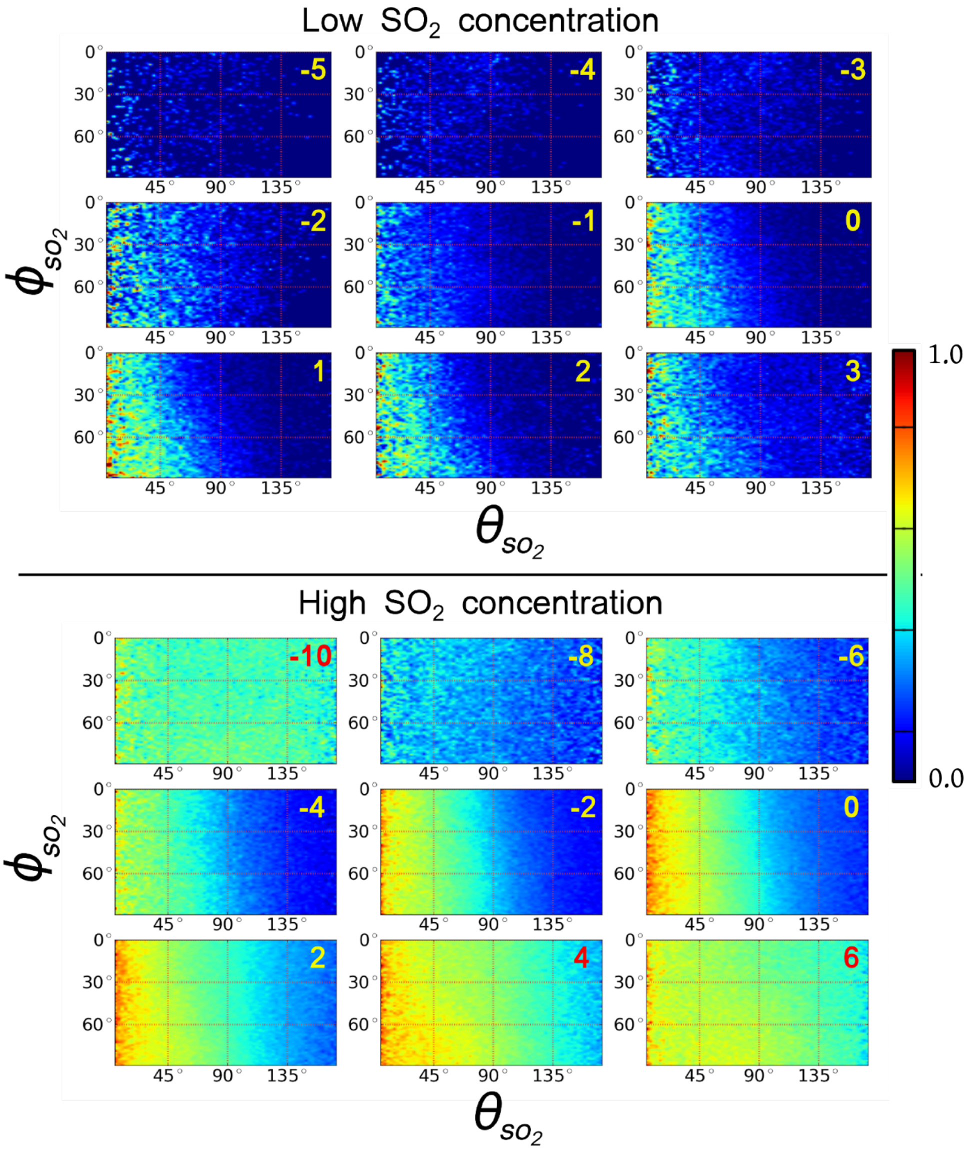

FIGURE 4.7. Molecular orientation distributions for $SO_2$ molecules adsorbed to the water slab surface.

as the region where molecular orientational anisotropy exists around the surface water location. Fitting the water density profiles we have calculated an interfacial width of approximately 10 Å for the neat-water system, and approximately 16 Å for the saturated system. In both systems the strongest orientational preference is found at the slab surfaces (positions near 0 Å). Previous work on orientational preference of water at air surfaces shows the same trend as the neat-water results here.[45, 47] The swaths of coloration indicating high intensity appearing in the neat-water plots from -4 to +4 Å, (and the corresponding regions in most of the saturated system plots) show the overall preference of water to orient at the surface. The plots of the neat-water and saturated systems are similar to each other with a narrow region of reorientation, but the effect in the interfacial region is greater in the neat-water system as evidenced by the sharper transition in intensity from blue to red, compared to the saturated system that has a less pronounced intensity change over larger areas of the histograms.

The bisector tilt of the water molecules, $\theta$, concentrates around $\theta = 90°$within the first few Å above and below the water surface location, becoming progressively isotropic further through the interfacial region and into the water bulk of both systems. Above the surface location at positive distances, $\theta \leq 90°$ indicates that the water hydrogens tend to point towards the gas-phase side of the surface. As the tilt nears $\theta = 90°$ the $H_2O$ bisector lies within the plane of the surface indicating a water orientation either flat on the surface, or with some amount of "twist" sending the OH bonds in towards, or out of the bulk. The value of $\phi$ determines the "twist" in this case. Both systems show a similar trend where waters at or just below the surface have values of $\phi$ near 90°, and waters above the surface take on values of $\phi$ near 0°. This jump in the angular distribution of $\phi$ indicates that waters at or below the surface lie mostly flat in the plane of the interface, and as they move above the surface towards the gas phase, they reorient with one OH bond pointing towards the water bulk, and one pointing out of the surface into the gas. This behavior is more strongly pronounced in the neat-water system where most of the surface waters are not interacting with an adsorbed layer of $SO_2$ molecules.

Although the plots show overall similarities for both the neat-water and saturated systems, the presence of a layer of adsorbed $SO_2$ molecules alters the orientation of those waters furthest into the gas phase. For the saturated solution, the resulting orientation of waters above 0 Å, shown in the bottom set of plots of Figure 4.6., is nearly isotropic in $\phi$, and with $\theta \leq 90°$. This results from waters with bisectors pointing further into the adsorbed $SO_2$ gas layer, and both hydrogens pointing outward from the aqueous bulk. The effect is more pronounced as the waters move further from the water surface, and above 4 Å the $\theta$ distribution is mostly concentrated around $\theta = 0°$(see Figure 4.4.).

The angle distributions above 6 Å in the neat-water plots of Figure 4.6. are mostly isotropic (manifested as uniform coloration throughout the range of orientations). Furthermore, there are few data points that make up the histograms, a result of fewer waters venturing beyond those extents. Conversely, waters near a layer of adsorbed $SO_2$ venture further above the water surface location relative to the low $SO_2$ concentration, where they can have interactions with the adsorbed $SO_2$ gas molecules. The waters above the water surface location orient perpendicularly to the interface. This is consistent with the experimental VSFS studies which showed evidence for the reorienting behavior of water due to the $SO_2$ interactions with the topmost surface waters.[18]

The distribution of $\phi$ is more sharply defined (i.e. less isotropic) for the neat-water system than for the saturated one. Waters on the neat surface lie flat or perpendicular to the surface if they are below or above the water surface location, respectively. The presence of the $SO_2$ allows a greater range of “twist” for those waters in the plane of the interface. The $\phi$ distributions quickly become isotropic above the saturated water surface location, shown as a uniform coloration across $\phi$ for most values of $\theta$.

### 4.4.2. $SO_2$ Orientation

Orientation distributions of the adsorbed $SO_2$ molecules were created during the equilibrium simulations for both the neat-water and saturated systems. Figure 4.7. shows the 2D distributions of $\theta$ and $\phi$ (arranged similarly to the water orientation distributions plots in Figure 4.6.) The $SO_2$ orientation data set for the neat-water system is much smaller as only a single $SO_2$ molecule was simulated in the bulk. The resulting distribution plots are thus representative of the single surface active $SO_2$ molecule. The neat-water $SO_2$ molecule remains within a narrower region of the interface than the saturated system $SO_2$, but effective comparisons can still be drawn. Note that the depth range of the plots in Figure 4.7. is different for the neat-water and saturated systems reflecting the surface mobility of the $SO_2$ molecules in the two systems.

In the interfacial region the angular distribution of the single $SO_2$ (in the neat-water system) is concentrated primarily in $\theta < 90°$. The peak of the distribution occurs at $\theta = 0°$. This indicates that the $SO_2$ bisector points out of the water surface, with the sulfur atom pointing towards the aqueous bulk, and the two oxygens pointing into the gas phase. This same distribution occurs in the saturated system for depths below the surface location, $< 0\,Å$. Beyond $4\,Å$ above the surface, both distributions become mostly isotropic, either because the $SO_2$ does not venture into the gas in the neat-water system, or because of the nature of the adsorbed $SO_2$ layer in the saturated system. Promixity to the water surface highly orients the $SO_2$ bisector.

The distributions of $\phi$ are isotropic in both systems at all depths. Because the $SO_2$ bisector near the surface is oriented perpendicularly to the interface, the isotropy in $\phi$ is expected. Further from the water surface where the bisector orientation becomes isotropic, the $\phi$ distribution remains isotropic. For the surface $SO_2$ orientation, the $\phi$ angle does not provide further information regarding the surface behavior or orientational preference.

### 4.5. Steered MD Transit Simulations of Adsorbing $SO_2$

The orientation of $SO_2$ molecules throughout the aqueous adsorption process was monitored during the transit SMD simulations. The angles $\theta$ and $\phi$ of the transiting $SO_2$ (Figure 4.4.) were calculated for each timestep of the SMD simulations as the $SO_2$ was pulled into the water slab from the gas phase, both in the neat-water and saturated slab systems. The orientation depth-profiles were collected for the 50 simulations of both systems for various distances from the water surface location, resulting in the 2-dimensional angle and depth-profile histograms shown in Figure 4.8.

From its starting position above the water surface, until the $SO_2$ moves to within 6 Å of the water surface location of both systems, the orientation is isotropic in $\theta$ and $\phi$. Isotropic orientation is manifested in the plots as mostly uniform coloration at a given distance from the surface independent of $\theta$ or $\phi$. Near and into the interfacial region the bisector angle $\theta$ becomes more perpendicular to the water surface ($\theta \approx 0°$) with the $SO_2$ sulfur pointing into the water phase, consistent with the equilibrium MD simulation results above. At the point when the $SO_2$ reaches the water surface location (0 Å), the bisector is perpendicular to the interface in both the neat-water and saturated systems. In the absence of simulated ionic species that form through

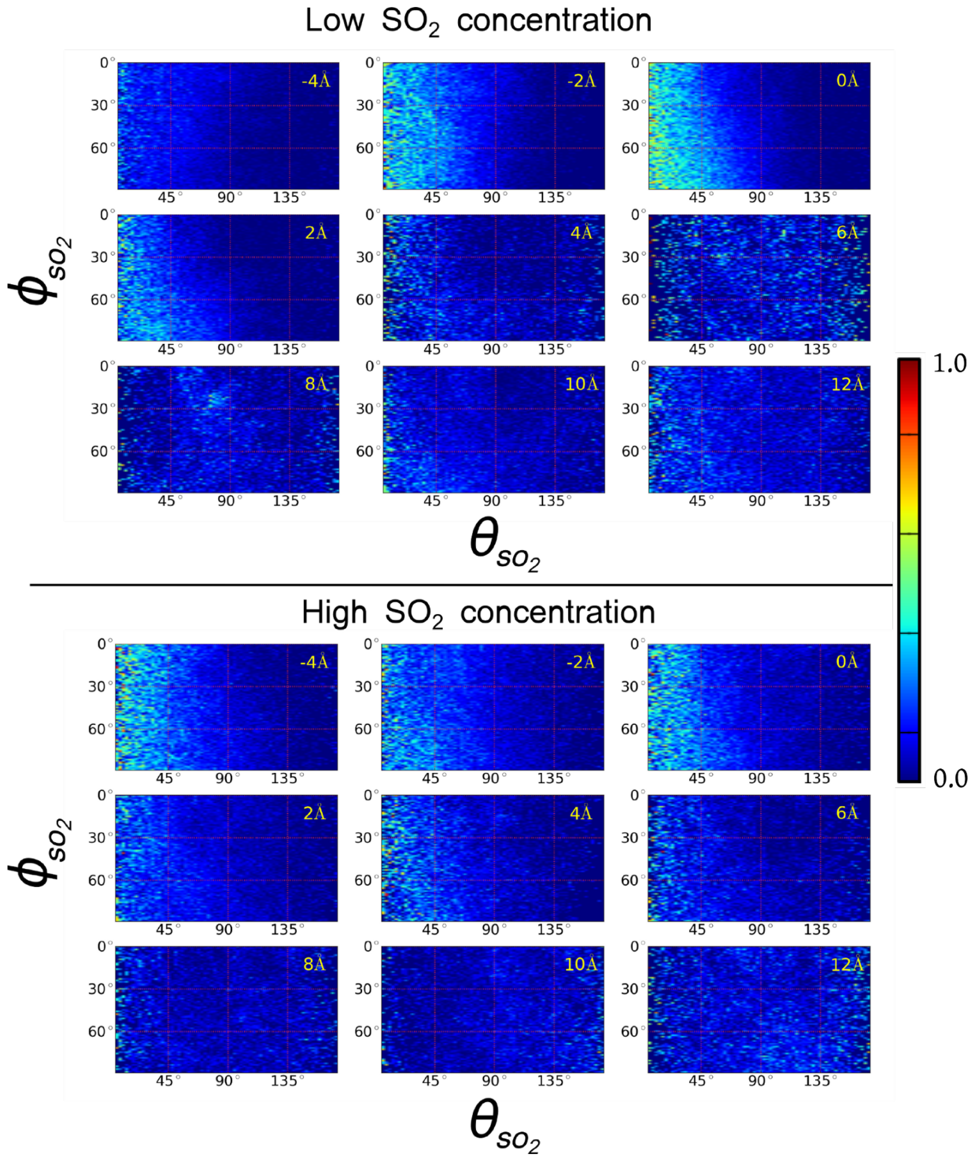

FIGURE 4.8. Molecular orientation distributions of an $SO_2$ at different interfacial depths of an aqueous slab during SMD transit simulations.

$SO_2$-$H_2O$ chemistry at the surface, it is clear that the adsorbing $SO_2$ in the gas phase takes on a preferred orientation to adsorb on a water surface. The main difference between the neat and saturated water systems is where the point of the transition from isotropic to preferred orientations is found.

Comparing in more detail the difference in these two systems upon $SO_2$ approach, for the neat-water surface, a transition occurs at approximately 4 Å above the surface water location. Below 4 Å above the surface, $SO_2$ has a preferred net orientation and is close enough to the water surface that it begins to interact with the topmost surface waters. In the saturated system, the same trend occurs, however the onset of the perpendicular orientation begins at approximately 8 Å above the surface. The layer of adsorbed $SO_2$ already present in the saturated system most likely interacts with the transiting $SO_2$ molecule. Also, topmost water molecules from the surface move up to a few Å inside the adsorbed $SO_2$ layer and interact with the transiting $SO_2$ further from the surface than those in the neat-water system. It is remarkable that the orientational trend appears so strongly in the $\theta$ plots even with so little data as was collected from the single $SO_2$ molecule of each simulation. From onset of orientation above the surface until 10 Å below (not shown), the $SO_2$ holds a preferred orientation.

With a mostly perpendicular bisector angle, it is expected that the values of $\phi$ for $SO_2$ would be isotropic relative to the reference axis. This is the case in both systems, with only a few exceptions. In both systems the $\phi$ profiles exhibit mostly isotropic distributions above 0 Å, with several regions of lighter coloration interspersed, but without a clearly formed orientational trend. At the neat-water surface and just above (from 0-2 Å above the water phase), the $\theta$ profile broadens to $\theta = 90°$, near $\phi = 90°$ appearing as a shoulder of light coloration in the bottom-left of the 0-2 Å axes. This indicates that $SO_2$ inclined up to 90° from the surface normal will have a preferred $\phi$ orientation lying more flat to the water surface. This is in contrast to $SO_2$ molecules above the water surface location, oriented more perpendicularly and without a preference for a particular range of values in $\phi$. The behavior is likely due to the interaction between the waters and the S-O bonds leading to a higher solvation than above the water surface location. As the $SO_2$ is solvated by more highly-coordinated bulk water, the S-O bonds experience less equal interaction environments. Baer et al. noted that their force field model for the $SO_2$ does not reproduce well the first hydration shell geometries,[107] so conclusions regarding the specific interactions and hydrate geometries between the $SO_2$ and $H_2O$ cannot be made here. It is notable that the same reorientation does not occur as strongly in the saturated system. The presence of the adsorbed $SO_2$ layer apparently decreases the reorienting behavior likely because of the disrupting effect the higher $SO_2$ concentration has on the water interactions in the interfacial region.

### 4.6. Summary

Gaseous adsorption on solid surfaces has been extensively studied over the past few decades with much learned about how molecular geometry and orientation of the adsorbate are influenced by the proximity of the solid slab. For a liquid surface where the surface slab is no longer rigid but has molecules with considerable freedom of movement, the surface and approaching gas molecules can be active partners in attaining the optimal geometry and orientation necessary for adsorption and subsequent uptake. And unlike the solid surface defined by a sharp plane, the interfacial region for the liquid-gas system is much broader, extends on either side of a defined center plane, and is host to a broad distribution of gas-liquid molecular geometries and orientations that change as the gas molecules transit through the interfacial region into the bulk liquid. Although the current molecular level understanding of the complex dances that these molecules play in this fluid interfacial region is in its infancy, emerging studies such as these are beginning to provide unique new insights that are key to understanding many environmentally important processes at aqueous surfaces.

Presented herein are the results of several classical molecular dynamic simulations that focus on understanding how surface water molecules and adsorbing $SO_2$ gas molecules twist and turn as the gas adsorbs and transits the interfacial region. The computational studies emulate and expand on the experimental spectroscopic studies from the Richmond laboratory which have found $SO_2$ surface complexation at a water surface.[16–18] These spectroscopic studies show clear evidence of $SO_2$-water surface complexation but details about this surface complex could only be inferred from spectral changes in the surface water spectrum since $SO_2$ could not be monitored directly. These simulations do not have that limitation and hence can provide information about the behavior of both surface partners and in particular, how their proximity influences the orientation behavior of each other. The orientational information obtained in these simulations are provided via calculated depth profiles which show the molecular distribution of orientations of the two different interfacial molecules throughout the dimensions of the interfacial region.

The simulations show that gaseous $SO_2$ quickly adsorbs to the water surface and continues to bind until a complete surface coverage is reached. Surface waters reorient in the presence of adsorbed $SO_2$. The waters at and just below the interface of a neat-water surface tend to lay flatter to the surface than when a saturating layer of $SO_2$ is present. The waters above the surface location or interacting with the layer of adsorbed $SO_2$ orient more perpendicularly to the interface, and further expose their “free-OH” uncoupled bonds for interactions with $SO_2$, and hydrate complex formation. Furthermore, we have found that surface waters underneath a blanket layer of adsorbed $SO_2$ will penetrate further into the gas phase, allowing for greater mobility of waters away from the aqueous bulk in the presence of $SO_2$.

Through these simulations it is also possible to characterize the orientational behavior of $SO_2$ during and after adsorption. The equilibrium neat-water simulations show that a single $SO_2$ molecule, representing a low concentration, has a high surface affinity. At a high $SO_2$ concentration in the saturated systems, $SO_2$ molecules are also surface active, and are found further out of the water phase than at the lower concentration. These $SO_2$ molecules form a bound layer that crowds the surface and interacts with the surface waters. The orientation of $SO_2$ on the water surface was found to be similar for both low and high concentrations. Those $SO_2$ molecules at or below the surface water location strongly orient with the sulfur atom pointed in towards the water bulk, and the oxygen atoms out towards the gas phase. The $SO_2$ molecules slightly above the water surface lose this net orientation within 6-8 Å. Those molecules further from the water are more isotropically oriented. Figure 4.9. depicts what the neat-water and saturated surface molecules look like for both $SO_2$ and $H_2O$ orientations and locations based on the calculations.

Steered molecular dynamics simulations were used to model the behavior of an adsorbing $SO_2$ as it moves from the gas phase above the water down through the surface and into the bulk. The $SO_2$ reorients as it makes its first contact with the water interface. Within 4 Å of the surface the $SO_2$ is mostly oriented with its sulfur towards the water phase. The results for the transit through the interface show that in both systems of low and high $SO_2$ concentration an adsorbing $SO_2$ near the interface has very similar orientation to those molecules already bound to the water surface. The $SO_2$ pulled further into the water bulk retains its orientation until it is past the interfacial region and then isotropically orients with the bulk water.

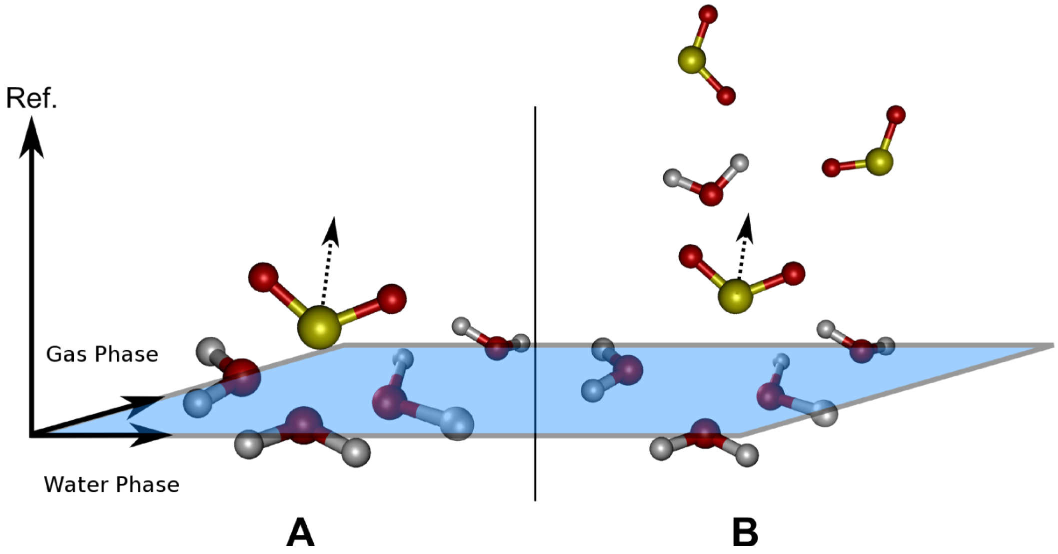

FIGURE 4.9. Proposed orientations of $H_2O$ and $SO_2$ in the regions near the (A) neat-water and (B) saturated liquid-gas interface.

These studies provide a starting point for future studies in this area that seek to understand how gases of different concentrations and chemical composition adsorb and transit across an aqueous/air interface. Obtaining such knowledge will be invaluable for understanding many environmental aerosol and land water systems where gaseous uptake at a water surface does not conform to expectations.[99, 101, 106, 118]

Chapter V documents the follow-up DFT-MD study that further examines surface-bound $SO_2$. The $SO_2$ molecule behavior and its hydration interactions with neighboring waters are probed in depth, and a unique bonding behavior is presented. Two parallel groups of simulations were created at two temperatures to model both laboratory and atmospheric conditions.

# CHAPTER V

# SULFUR DIOXIDE SURFACE HYDRATION BEHAVIOR

This work was submitted for publication and is under review for the Journal of Physical Chemistry C. Dr. Geraldine Richmond supplied computational resources and project support. Eric Shamay was the principle investigator for this work.

## 5.1. Introduction

The molecular nature of the adsorption of gas molecules onto a water surface is one of the remaining largely uncharted territories of surface chemistry. Although gas uptake into aqueous systems occurs often environmentally and industrially, we still know very little about the process and the details of the adsorption reactions, and certainly less than what we know about gaseous adsorption on a solid surface. How does a gas initially bind to a water surface, and what steps are involved in the subsequent adsorption? How does an unbound gas molecule near a water surface affect the water to which it will bind? What is the structure of hydrating waters in the surface region, and how does a hydrated solute molecule behave differently than as a gas? Experiments to address these questions provide valuable information, but have to date never fully characterize microscopic events and behaviors. However, these systems can be fully characterized computationally, and when coupled to the previous experimental work can provide a much more complete picture of gaseous adsorption to aqueous surfaces.

$SO_2$ is a particularly important gas to use as a starting point and model system because of its importance in commercial and environmental systems. [95, 96, 99, 106, 119, 120] Its simple molecular structure, high solubility in water, and relative abundance make it a pivotal compound in numerous aqueous atmospheric reactions. A complete picture of the $SO_2/H_2O$ adsorption process will aide in understanding gaseous adsorption on the many aqueous surfaces in the environment, as well as in understanding the fundamental nature of gases in water's surface region.

The work documented in this chapter makes use of ab initio quantum molecular dynamics (MD) techniques to model and simulate the hydrating structures that form around a surface-bound $SO_2$ on water. A dynamic water surface is simulated, complete with all the extended hydrogen-bonding interactions that capture the variability of the $SO_2$ hydrate structures, and the behavior of the water surface molecules. The quantum MD technique described herein allows more accurate and realistic simulation than the classical MD of $SO_2$described in chapter IV.[19] It is also superior to small cluster DFT studies because it does not assume geometry optimized configurations, and the extended interactions of a water slab are incorporated. The previous classical MD study determined the net orientational behavior of $SO_2$ binding to a water surface, and the orientation of the waters as they respond to the presence of an adsorbing gas. Understanding the orientational behavior of molecules in the aqueous interfacial region during adsorption was a necessary first step to understanding the specific details of gas-binding and surface behavior.

Quantum MD techniques are the logical follow-up as they accurately reproduce the hydration geometry around the bound $SO_2$ molecules, and allow us to examine in detail the specific bonding interactions that occur within the surface hydrates, and in the extended bonding further into the water.[107] Two parallel studies are performed in this project; one is done at 300K, and one at the more atmospherically relevant cold 273K. This set of temperatures complements the most recent experimental studies that showed the binding of gaseous $SO_2$ to a water surface is greatly enhanced at cold temperatures.[18] Other experiments by the Richmond laboratory developed the picture of $SO_2$ adsorption, and showed that $SO_2$ surface hydrate complexes form when a water surface is exposed to $SO_2$ gas.[16, 17] Although conclusions regarding the specific nature of those complexes could only be inferred from the experiments, the current computational studies now provide insights about the specific microscopic geometries and behaviors of the hydrating complexes.

This is likely the first temperature study using quantum MD to study the binding of small gas molecules on a water surface. It is shown how temperature affects the bonding behavior of the surface-adsorbed $SO_2$ to neighboring waters, and a sequential binding mechanism for $SO_2$ adsorbing to a water surface is proposed. Also, $SO_2$ binding behavior is examined when bound to surface waters. Lastly, analysis of a specific bonding arrangement demonstrates an extended bonding structure of $SO_2$ hydrates, as they are seen to preferentially form an extended cyclic ring structure through intermolecular bonds.

### 5.1.1. Bonding Coordination

A hydrated $SO_2$ in an aqueous environment forms hydrogen bonds through the oxygens to nearby water-hydrogens, or interacts via the sulfur atom with water-oxygens.[107, 121, 122] To further analysis of the way in which $SO_2$ coordinates its bonding to surface waters (those that lie in the topmost region of a gas/water interface), a naming scheme is adopted to denote the way in which the $SO_2$ is hydrated by the surrounding waters. This naming scheme mimics a notational system developed during a previous study on water coordination by Buch et al.[123] and was subsequently used in more recent computational work.[47] In this naming system, a letter is used to designate the atom on a water molecule through which a hydrogen bond is formed to neighboring waters. Thus a bonding coordination of “OOH” designates two proton-acceptor bonding interactions through the water-oxygen, and a single proton-donor bonding interaction through a hydrogen. More recently, Baer et al. devised a nomenclature that explicitly enumerates the bonding to $SO_2$ via the sulfur or oxygen atoms.[107]

This work adopts a similar nomenclature scheme for $SO_2$ in order to quantify hydrogen bonding through the acceptor $SO_2$-oxygens, and the weaker bonding interactions from the $SO_2$-sulfur to water-oxygens. Thus, an “SOO” coordinated $SO_2$ molecule forms a single interaction through the sulfur atom to a neighboring water-oxygen, and two hydrogen bonds through either a single $SO_2$-oxygen, or distributed with one hydrogen bond on each of the $SO_2$-oxygens. Analysis of the distribution of these various $SO_2$ coordinations will give insight to how $SO_2$ binds to the water surface.

To determine $SO_2$ bonding coordinations, intermolecular bonds are defined using the distance criteria of Baer et al.[107] The bond-length definition is based on a set of distance criteria where a bonding interaction between a $H_2O$-oxygen and $SO_2$-sulfur is formed at a distance less than 3.5 Å, and an $SO_2$-oxygen hydrogen bond to a $H_2O$-hydrogen is formed at a distance less than 2.2 Å.

### 5.1.2. Cyclic Bonding Structures

Hydrated $SO_2$ clusters have been studied extensively with several recent experiments and computations forming a clearer picture of $SO_2$ bulk and surface behaviors.[16–18, 91, 99–101, 107, 121, 122, 124–127] At a water surface, it is now known that $SO_2$ forms a complex with water during adsorption, and then subsequently absorbs into the interfacial region by reaction to form ionic sulfur species.[16–18] The computational study to elucidate the structure of surface hydrated $SO_2$ by Baer et al. showed that the bonding coordination distributions of $SO_2$ at the surface are altered relative to the bulk region, and that two coordinations dominate the distribution of bonding types: the “SO” and the “SOO”. In the same work they then focused on the dominant coordination to determine the most likely cluster geometry of di- and tri-hydrate species of $SO_2$. However, that study, and others probing specific hydrate structures, were performed in gas phase, under idealized conditions following geometry optimizations. None of the studies have yet focused directly on the presence of an extended hydrating structure involving $SO_2$ molecules at a water surface, forming closed rings of molecular interactions. Here, ab initio molecular dynamics are utilized to recreate a microscopic water surface environment. By focusing on the occurrence of a specific subset of $SO_2$ bonding coordination types, it is possible to probe directly a certain hydrated $SO_2$ in an aqueous interfacial environment.

The gas phase cluster geometries predicted in the study by Baer et al. imply a cyclic bonding structure through the two or three hydrating waters. “Cyclic” here is used to denote a closed loop formed by the intermolecular hydrogen bonds, S-O interactions, and covalent bonds of the molecules involved. Figure 5.1. depicts one such cyclic structure showing the bonds beginning on the sulfur and returning through a $SO_2$-oxygen.

### 5.1.3. Graph Theoretical Details

As noted above, the optimized geometry of the gas phase $SO_2$ hydrates suggests cyclic bonding structures. Geometry optimization shows the formation of these cyclic hydrate structures with two or three waters. A different story entirely has the potential to emerge when $SO_2$ is placed in a dynamic environment such as in the

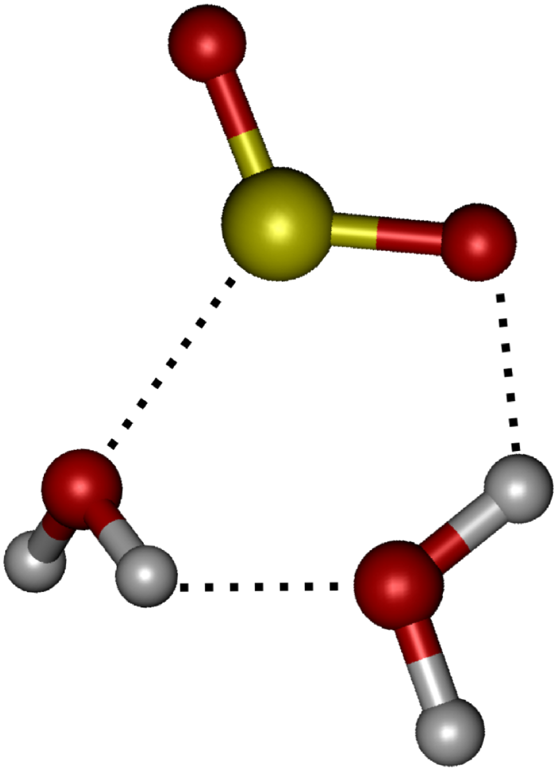

FIGURE 5.1. Example cyclic $SO_2$ hydrate structure, formed by the covalent, S-O, and hydrogen bonds of the two molecule types.

course of MD simulations of an aqueous surface. Do the cyclic structures also form in the course of a dynamic bonding process on a simulated water surface, where extended hydrating structures influence $SO_2$ and water behavior? To study the formation and behavior of cyclic hydrate structures graph theoretical techniques are employed on MD trajectory data. Previous use of graphs in molecular computations were applied to finding stable arrangements of water clusters, ice, hydrogen bonding, extracting topological molecular properties, and cyclic structure studies.[128–133]

Here graph theoretical concepts are briefly introduced. They have been described well by others with varied application to cyclic structures.[129, 132, 134–137] A graph consists of nodes, and edges that connect the nodes. A molecule can be represented with atoms as nodes, and edges for each intramolecular covalent bond connecting the atoms. The set of edges is then further expanded to include intermolecular interactions such as hydrogen bonds and other bonding interactions. Edges may be assigned weights (i.e. bond lengths), types, and can be directional, i.e. pointing from a source node towards a target node. A molecular system including all atoms, bonds, and interactions is thus fully described by a graph.

To detect cyclic structures in a graph a depth-first or breadth-first search (DFS and BFS, respectively) may be used.[138, 139] A graph search is a recursive algorithm of queuing nodes and all neighboring nodes while performing a specified procedure on each visited node. This is easily performed on adjacency list or connectivity matrix data structures, iterating through nodes (i.e. atoms) of interest in the graph as starting points of the search. In graph search terminology, all nodes are colored during graph traversal to distinguish unvisited nodes (white), queued nodes (gray), and visited nodes (black). Performing a BFS on a graph, cyclic structures are detected any time a "gray target" is encountered when queuing adjacent neighbors of a node. A benefit of BFS is the ability to determine the smallest cyclic structure containing a given node. In the case of $SO_2$ hydrate structures, beginning the BFS with the $SO_2$-sulfur as the starting, or root node for the search, will discover cyclic bonding structures in order of size. This scope of analysis here is limited to with the smallest cyclic structure involving those waters in the first and second hydration shells around the $SO_2$. Furthermore, it is possible to reconstruct a cycle's structure by finding its size (number of contributing atoms), and the number of unique waters in the cycle. This allows for distinguishing between various types of cyclic structures encountered.

Several arrangements of cyclic bonding structures are shown in Figure 5.2. for a $SO_2$ molecule with three waters. Cycles with fewer or greater numbers of waters are also possible and encountered during MD. Cycle types I, II, III in Figure 5.2. are cyclic structures in which the $SO_2$ is a member of the cycle. Types IV and V do not involve the $SO_2$ in the bonding cycle, but are commonly encountered as the smallest cycle types formed near the $SO_2$. Type III is of particular interest because the $SO_2$ in this cycle has the most frequently occurring bonding coordination ("SO", as shown later).

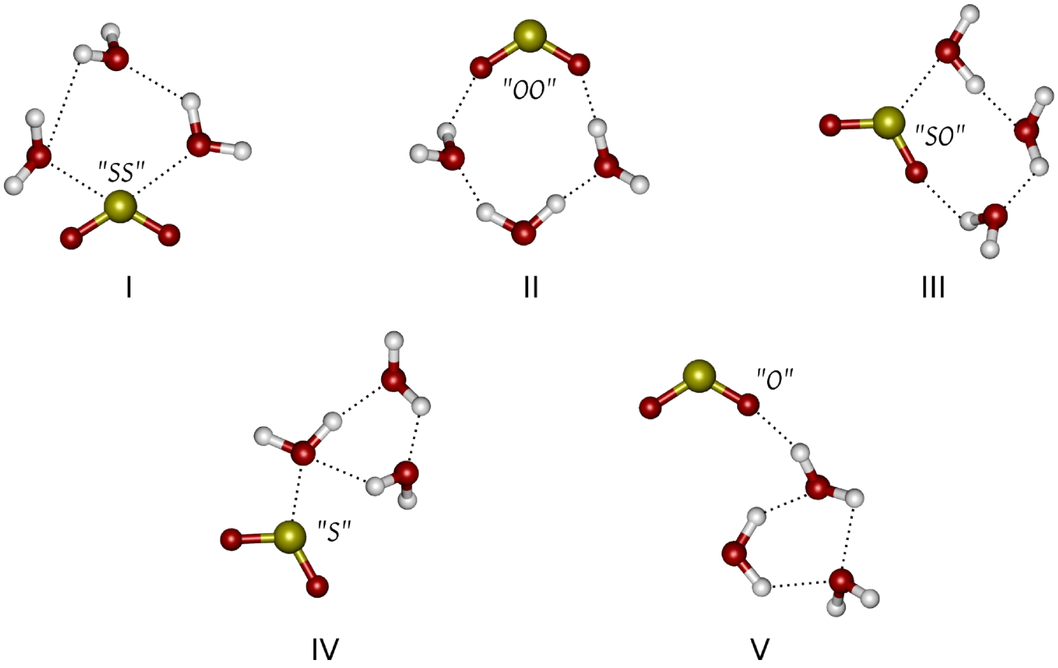

FIGURE 5.2. $SO_2$ in various cyclic hydrate structures encountered during MD simulations with water.

Baer et al. presented a detailed geometric and spectroscopic breakdown of type III cycles with two and three waters from their DFT calculations.[107] Given the information of the number of waters, atoms, and bonds involved in the bonding cycles, of the three-water type III cycles there exist two structural varieties, shown in Figure 5.3., that differ in the set of water atoms involved in the cyclic structure. Type III-A (shown in Figure 5.3.A) is arranged with each water contributing an OH bond to the structure of the cycle. Type III-B involves a single water contributing an OH, whereas the other two waters contribute only the oxygen atom or the entire water molecule to the structure, respectively. This nuance of the type III structures involving three waters, and the overall distribution of structures are presented in more detail later. Also shown is the distribution of cyclic structures encountered during MD simulations to aide in further understanding the behaviors of $SO_2$-hydrates at the water surface.

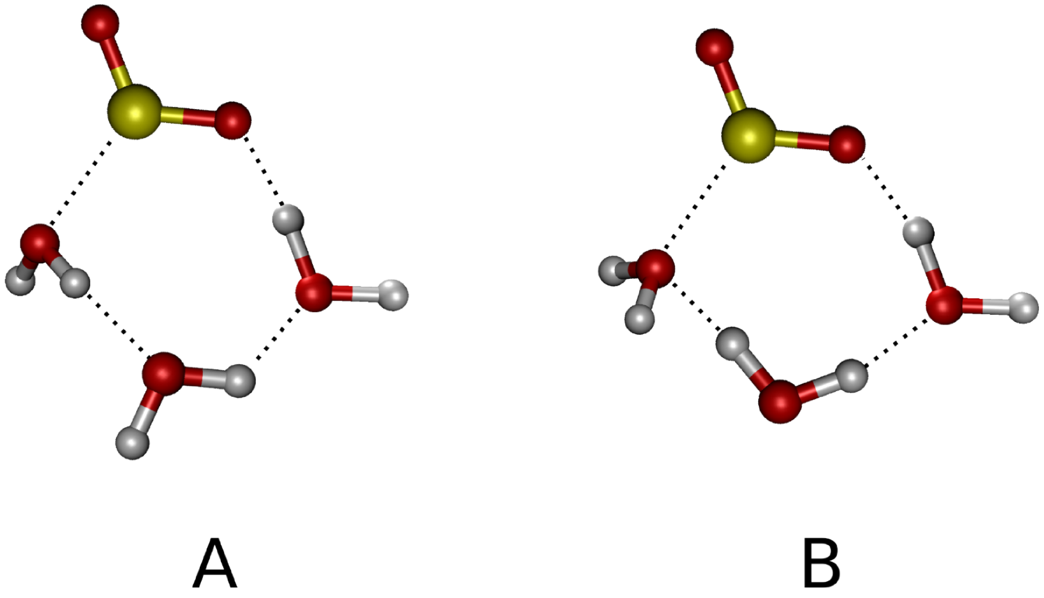

FIGURE 5.3. Two conformations of Type III $SO_2$ cyclic hydrate structures.

## 5.2. Computational Methods

On-the-fly ab initio molecular dynamics simulations were performed with the QUICKSTEP package, which is an implementation of the Gaussian plane wave method using the Kohn-Sham formulation of density functional theory (DFT).[13] The Kohn-Sham orbitals are expanded using a linear combination of atom-centered Gaussian-type orbital functions. The electronic charge density was described using an auxiliary basis set of plane waves. Energies and forces from on-the-fly simulation sampling of the Born-Oppenheimer surface were calculated for each MD step using the Gaussian DZVP basis set, the exchange-correlation functional of Becke, Lee, Yang, and Parr (BLYP),[34] and the atomic pseudo-potentials of the Goedecker, Teter, and Hutter type.[33] A simulation timestep of 1 fs was used, with a Nose-Hoover thermostat set at 273K and 300K for the "cold" and "hot" simulations, respectively. These computational parameters were verified to yield a reasonable description of bulk room temperature water when simulating a neat-water system.

Initially, 10 equilibrated boxes of side-lengths 10.0 Å, with 36 randomly packed water molecules were used. Five of the boxes were used for each of the cold and hot simulations. A sulfur dioxide molecule was randomly placed onto the surface within 2.5 Å of a water molecule centrally located above the waters in the z-axis. A copy of the initial system cubes were then expanded along one axis (z-axis) to 25 Å. The system energy was minimized through a geometry optimization. Subsequently, the system was equilibrated for 1 ns in canonical ensemble (NVT) conditions. Periodic boundaries were set on the two short axes to form an infinite slab. The equilibrated systems were then simulated for a further 20 ps in the microcanonical ensemble (NVE), with trajectory snapshots recorded every 1 fs. The initial 1 ns equilibration trajectory was not included in the final analysis. This simulation process resulted in 20,000 time steps of system trajectory for analysis in each of the hot and cold replicas of the system, for a total of 100,000 timesteps at each temperature.

## 5.3. Sulfur Dioxide Bonding Coordinations

The bonding coordination of each $SO_2$ was determined at each timestep of the simulations. Figure 5.4. shows the distribution of bonding coordinations of the surface

$SO_2$, as a percentage of all bonding coordinations encountered for both the cold (blue) and hot (red) trajectories. A first visual inspection reveals several trends. Clearly the "SO" coordination is the most populous at both temperatures. The second and third most populated coordinations are the "S" and "SOO", however their distributions differ between temperatures. In cold simulations the "S" and "SOO" coordinations occur nearly equally. The hotter temperature simulation shifts the distribution such that the "S" occurs 5% less frequently than in the cold, and the "SOO" occurs nearly 10% more often. The distribution of bonding coordinations in the hot temperature has a clear first and second most frequent coordination: "SO" and "SOO", respectively. These results for the hot (room temperature) system coincide with those of the previous single-temperature simulation study by Baer et al. at a similar temperature.[107]

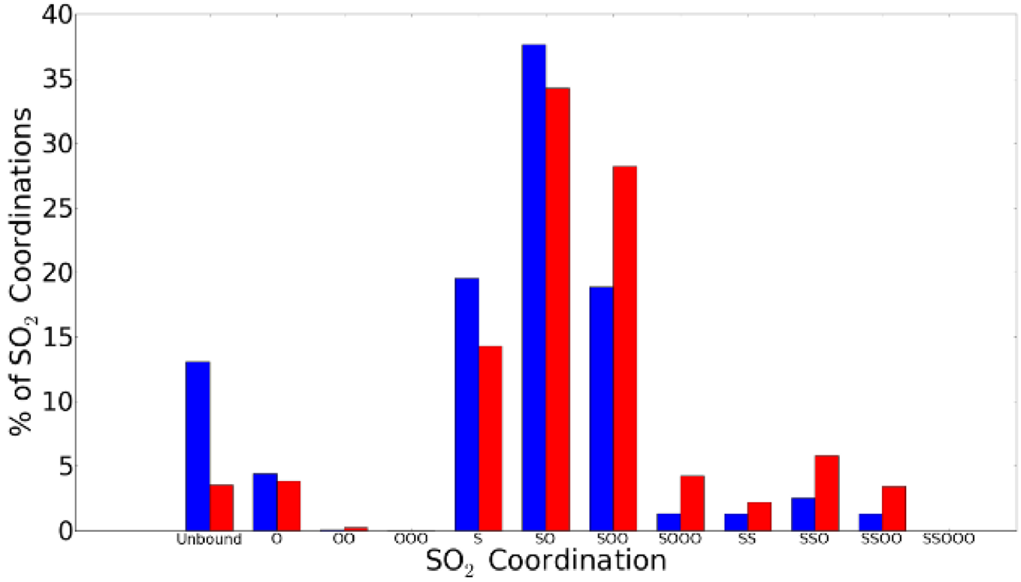

FIGURE 5.4. The distribution of bonding coordinations of the (blue) cold and (red) hot $SO_2$.

Several conclusions about the bonding behavior of $SO_2$ to surface waters stem from this distribution of coordinations. Clearly the cold $SO_2$ spends more time than the hot $SO_2$, 13% versus 3%, respectively, completely unbound from the surface waters. This does not necessarily imply a complete desorption into the gas phase, but only a brief sojourn away from the waters, with all interactions and bond lengths longer than the cutoff criteria used for the analysis. Furthermore, the most frequently occurring bonding coordinations are "S","SO", and "SOO", with "SO" being the most populated at both temperatures. Baer et al. also concluded that these three coordinations were the most frequent for a room temperature simulation, and specifically identified the "SO" and "SOO" as most common in their study.[107]

Looking closer at the coordination types it is notable that coordinations lacking any sulfur interactions (e.g. "O", "OO", etc.) represent the least frequently formed. A bonding coordination with at least a single sulfur interaction is clearly favored over $SO_2$ "oxygen-only" bonding to waters. In previous classical simulations of $SO_2$ on water it was concluded that during adsorption and throughout the interface, the $SO_2$ orients so that its sulfur tends to the $H_2O$ bulk side of the interface.[19] The coordination distributions here support the idea that binding through the sulfur is preferable, to the extent that a non-sulfur coordination is rarely formed during the course of all the simulations.

Baer et al. performed this coordination analysis for their single-temperature study, but discriminated between $SO_2$ binding through the two different oxygens. They concluded that there is asymmetric hydrogen bonding through the $SO_2$-oxygens, with one oxygen binding more often than the other. This is supported by the findings here where all the double oxygen coordinations (e.g. "OO", "SOO", etc.) represent a much lower percentage of the coordinations than the single oxygen counterparts (e.g. “O”, “SO”, etc.). Furthermore, a triple-oxygen coordination (e.g. “OOO”, “SOOO”, etc.) is very rarely encountered. Three $SO_2$-oxygen bonds only form if both $SO_2$-oxygens are interacting with water hydrogens. These findings, that triple-oxygen coordinations rarely form, complement the conclusion of Baer et al. about the asymmetry in the oxygen interactions.

Having established the preference for an interaction through the $SO_2$-sulfur atom, the right side of Figure 5.4. is examined at the double-sulfur coordinations (e.g. “SS”, “SSO”, “SSOO”, etc.). From the data it is clear that single-sulfur coordinations are overwhelmingly preferred over double-sulfur ones. Adding a third oxygen atom is also unfavorable as the “OOO” and “SSOOO” together represent less than 1% of the trajectories, and the comparison between “SOO” to “SOOO” shows a very large decrease in occurrences.

A picture can now be formed of a typical $SO_2$ molecule adsorbed to a water surface across both temperatures in this study. The $SO_2$ will have at least one interaction to neighboring waters through the sulfur, and will then bond asymmetrically through one of the oxygens either once or twice to water hydrogens. The $SO_2$-oxygen bonds will form and break repeatedly throughout a trajectory, and overall the most dominant coordination will be the “SO” bonding arrangement.

### 5.3.1. Temperature Effects on Bonding Coordinations

The binding behavior of the $SO_2$ is altered by changing the temperature of the system, as evidenced in the shift in bonding coordination populations of Figure 5.4. from cold to hot. In the cold temperature, the unbound, “S”, and “SO” coordinations are more populated than in the hot systems. The increased temperature decreases the time spent in the unbound coordination, and causes all the coordinations to the right of “SO” in Figure 5.4. to increase over the equivalent cold temperature populations. As shown, the cold $SO_2$ spends nearly four times as much time unbound as the hot $SO_2$, with most of the unbound population in the hot simulations shifting to coordinations with double-oxygen and double-sulfur bonds.

On the cold water surface, the “S” and “SO” are more populated than for the hot system. The relative decrease of these coordinations are matched in the hot surface by an increase of the “SOO” configuration. This speaks to a dramatic difference in the surface behavior of $SO_2$ at the two temperatures. The cold $SO_2$ spends nearly equal time in the “S” and “SOO” coordinations, but nearly 20% more time in the “SO”. Thus, the addition or removal of a bond through the $SO_2$-oxygen to a neighboring coordination (e.g. addition of an oxygen bond from “SO” to “SOO”, or removal of the bond from “SO” to “S”) is equally probable, as long as the sulfur interaction with the water oxygen does not break.

Figure 5.5. shows the radial distribution functions (RDF) of $SO_2$ to water atoms for both cold (blue) and hot (red) temperatures. The S-$O_{H_2O}$ RDFs are nearly equal except for a slightly taller first peak in the cold system. Along with the slightly larger population of the cold “S” and “SO” coordinations in the cold surface, the RDF indicates that since bonding occurs frequently through the sulfur, the cold $SO_2$-sulfur interacts more closely with the surface waters. In the hot systems, the bonding coordinations with two oxygen bonds (e.g. “SOO”, etc.) occur more frequently than in the cold system. This additional bonding through a second oxygen interaction may slightly shift neighboring hydrating waters away from the $SO_2$-sulfur towards the oxygen end of the molecule. This suggests that the cold $SO_2$ bonds closer to the surface waters through its sulfur atom (as shown in the S-$O_{H_2O}$ RDF) and favors the more “sulfur-centric” bonding coordinations (e.g. “S”, “SO”). The

increased temperature of the hot system allows the $SO_2$ to bond more extensively through its oxygens to the "SOO" coordination. The greater interactions through the oxygens, and higher bonding coordination, may pull the $SO_2$ further into the water interface and then allow for increased bonding through the sulfur, up to double-sulfur coordinations (e.g. "SS", "SSO", etc.).

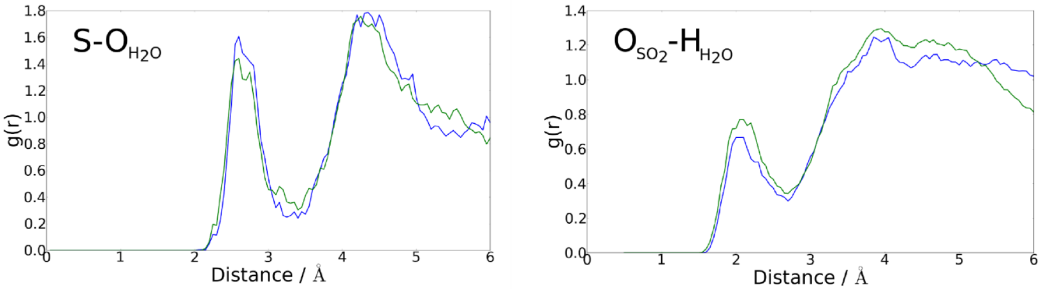

FIGURE 5.5. RDFs of (blue) cold and (green) hot simulations. (left) $S_{SO_2}$–$O_{H_2O}$, and (right) $O_{SO_2}$–$H_{H_2O}$.

### 5.3.2. Bonding Transitions

During the course of each simulation, the $SO_2$ bonding coordination was determined and recorded for each timestep. From the coordination data, not only are the populations of the various bonding coordinations extracted, but also the frequencies of transitions between the different coordinations (i.e. the number of times each $SO_2$ switched from one coordination type to another). This data allows for generation of the directed graphs of Figure 5.6. depicting the cold and hot (Figure 5.6. A and B, respectively) bonding coordinations as circular colored nodes.[140, 141] The transitions between the coordinations are depicted as directed edges pointing in the direction of the transition from one bonding coordination to another. The populations of the coordinations are depicted by both the node size and coloration (larger and darker red coordinations occur more frequently). Populations of the transitions between coordinations are depicted by arrow thickness, with thicker lines corresponding to more frequent transitions. Additionally, the transition lines are numbered to the right of each line with the number of times each transition occurred.

As expected for the more populated coordinations, there are more transitions between larger nodes in Figure 5.6. than transitions to less populated coordinations. Insights to the bonding process are made clearer from these graphs. In the cold system graph of Figure 5.6.A the majority of transitions are between the "S-SO" and "SO-SOO" nodes. The number of transitions within this "S-SO-SOO" group of bonding coordinations is an order of magnitude larger than any other transition. This indicates that while the $SO_2$ is bound in any of the three most populated bonding coordinations, it is actively binding and unbinding the oxygens to form the other two coordinations in this group. Clearly, the $SO_2$ is rather active and constantly forming and breaking bonds through its oxygens.

In the graph of the hot system in Figure 5.6.B, the transition frequencies follow the same trend as in the cold system, increasing with adjacent node size. One very surprising result is in the transition from "SOO-SOOO". This transition frequency does not follow from the adjacent node sizes, as the "SOOO" node represents less than 5% of the bonding coordinations. This is indicative of a very rapid cycle of forming and breaking of bonds to the second $SO_2$-oxygen. As noted earlier, it is likely that "SOO" coordinated $SO_2$, asymmetrically binding twice through a single oxygen, is being pulled further into the water interface. It is likely more surrounded by waters, and in the hot system it can more easily form a brief third hydrogen bond to a water through the second $SO_2$-oxygen. Because the triple-oxygen coordination is not as favorable, it quickly breaks the bond and the $SO_2$ returns to the "SOO" coordination.

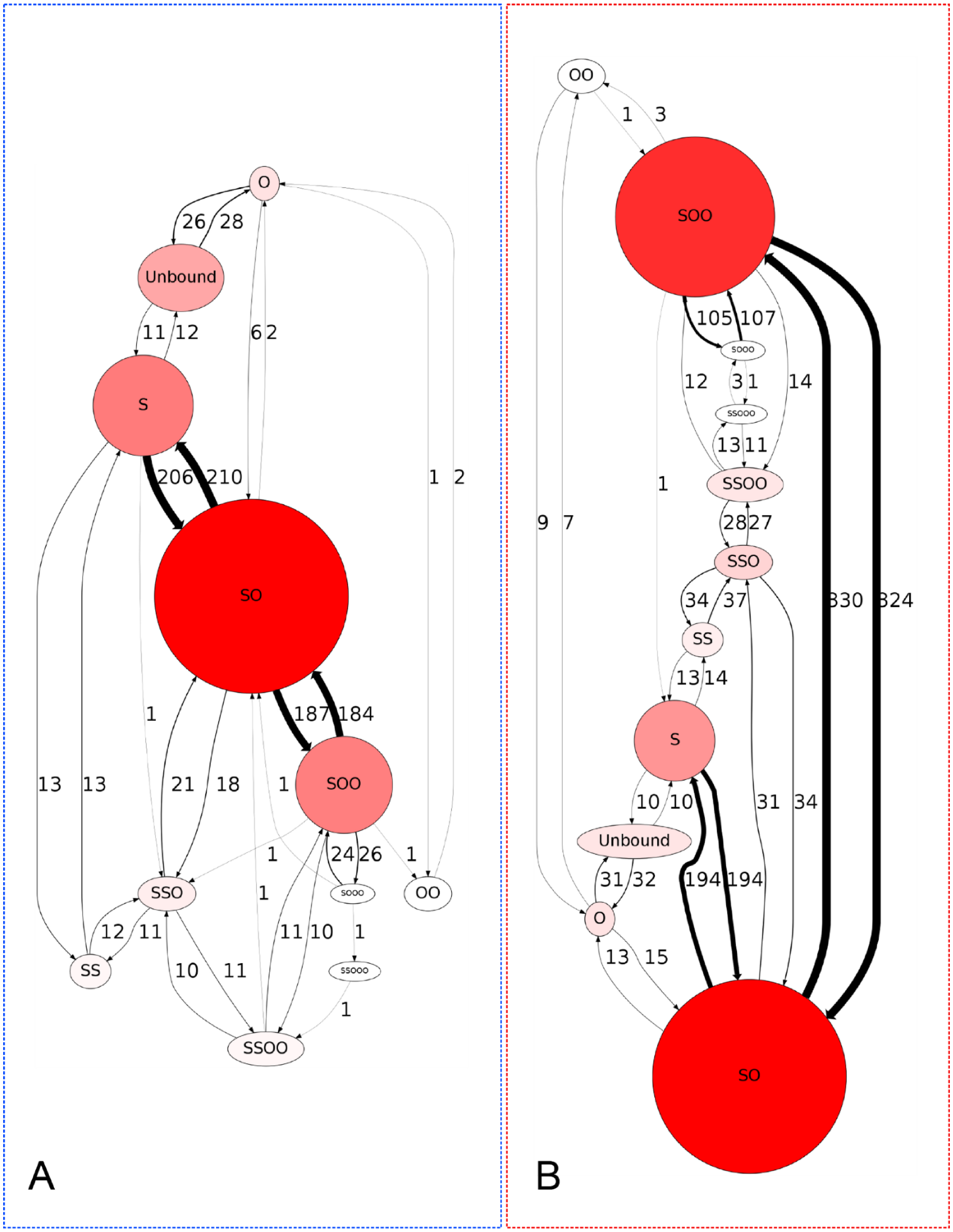

FIGURE 5.6. A graph of the $SO_2$ bonding coordinations showing (directed edges) the number of times the coordination transition occurred.

Given the information about the frequencies of bonding coordination transitions, it is possible to draw a likely route of adsorption beginning with an unbound $SO_2$. From the unbound coordination, the $SO_2$ can bind to waters either through the sulfur or an oxygen to enter the “S” or “O” coordinations, respectively. At both temperatures the coordination transition in Figure 5.6. from unbound to “O” occurs almost three times more than the transition from unbound to “S”. Two possibilities may explain this difference. The single H-bonding of the “O” coordination may form more easily, but also break quickly after formation, accounting for the higher transition frequency. Otherwise, the “O” coordination may be the first step in adsorption of an unbound $SO_2$, where a subsequent addition of an $SO_2$-sulfur interaction to a water oxygen would lead to a transition to the most frequent coordination, “SO”. In the latter case, any adsorption of $SO_2$ proceeds through an oxygen binding, accounting for the increased unbound-“O” transition frequency.

To verify if the “O” coordination forms from, and breaks quickly to the unbound coordination as is suggested by the transition frequency plots in Figure 5.6., the lifespans of the various coordinations are plotted in Figure 5.7. Each point in the plot represents a time during the simulation in which the $SO_2$ formed the respective coordination. The vertical “lifespan” position is calculated directly from the amount of time spent in the given coordination before changing to another. Both cold (blue) and hot (red) data are plotted. The data of Figure 5.7. show that most coordination configurations last a very brief time, with the majority forming for under 0.5 ps. The three most populous coordinations, “S”, “SO”, “SOO” (as determined from Figure 5.4. by percentage) in both temperatures have coordination lifetimes of up to 1 ps, in some instances lasting up to 1.5 ps. The brevity of lifespans overall speaks to the dynamic nature of the $SO_2$ surface binding. The length of time in each coordination parallels the populations of the coordinations, and suggests an ordering of steady states among various bonding coordinations. The “unbound” configuration stands out as an anomaly amongst the lifespans of the other bonding coordinations. The few lifespans above 1.5 ps, up to 3.25 ps long, suggest a $SO_2$ that not only unbinds from the water surface, but that it also recedes far enough to avoid a quick rebinding and coordination change to “S” or “O”. Those data points of a few long lived unbound species indicate times when the $SO_2$ is far from the water, residing in the gas phase until the necessary water rearrangement occurs and it is drawn back to the surface to rebind.

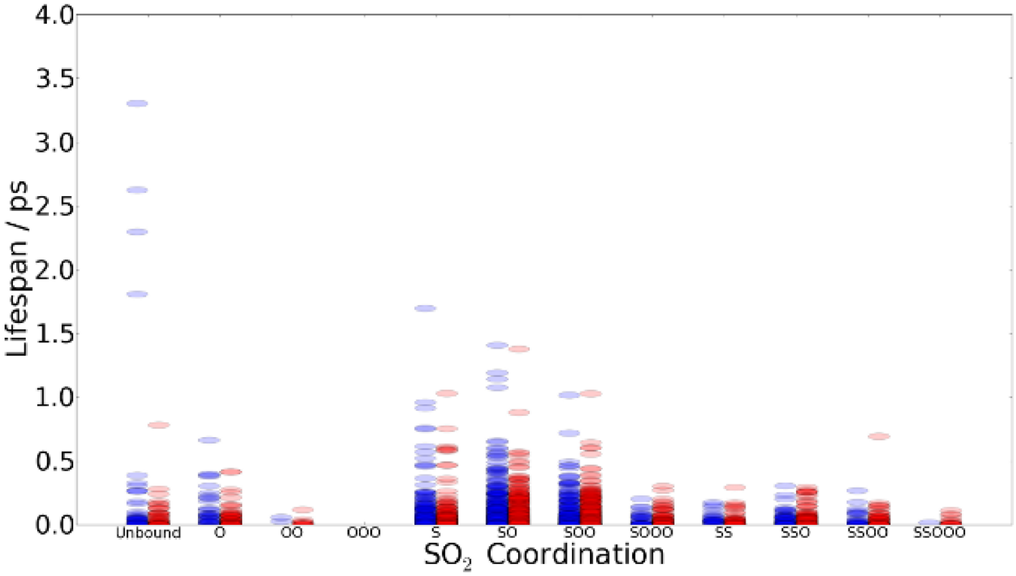

FIGURE 5.7. Time $SO_2$ spent in each bonding coordination. The total amount of consecutive timesteps in a coordination corresponds to the vertical position along the lifespan axis, in ps.

Returning to the transition plots of Figure 5.6., the behavior of the unbound transition to both “S” and “O” coordination can now be better characterized. Figure 5.7. shows that the “O” coordinated lifetimes are shorter than the “S” coordinated ones. Figure 5.6. shows that the unbound-“O” transition occurs almost three times more than the transition to the “S” bonding coordination. The unbound $SO_2$ forms a bond to a neighboring water through its oxygen, but that bond is short-lived and either quickly breaks (resulting in unbound $SO_2$), or it transitions to the “SO” coordination by forming another bond through the sulfur. The unbound-“S” transition does not occur as often. This may be because the “S” coordination is more stable than the “O”. Once in the “S” coordination the $SO_2$ does not quickly break the interaction from its sulfur to water, but rather remains for up to 1 ps in the “S” coordination before (most likely) forming an oxygen bond to make the “SO” coordination. The likely behavior of $SO_2$ is described as it transitions from the gas phase in an unbound coordination to binding with waters on an aqueous interface.

Once the $SO_2$ begins interacting with the water surface, the pathway leading back to the unbound coordination is not often traversed. As shown in Figure 5.6. the dominant coordination transitions occur between the “S-SO-SOO” group of coordinations. This suggests that the $SO_2$-sulfur interaction to a water oxygen has a much longer lifespan than the $SO_2$-oxygen bonding to water hydrogens. The difference between the “S-SO-SOO” coordinations is an addition or removal of oxygen bonds. The frequent transitions between them show that the bonds to $SO_2$-oxygens are quickly forming and breaking. For the $SO_2$-sulfur interaction to break, the $SO_2$ must enter a non-sulfur coordination (e.g. “O”, “OO”, unbound, etc.) or a coordination with more than a single sulfur interaction (e.g. “SS”, “SSO”, etc.). The transitions to coordinations that allow for breaking of the $SO_2$-sulfur interactions, or switching the interaction to another water, are infrequent compared to those leading to an oxygen bond transition. Thus, the $SO_2$ spends most of its time while bound to the surface waters breaking and forming hydrogen-bonds through its oxygens, and interacting with neighboring waters through a more persistent interaction via the $SO_2$-sulfur atom.

## 5.4. Cyclic $SO_2$ Hydrate Structures

Having examined the bonding coordinations and bonding behavior of $SO_2$ with surface waters, attention is now turned to a secondary behavior of the hydrate structures that form around the surface-bound $SO_2$ molecule. The simulation trajectory data was analyzed to determine the presence and characteristics of $SO_2$ cyclic hydrate structures that form, as posited earlier in the text and depicted in Figure 5.2. Only the most commonly occurring subset of the cyclic structures were analyzed based on two selection criteria: (1) The distances between atoms must match the same bonding/distance criteria as used for determining bonding coordinations. (2) The $SO_2$ must be minimally in a bonding coordination of type "SO", meaning that the sulfur has at least one bonding interaction, and at least one hydrogen-bond must have formed with an oxygen to a neighboring water-hydrogen. As noted earlier in the discussion of the graph BFS algorithm, the cyclic structures found represent the smallest cycles in which the $SO_2$ is a member, based on the search's order of cycle discovery. The $SO_2$ will be involved in other larger and more extended cyclic bonding structures beyond the first one discovered via the BFS. The larger and more extended cyclic structures involving more waters affect the behavior of the hydrogen-bonding network of the water surface. The focus here is only on the smallest cycles involving the $SO_2$ as they most affect the $SO_2$ bonding and hydration.

The plot in Figure 5.8. shows the distribution of how often the various types of cyclic hydrates were encountered at both cold (blue) and hot (red) temperatures. Each data point shows a percentage of the MD trajectories in which the $SO_2$ was a member of a cyclic structure, for different numbers of cyclic waters (up to 4). The two tallest data points, left-most in the plot, show the overall time spent in all types of cyclic structures. Clearly the hot $SO_2$ spends more time in a cyclic structure than at the cold temperature. It is remarkable that the time spent in a cyclic structure shows a 15% difference (42% cold, 57% hot). The hot $SO_2$ spends well over half of the simulated time bound as one of the hydrate cycles, and the cold $SO_2$ spends just under half of the time as such. Thus, in addition to having earlier found the most likely bonding coordination during the simulated life of $SO_2$, the hydrates of the $SO_2$ form cyclic structures for much of the time while bound to the water surface.

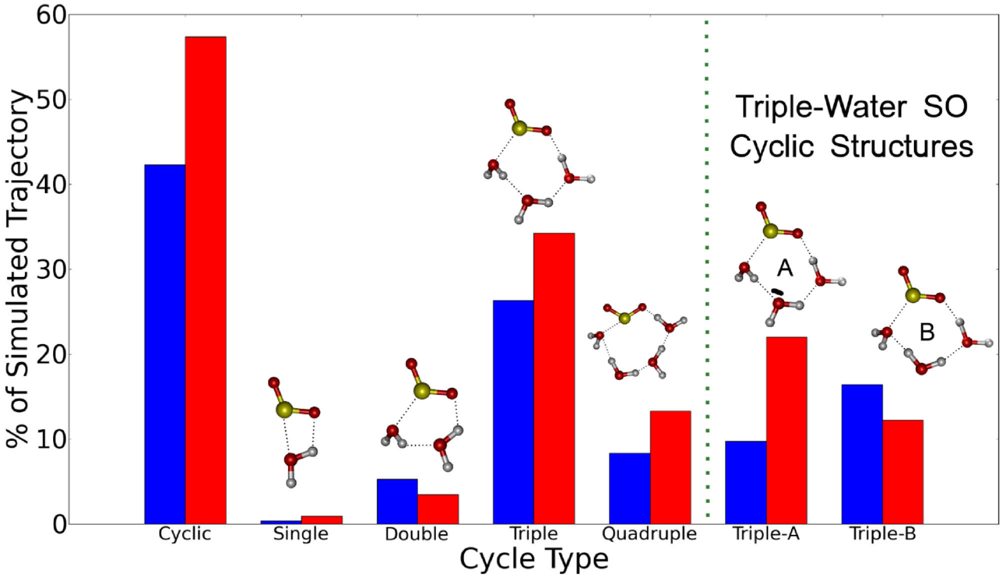

FIGURE 5.8. Different $SO_2$ cyclic hydrate structures (up to 4 waters), and occurrence rates as a percentage of total simulation time.

Now begins a look at the different types of cyclic hydrates, distinguished by the number of waters involved in the bonding structure. In Figure 5.8. the single and double water cycles are the least frequently encountered structures, accounting for less than 10% of both cold and hot temperature simulation times. Formation of the single-water type is likely energetically unfavorable because of the proximity of the water to the $SO_2$ required to form the bonding cycle. The double-water structure was one of two types of clusters proposed in a previous computational work as a candidate structure contributing to the overall IR spectrum of surface-bound $SO_2$.[107] In those static and geometry-optimized cluster calculations, lacking the extended water structure or bonding from waters external to the hydrate, both the double and triple types appear equally likely to form. However, the MD simulations here have introduced many waters into a dynamic environment allowing for extended bonding networks, and the results show clearly that the double-water cyclic hydrate is formed much less often (less than 5% at both temperatures) than the triple-water form.

The results for triple and quadruple-water structures show that larger hydrate cycles are favored at higher temperatures. Although the higher number of hydrating waters ($> 4$) are not shown, those contribute minimally to the overall distribution. The majority of the cyclic hydrates are formed with three waters in the triple-water type. This hydrate type matches the bonding structure inferred from previous experiments, and also one of the cluster types modeled by others.[16, 17, 107] It was further found that, of the triple-type hydrate cycles, the waters contributing to the cycles can be arranged in two ways that preserve the hydrogen-bonding between the molecules (described earlier and shown in Figure 5.3.). The triple-water type cycle results were broken-down into contributions from the type-A and type-B triple-water structures. The two triple cycle structures are depicted on the right side of Figure 5.8., along with the plots of their contributions to the overall distribution. It is notable that each temperature has a different dominant type of triple-water cyclic structure.

The cold system forms more of the type-B, and the hotter system forms primarily type-A.

### 5.4.1. Cyclic Hydrate Structure Lifetimes

We know that the $SO_2$ bound to a water surface is most likely in the "SO" bonding coordination, and is also often taking part in some type of cyclic structure. With this in mind, it becomes interesting to ask: how long does a cyclic hydrate form before breaking to an acyclic hydrate structure? To answer the question of cyclic lifespan, a method was devised to define the lifetime of a cycle. For each MD trajectory, coordinate data was analyzed to determine if a cyclic hydrate structure was formed as described earlier in this manuscript. A timeline was then produced where each timestep was given a value of 1 or 0 depending on whether a $SO_2$ hydrate bonding cycle was present or not, respectively. This resulted in a time-function, $C(t)$, similar in nature to a time-varying digital signal.

In an electro-mechanical system, a mechanical switch often outputs a noisy signal, full of transients or "signal bounce" before settling to a final value. This will appear as a rapid on-off cycling of the signal, and the problem is one of great concern in signal processing. Many mechanical, electrical, and software solutions have been devised to suppress the transients, or "debounce" the signal. Analogously, the hydrate bonding cycles formed in the simulated system often undergo a period of time during formation, or before dissolution, where the $C(t)$ function bounces before settling into a final value. The bounce in the function manifests itself in the statistics as a series of rapid switches between cycle presence and cycle absence. Physically, the bond lengths within the cycle (or the cycle-to-be) are fluctuating back and forth across the bond-length criteria. It is thus an artifact of algorithmic determination of the presence or absence of a bond. Removing this artifact will allow us to examine the longer-time bonding behavior and this is accomplished as follows.

We wish to find a function based on $C(t)$ that eliminates the brief oscillations during transitions. The resulting function, $f(t)$, will only contain information of whether a hydrate bonding cycle is present or absent, and none of the noisy oscillations of the transitions between the two states. $f(t)$ may then be used to calculate statistics about the cycle lifespans. A representative portion of a cycle time-function, $C(t)$, is plotted for one of the simulated trajectories shown as the dashed black line in Figure 5.9. At the far left of the plot the function is in the "no cycle" state indicating that a bonding cycle has not been detected, and then switches "on" as a cycle is found later in time. The cyclic structure is very dynamic, constantly moving and distorting, so any of the bonds forming the cyclic bonding structure are liable to break and reform quickly. This bouncing between states is manifested in Figure 5.9. as a series of sharp spikes in the $C(t)$ function lasting less than 10 fs each. $C(t)$ was smoothed using a moving Gaussian window function with a 10 fs width, having the effect of disregarding cycle breaks or formations of less than 20 fs duration. The resulting smoothed function, $C_s(t)$, was then cutoff with the following criteria:

$$f(t) = \begin{cases} 0 & C_s(t) < 0.2 \\ 1 & C_s(t) \geq 0.2 \end{cases}$$

where $f(t)$ is the debounced time-function that represents the lifespans of cycles. Figure 5.9. shows the original time-function of cycle formation and breaking, $C(t)$ (dashed black), the smoothed function, $C_s(t)$ (red), and the final debounced function, $f(t)$ (green).

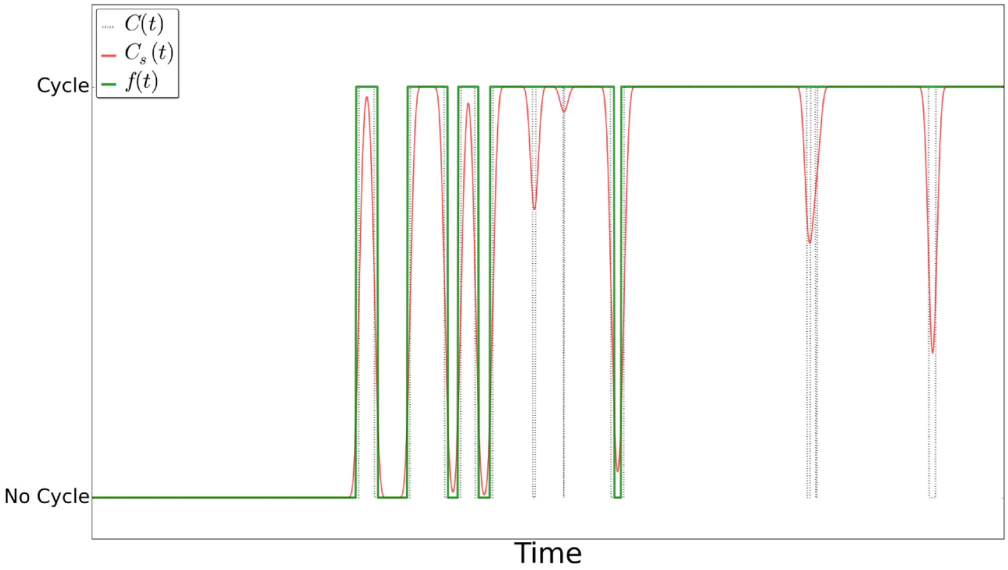

FIGURE 5.9. (dashed black) A cyclic $SO_2$ hydrate formation time function, $C(t)$, (red) a smoothed $C_s(t)$, (green) the debounced cycle formation function, $f(t)$.

The distribution of cycle lifetimes (i.e. contiguous spans of time spent with $f(t) = 1$) was determined. The distribution of cyclic lifespans is shown in Figure 5.10. for the cold (blue) and hot (red) simulations. The most frequent lifespan for both temperature data sets lasts between 0-1 ps. This accounts for the vast majority of cyclic hydrates found (approximately 95%) indicating that these structures are very transient, and are continuously forming and breaking for very short periods of time. Even with the debouncing procedure that would artificially increase the timespan spent either formed or broken, the nature of the water surface, and the very dynamic extended hydrogen bonding network, keeps many of the structures from lasting much longer than 1 ps. The difference between hot and cold systems in the $< 1$ ps population is less than 2%, with this trend extending to the longer lifespans as well. The inset of Figure 5.10. shows an expanded view of the region above 1 ps. All of the distribution shows only a $< 1.5\%$ difference between cold and hot cyclic lifetimes.

Overall, the distribution shows that when cycles form, at both temperatures, they last a similar amount of time. Up to 3 ps, the cold temperature cycles show a very slight population increase above the hot temperature cycles. Above 4 ps, most of the cycles that form are found in the hot system. The 8 ps cycles are notable in that they form for just under half the length of one of the simulated trajectories.

We know from the transition frequency plots of Figure 5.6. that the bonding coordinations are switching frequently. The $SO_2$ is likely forming and breaking bonds with waters external to the cyclic hydrate structures (i.e. not directly involved in the bonds of the cycle). For the longer-lived cycles, the external bonding to the $SO_2$ may have little effect on the cyclic hydrate waters. However, any time the $SO_2$ switches into an unbound, sulfur-only, or oxygen-only coordination (i.e. “S”, “SS”, “O”, etc), the cyclic structure is necessarily broken. Because the majority of cyclic structures last only briefly ($< 1$ ps), the active switching of $SO_2$ bonding coordinations appears to break the cyclic structure. Figure 5.4. shows that the sum of coordinations that necessarily break cyclic structures account for approximately 39% and 24% of the bonding coordinations in the cold and hot system, respectively. Consequently, the distribution of Figure 5.8. also indicates that there are more cycles formed in the hot system (approximately 16% above the cold). Of the three most encountered bonding coordinations, the hot system shifts population from the “S” (a cycle-breaking coordination) to “SO” and “SOO” (coordinations that allow for bonding cycle formation through the $SO_2$). This is relative to the cold system coordination distribution that has equal “S” and “SOO” populations. The increased temperature appears to cause the $SO_2$ to bond in a way that is more conducive to the formation of cyclic structures. This may account for the slightly increased populations of the longer cycle lifespans in the hot system (greater than 4 ps in some cases) compared to the cold system in the cycle lifespan distribution of Figure 5.10.

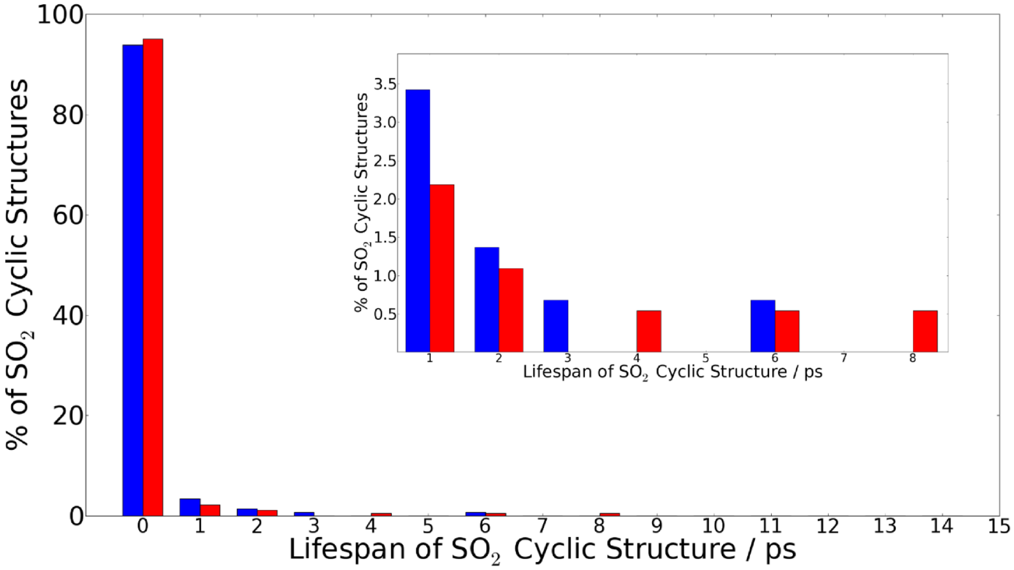

FIGURE 5.10. Cyclic $SO_2$ hydrate structure lifetimes of (blue) cold and (red) hot simulations.

## 5.5. Summary

The adsorption of small gas molecules to water surfaces has been extensively studied over the past few decades. Much has been learned about the energies of hydrate configurations, and the kinetics of gaseous uptake into aqueous systems. Yet, the specific molecular nature of the adsorption process, including the various geometries, hydrate species, and bonding pathways remains largely unknown. As a gas transitions into the liquid water phase, it passes through a fluid interfacial region that remains poorly understood. Our understanding of the processes and chemistry of the interface is still in its infancy, but we are beginning to gain unique new insights that are key to understanding many environmentally important processes at aqueous surfaces.

Presented herein are the results of ab initio molecular dynamics simulations that focus on how a wandering gaseous $SO_2$ molecule first makes contact with a water surface, and subsequently forms extended hydrate structures with interfacial water molecules. The computational studies complement and expand on experimental studies from this laboratory that found surface complexation of $SO_2$ at a water surface.[16–18] Furthermore, these computations build upon and enrich our understanding of adsorbing $SO_2$ behavior from our recently published computational study on interfacial geometries of aqueous surface $SO_2$ molecules.[19]

The simulations show that $SO_2$ has a preferred means of bonding and interacting with surface water molecules by taking on various bonding coordinations. In this study it is shown that the "SO" bonding configuration is the most preferred, with "S" and "SOO" also contributing greatly to the coordination distribution. Once a $SO_2$ has bound to form a surface hydrate it rarely forms multiple bonding interactions through the sulfur atom, and even less frequently takes on a configuration with no sulfur interactions to nearby waters.

This study is one of very few temperature studies looking at the microscopic nature of interfacial gas molecules on water. By changing the temperature, it was found that a hotter water system leads to longer $SO_2$ binding to the water surface. The distribution of bonding coordinations was greatly affected by a temperature change, shifting populations of bonding configurations because of the altered $SO_2$ and $H_2O$ behavior. At the higher temperature, $SO_2$ forms more frequent bonds to interfacial waters through the sulfur and oxygen atoms. Overall, it was determined that the $SO_2$ hydrate interactions are transient, binding and unbinding to water molecules rapidly in very dynamic bonding coordinations.

Introduce here is the use of a graph structure to represent atoms and interconnectedness between molecules, and also to represent transitions between the various bonding coordinations of an adsorbed $SO_2$. It was shown that the intermolecular bonds formed through the $SO_2$-oxygens are quickly broken and formed, lasting briefly compared to sulfur interactions. From the graph of bonding coordination transitions, a likely pathway for $SO_2$adsorption was found starting with an unbound gas-phase $SO_2$, ending with a hydrated $SO_2$ species bound to surface waters.

The formation of cyclic hydrate structures was probed and it was found that these hydrated bonding ring species form during much of a simulated trajectory. Temperature increases the occurrence of cyclic structures, and also shifts the distribution of the specific types of cycles being formed. Two types of cyclic tri-hydrates were discovered during the course of simulations. The cycle lifetimes were found to be mostly short-lived, with a majority lasting less than 1 ps before breaking and reforming due to the dynamic bonding and motion of the surface waters and $SO_2$ molecules. Temperature did not have a very dramatic effect on the cyclic lifespans, but higher temperatures did lead to $SO_2$ bonding coordinations that are more likely to form into cyclic hydrates.

These studies build upon computational and experimental research in this area, seeking to understand how gases adsorb and transit across an aqueous/air interface. Such knowledge is invaluable for understanding land water and environmental aerosol systems where gaseous uptake behavior at a water surface surprises us and often defies physical intuitions.[99, 101, 106, 118]

The following two chapters of this dissertation document two projects involving interfacial aqueous malonic acid. The first of the two projects in Chapter VI was a collaborative effort involving both SFG experiments and classical computational simulations of malonic acid solution surfaces. Chapter VII documents a follow-up DFT-MD computational project that further probes the surface nature of malonic acid, and compares the more accurate quantum interaction potential with the classical one.

# CHAPTER VI

# DICARBOXYLIC ACID ON A WATER SURFACE

This work was co-authored, and the manuscript is in preparation to be submitted for review. Eric S. Shamay provided all the computational simulation results and analyses. Patrick Blower conducted the VSFS experiments of malonic acid probing the carbonyl C=O vibrational modes. Stephanie Ota performed the VSF experiments and analysis of the methylene CH vibrational modes. Patrick Blower was the principle investigator for this work.

## 6.1. Introduction

Organic materials are ubiquitous in the atmosphere of our earth[142] and their presence in aerosols affect important changes in climate conditions.[143, 144] Climate forcing is caused by aerosols directly through scatter and absorption of radiation, and indirectly through cloud formation. It has been shown that up to 90% of the total mass of tropospheric aerosols (dependent upon location) can be comprised of contributions from organic matter[142] and this has spurred a revival in the study of how organic materials affect aerosol properties. Organic acids are a particularly important class of organic material involved in aerosols, varying in size and complexity from low molecular weight formic acid[145] to large humic-like substances (HULIS).[146] Dicarboxylic acids represent a sizable fraction of organic material; they are of low molecular weight and soluble in water, and also contain multiple acidic sites. Dicarboxylic acids are a prevalent hygroscopic[147] and water soluble component of our atmosphere that occur in urban, rural, remote, and marine environments.[145, 148–155] In fact they are often the dominant class of water-soluble organics in our environment, with the shorter C2-C4 found to be the most abundant.

Since organic aerosols can be hygroscopic and are capable of acting as cloud condensation nuclei[156] (CCN), much effort has been put into understanding the properties of these aerosols as well as secondary organic aerosols (SOA). Prediction of CCN activation is well understood for inorganic fractions (e.g. NaCl, $(NH_4)_2SO_4$)[143] and can be determined based on chemical composition, solubility, surface tension, and dry particle size (i.e. Kohler curves). Atmospheric aerosols contain a mixed chemical composition including a significant fraction of organic components; it is often necessary to determine these properties for organic components. Deliquescence,[157] phase transitions,[158] water activities,[159] and surface tension[160–162] have been investigated for binary systems containing malonic acid as well as other atmospherically relevant dicarboxylic acids in order to aid in the predictability and modeling of these binary systems as CCN.[163] While these studies have provided a better understanding of the bulk thermodynamic properties of dicarboxylic containing aerosols as a stable/unstable particle for CCN, they do not address the heterogeneous reactions[164] that can take place at the surfaces of these aerosols. For example, a recent study on halogen activation on water surfaces (i.e. a heterogeneous reaction) shows how weak acids at a water surface, such as malonic acid, can actually enhance $I_2$(g) production in the marine boundary layer when compared to a neat water surface.[165]

It is known from surface tension measurements[160–162] that short-chain dicarboxylic acids are surface active. However, unlike traditional ionic alkyl surfactant molecules that have well defined hydrophobic and hydrophilic parts, low molecular weight dicarboxylic acids have two hydrophilic ends (carboxylic acid moieties) connected by a hydrophobic spacer $(CH_2)_n$. As a consequence, unlike simple alkyl carboxylic acid surfactants, one cannot *a priori* predict the orientation and surface-bonding characteristics of the dicarboxylic acids. Given the prevalence of dicarboxylic acids in aerosols, surprisingly few molecular-level investigations of the behavior of dicarboxylic acids at aqueous surfaces have been conducted.

One of the more important dicarboxylic acids in the atmosphere is malonic acid, the focus of this chapter. Malonic acid, with its two carboxylic acid groups separated by a $CH_2$ spacer is found in significant concentrations in aqueous environments (aerosols, cloud water, freshwater, seawater and various forms of wet deposition). A combination of experimental and computational methods are employed to develop a robust molecular picture of the behavior of malonic acid at a water surface. The experimental approach involves surface tension measurements to provide quantitative thermodynamic data on the adsorption process and vibrational sum frequency spectroscopy (VSFS) as a means for obtaining a more microscopic picture. VSFS is a surface specific spectroscopy that is excellently suited for exploring the surface properties of these aqueous organic systems. As a second order non-linear vibrational spectroscopy method, VSFS is highly surface specific and can impart valuable information about the structure and orientation of an adsorbate as well as the alteration of surface water molecules due to the presence of the adsorbate. Molecular dynamics are used to create a more complete picture of adsorbate behavior, and complement well the experimental methods. MD probes directly the specific orientations and geometries of malonic acid on a water surface, and also the intermolecular interactions taking place with neighboring waters. Orientational analyses of MD trajectories show the geometry of malonic acid throughout a water interface, and the response of the acid orientation to location within the surface.

In addition, the use of computer modeling greatly assists in the interpretation of VSFS spectra and provides detailed molecular data that is otherwise inaccessible by experiment.

This chapter explores surface speciation, orientation, and surface pH dependence of malonic acid by using this combination of experimental and theoretical approaches. Results presented here provide the platform necessary to interpret the more complicated ternary systems that more closely resemble the aerosol compositions of the atmosphere. This is a work of fundamental importance for establishing malonic acid behavior for further study of this system, and also of more complex acids and solutions.

## 6.2. Experimental Methods

### 6.2.1. Surface Spectroscopy

VSFS is an excellent tool for exploring aqueous interfaces because of its surface specificity; it is forbidden in centrosymmetric media such as bulk water. VSFS has grown in the past decade as a highly versatile method for studying a variety of processes at water surfaces. A brief description is given below as it pertains to the experiments conducted in this study. Two different laser systems were used. The VSF experiments conducted in these studies involve an 800 nm beam of light overlapped in time and space with a variable frequency beam (in the IR) at the surface of the aqueous solution. The intensity of the resulting sum frequency signal is proportional to the square of the second-order susceptibility, $\chi^{(2)}$, which has both a resonant and non-resonant component, as shown in Equation 6.1.

$$\chi^{(2)} = \chi_{NR}^{(2)} + \sum_{\nu} \chi_{R,\nu}^{(2)} \qquad \text{(Equation 6.1.)}$$

The resonant susceptibility, $\chi_R^{(2)}$, is proportional to the number of molecules contributing to the sum frequency response, N, and the orientationally averaged molecular susceptibility, $\langle\beta\rangle$, as in Equation 6.2.

$$\chi_R^{(2)} = \frac{N}{\epsilon_0}\langle\beta\rangle \qquad \text{(Equation 6.2.)}$$

Because of the overlap of some modes with other resonant modes, as well as the non-resonant background, spectral fitting is necessary to deconvolve individual peaks. A fitting procedure[166] is employed that accounts for homogeneous and inhomogeneous line-widths of VSFS active modes (Equation 6.3.).

$$\chi^{(2)} = \chi_{NR}^{(2)} \exp^{i\phi} + \sum_{\nu} \int_{-\infty}^{\infty} \frac{A_\nu \exp^{i\phi_\nu} \exp^{-[\omega_L - \omega_\nu/\Gamma_\nu]^2}}{\omega_L - \omega_{IR} + i\Gamma_L} \qquad \text{(Equation 6.3.)}$$

The first term in Equation 6.3. is the non-resonant susceptibility (containing an amplitude and phase). The second term is the sum over all VSFS active resonant modes. The resonant susceptibility is a convolution of the homogeneous (lorentzian) line widths of the individual molecular transitions ($\Gamma_L$) with inhomogeneous broadening ($\Gamma_\nu$). For a VSFS mode to be active, both a Raman transition and IR dipole change must occur. This is modeled as the transition strength $A_\nu$ and is proportional to the orientationally averaged IR and Raman transition probabilities. The frequencies of the lorentzian, resonant modes, and IR are $\omega_L$, $\omega_\nu$, $\omega_{IR}$, respectively. Each resonant mode also has a phase value, $\phi_\nu$.

The choice of incoming and outgoing polarizations allows for deriving information about molecular orientation. This arises from the fact that of the 27 elements of $\chi^{(2)}$ there are four polarizations that are nonzero and unique ($\chi_{zzz}$, $\chi_{xxz}$, $\chi_{xzx}$, and $\chi_{zxx}$). These unique elements can be probed using incoming polarized visible and IR light, and outgoing polarized sum frequency light. The polarization naming schemes are denoted as “S” (perpendicular to the plane of incidence) or “P” (parallel to the plane of incidence) and are given in the order of sum frequency, visible, IR. By selecting the incoming polarizations to be both S polarized, and the monitored output set to P polarized output, the VSF response allows one to probe dipole components that are perpendicular to the plane of the interface. The SPS polarization combination will probe dipole components that are parallel to the plane of the interface.

Two different laser systems were used in these VSF studies. The first was focused on the mid IR, carboxylic C=O region. This system is an upgraded version that has been described previously.[32, 167] Briefly, a CW Nd:YVO4 laser (Millennia 5sJ, Spectra Physics) is used to pump a Ti:sapphire oscillator (Tsunami, Spectra Physics) which is tuned to produce ˜100 fs pulses centered at 800 nm. These pulses are then amplified using a regenerative amplifier (Spitfire Pro XP, Spectra Physics) to produce nominally 3 W of 800 nm light with a bandwidth of ˜12 nm. These pulses are split with ˜1 W going to a home-built slicer that spectrally narrows the pulse to ˜2 ps and ˜1 W going to an optical parametric amplifier (OPA-800C, Spectra Physics) for DFG mixing and subsequent IR generation. Both the IR and visible pulses are then propagated to the interface, where they are overlapped in time and space to produce sum frequency pulses. The resulting sum frequency pulses are filtered by an edge filter (RazorEdge, SEMROCK), collected by a lens, and focused into a spectrograph (SpectraPro 150, Acton Research) which disperses the signal onto a liquid nitrogen cooled CCD (Princeton Instruments). All spectra are normalized to the non-resonant response off of a bare gold surface (three 30 s scans and one 30 s background scan) and are calibrated using a polystyrene standard and absorption lines from ambient water vapor. All measurements were performed at 20 °C.

The second system used was calibrated for the water/CH region, and has been documented in previous publications from this laboratory.[18] This picosecond system generates sum frequency light by overlapping 800 nm (˜2.6 ps, 1 kHz repetition rate) and tunable (2700-4000 $cm^{-1}$) infrared light in a copropagating geometry at 56° and 67° from the surface normal, respectively. After filtering any reflected 800 nm light, the resultant sum frequency light is collected with a thermoelectrically cooled CCD camera (Princeton Instruments) in 3 $cm^{-1}$ increments over the tunable range.

### 6.2.2. Surface Tension

The Wilhelmy plate method was used for collecting Surface tension measurements of the aqueous solutions via a force balance (KSV Instruments).[168] The solutions were placed in a clean glass dish and careful manipulation ensured that the plate was oriented correctly to the interface. Samples were allowed to equilibrate before the measurements were taken. The Pt plate was flamed until glowing orange and rinsed repeatedly in >18 MΩ water between measurements.

### 6.2.3. Chemicals

Malonic acid was purchased from Sigma-Aldrich (ReagentPlus 99%). NaOH was purchased from Mallinckrodt Chemicals (AR). All solutions were prepared fresh with >18 MΩ water and used within 72 hours. All glassware was cleaned with concentrated $H_2SO_4$ and NOCHROMIX and was thoroughly rinsed with >18 MΩ water.

## 6.3. Computational Methods

Classical molecular dynamics (MD) simulations were performed using the Amber 11 suite of simulation programs.[11, 169] A single system of water and malonic acid was initialized for simulation by creating a cubic unit cell with side lengths of 30 Å. The unit cell was then randomly packed with 900 water molecules, and 40 malonic acid molecules using the PACKMOL program created to simplify construction of MD starting configurations.[170] This resulted in a malonic acid concentration of 2.5 M, purposefully set to be similar to that of the VSFS experimental conditions.

The initial system was energy minimized by a combination of steepest descent and conjugate gradient methods to reach a geometry optimization. The z-axis of the system was then expanded to 100 Å creating a large vacuum region adjacent to the aqueous cube. Periodic boundary conditions were then employed resulting in an infinite slab configuration with two aqueous-vacuum interfaces. This configuration was then evolved through MD simulation for 500 ps to equilibrate the system. The system was then evolved for 50 ns of data-collection, recording atomic coordinates every 100 fs for a total of 500,000 data points.

The simulations were performed using a timestep of 1 fs. Fully polarizable models were used for both the water and malonic acid molecules. Water was simulated using the POL3 model,[73] and the malonic acids were constructed using a fully atomistic model based on the Amber FF02EP force field.[10] The system temperature was set at 298K, and Langevin dynamics were used to propagate dynamics via a leapfrog integrator. The particle mesh ewald technique was used for calculating long-range electrostatic interactions, with a force cutoff set to 10 Å. Waters were held rigid by means of the SHAKE algorithm to increase computational throughput and speed of data collection.

In all following analyses, the results obtained for molecular orientation are averaged between both of the water slab surfaces. The distance to each aqueous surface was determined for every malonic acid at each timestep using the method developed in our recent computational study to determine water surface locations.[19] The closer surface was always used to analyze acid orientation, and the reference axis was always set to point from the aqueous bulk outwards towards the vacuum phase, normal to the plane of the water surface.

## 6.4. Spectroscopic Response of Carboxylic Acid

Spectroscopically probing the adsorption of malonic acid at the water surface involved two different spectral regions: the first corresponds to the carboxylic C=O modes in the 1600-1800 $cm^{-1}$ region, and the second captures the C-H stretch modes of the malonic acid and the OH stretch modes of surface water molecules in the 3000 $cm^{-1}$ region. Both SSP and SPS polarization combinations were used in both spectral regions to measure the modes that have dipole moments perpendicular and parallel to the interface respectively.

Figure 6.1. shows the SSP spectra of aqueous MA at four concentrations. The intensity of the signal from the carboxylic C=O modes in the SSP polarization scheme increases as the bulk concentration of MA increases. The intensity increases progressively from the lowest concentration at 100 mM to the highest concentration at 3 M. In VSFS studies, intensity derives from both number density at the surface and net surface orientation of the molecules probed; the direction is dependent on the polarization combinations used. Malonic acid clearly is present at the water surface with increasing population as the bulk solution concentration increases. The strong signal observed under SSP polarization further indicates that the dipole moment of

one or both MA carboxylic acid groups has a net orientation perpendicular to the surface plane. According to the global fits of the spectra, one peak is centrally located at 1740 $cm^{-1}$ with a Gaussian width of 23 $cm^{-1}$. No shift in the VSF signal frequency is observed as bulk solution concentration increases.

Infrared studies of MA in bulk aqueous solution have shown that the carboxylic C=O modes appear at 1719 $cm^{-1}$ for the fully protonated ($H_2A$) form, and 1713 $cm^{-1}$ for the singly protonated ($HA^-$) form.[171] In addition, this mode is also sensitive to the degree of water solvation, with monomers in the vapor phase having been measured as high as 1760 $cm^{-1}$.[172] The intermediate frequency of 1740 $cm^{-1}$ observed for MA at the water surface is a reflection of carboxylic C=O modes that are weakly solvated by water molecules at the interface; they are more weakly solvated than previous studies of the carboxylic acid group of hexanoic acid at the vapor/water interface.[32] It should be noted that these are relatively weak signals. Consequently, the normally negligible non-resonant background interferes with the signal on the high-frequency side of the spectra resulting in a non-zero VSFS signal. This interference has been seen before in VSFS studies of carboxylic C=O modes at aqueous interfaces[173] as well as nitrate modes.[167] In addition to the frequency assignments, the phase values obtained in the spectral fitting routines indicate that the carboxylic C=O dipoles have an overall orientation pointing away from the bulk water toward the gas phase.

The carboxylic C=O modes were also probed in the SPS polarization resulting in less intense signals than SSP. Figure 6.2. shows the results. Since the SPS scheme excites modes that are in the plane of the interface, the signal intensity can be decreased due to canceling of the VSFS signal from the rotational degeneracy that occurs in the polarization. Similar to the SSP experiments, the SPS signal intensity

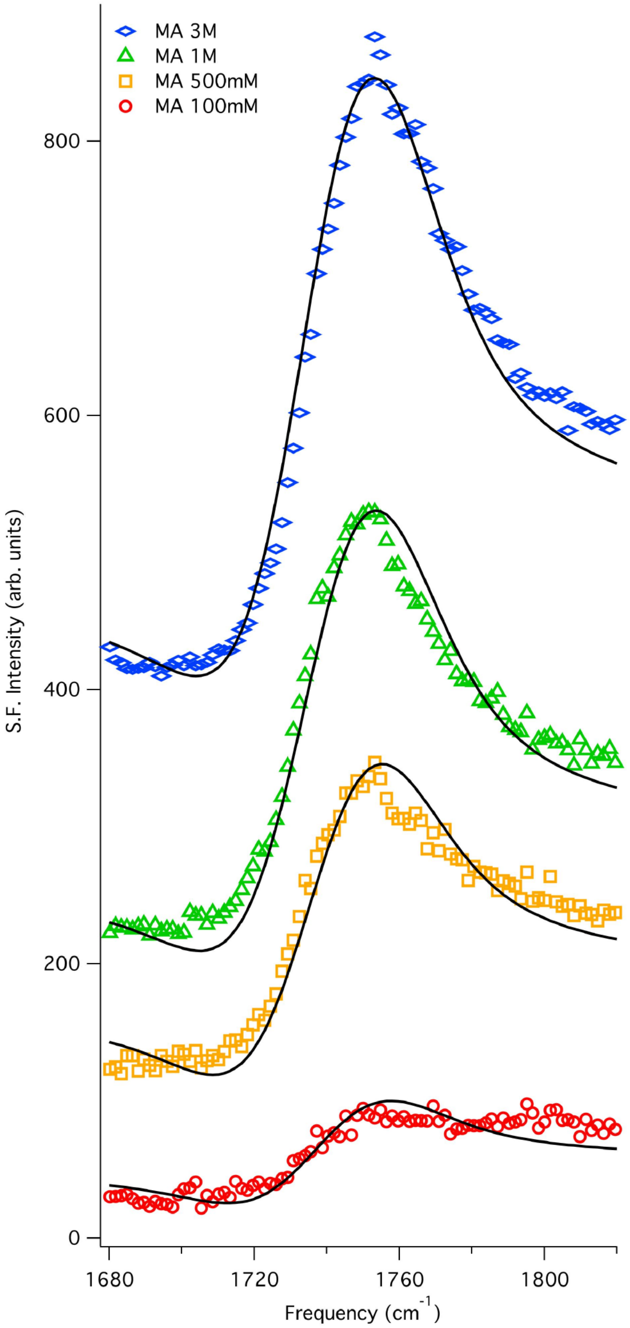

FIGURE 6.1. VSFS-SSP spectra of the carboxylic C=O of aqueous malonic acid at concentrations of 0.1 M, 0.5 M, 1 M, and 3 M.

increases as the bulk concentration of MA increases. However, the fitted spectra reveal a peak centrally located at 1730 $cm^{-1}$ (versus 1740 $cm^{-1}$ SSP) with a slightly larger

Gaussian width of 30 $cm^{-1}$ (versus 23 $cm^{-1}$ SSP). Although this C=O frequency is higher than bulk values, it is not shifted as much as that arising from the SSP spectra, and is closer to bulk aqueous values. The larger Gaussian width is consistent with a more heterogeneous environment, further supporting the assertion that the SPS-active carboxylic C=O modes are in a slightly different environment than their SSP-active counterparts.

### 6.4.1. CH and OH Spectral Response

In addition to probing the carboxylic C=O modes of MA, the spectral region associated with the methylene CH modes of MA (˜2900 $cm^{-1}$) was investigated to develop a more comprehensive picture of the adsorbate structure. The OH stretch modes of water were also investigated as a means of determining how the adsorbate presence alters the surface water structure and bonding in three spectral regions. A simple picture that has evolved from many VSF studies of OH oscillator behavior: the free OH region (˜3700 $cm^{-1}$) corresponds to the response of water OH oscillators that have minimal interaction with nearby water molecules and in fact are vibrationally decoupled from the hydrogen-bonding network of bulk water; these modes are most affected by adsorbates at the top most layer of the interface. OH oscillators corresponding to the most highly coordinated surface water molecules reside at much lower frequencies (˜3200 $cm^{-1}$); these are also water molecules deeper in the interfacial region and more sensitive to the presence of interfacial ions. The region corresponding to intermediate degrees of hydrogen bonding and interfacial depth is seen near 3400 $cm^{-1}$.

Figure 6.3. shows six spectra of the water/CH region for three different concentrations of MA. Looking first at the CH stretch region, as the MA solution

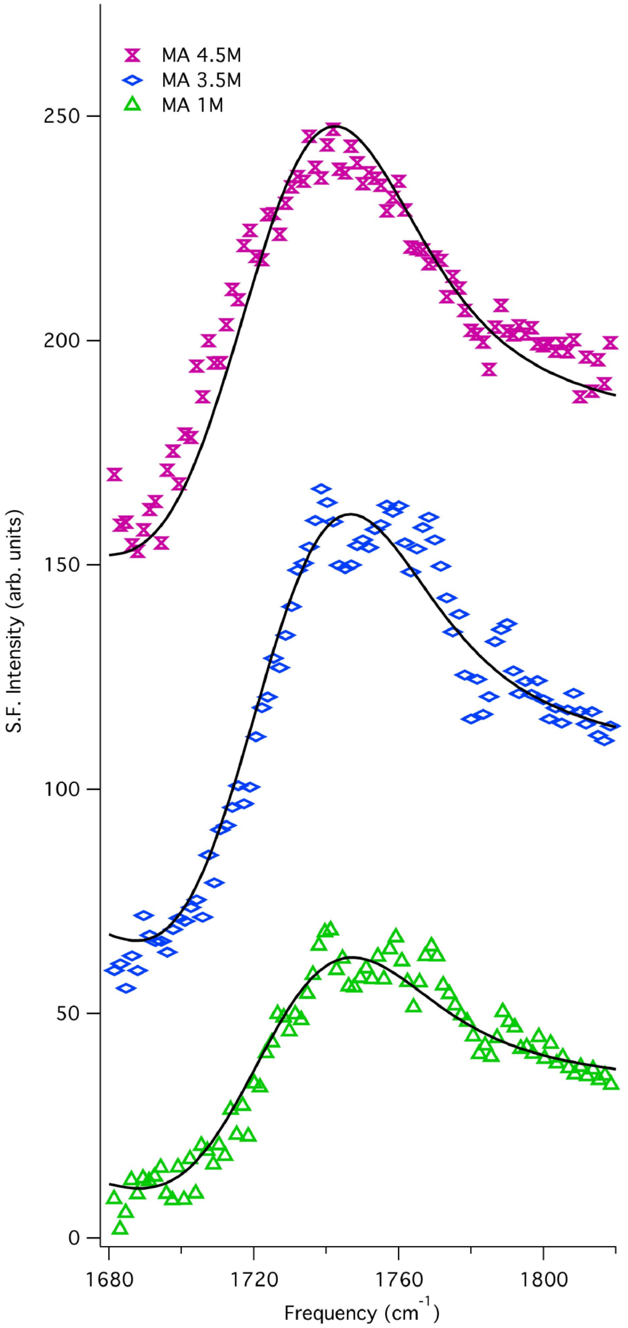

FIGURE 6.2. VSFS-SPS spectra of carboxylic C=O of aqueous malonic acid at 1 M, 3.5 M, and 4.5 M.

concentration increases, there is a corresponding increase in intensity from 2800-3000 $cm^{-1}$. Unfortunately, the overlap between the OH modes and the CH modes makes distinct spectral characterization difficult. Nevertheless, this broad region between 2800 and 3000 $cm^{-1}$ is attributed to the carboxylic OH stretching of malonic acid based on isotopic VSFS studies done on selectively deuterated succinic acid, $(COOH)_2(CD_2)_2$, in $D_2O$ and $H_2O$.[18] The overall trend observed is that with increasing MA concentration, there is a corresponding increase in signal in the CH region. However, there is no evidence of a high degree of orientation of any CH modes at the surface, even at the high concentration as can be seen from previous surfactant studies. The absence of any observation of $CH_2$ modes is likely due to an orientational averaging effect. This will be addressed further in the computational section.

Looking next at the water response, upon adsorption, there is a corresponding decrease in the free OH signal with increased MA in bulk solution and consequently at the surface. This decrease is also observed in the 3400 $cm^{-1}$ region corresponding to somewhat stronger but still relatively weakly bonded surface water molecules. Interestingly, the free OH signal does not fully disappear even at concentrations of 3.5 M indicating that the water surface is not completely covered by the MA. This is unlike other similar acid surfactants, where the free OH signal is negligible once complete surface coverage is reached.[174] Estimates from the surface tension data indicate that at this high concentration, the area per MA molecules is on the order of 150-200 $\AA^2$ which is more than double that of a surfactant such as sodium dodecyl sulfate (SDS). These results then suggest that MA adsorption is not completely disrupting water at the top most layer and therefore must not pack tightly enough to fully cover the surface. The spectral characteristics of water at longer wavelengths are consistent with increased presence of MA at the surface. What appears to be an increase in OH response around 3200 $cm^{-1}$ is consistent with progressively stronger

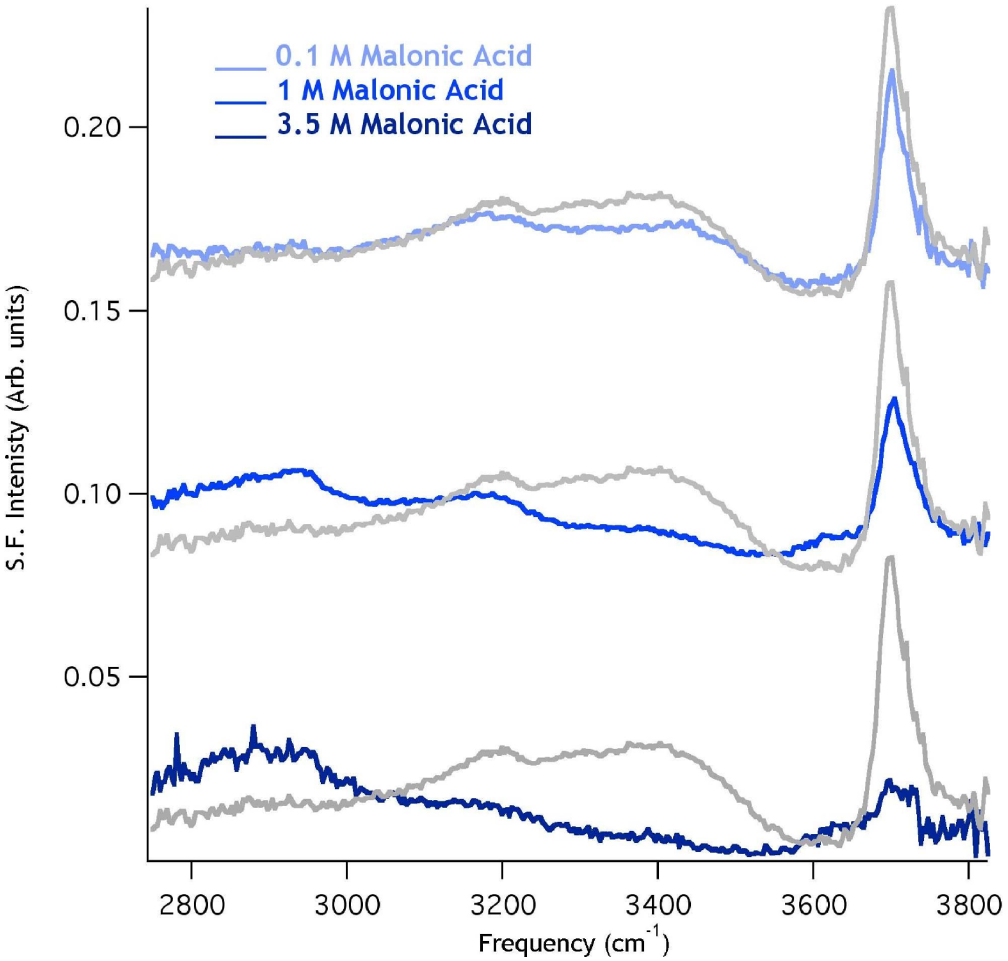

FIGURE 6.3. VSFS of water/CH region for 0.1 M, 1 M, and 3.5 M aqueous malonic acid. The gray spectra are neat water.

surface OH bonding with the presence of MA. However, as noted above, the signal from C-H modes complicate the interpretation in this region.

### 6.4.2. Surface Tension Results

Previous studies investigated thoroughly the surface tension of MA on $H_2O$.[160–162] The results reported here are in excellent agreement with the earlier work. Surface tension measurement, a macroscopic technique, coincides with the overall surface concentration, whereas VSFS simultaneously measures both surface concentration (number density at the surface) as well as molecular orientation.[90] By combining the results of these two complementary techniques, a more complete picture of the adsorption of MA at the surface is created. Figure 6.4. shows the comparison between surface tension data, and the changes in the amplitude of the SSP and SPS data with changing MA concentration. As the bulk concentration of MA increases from 100 mM to 3 M, the surface tension decreases from values near that of pure water (73 mN/m)[175] to approximately  65 mN/m; further increases in concentration do not affect the surface tension substantially, and eventually become impossible due to the solubility limit of MA in water.[161] The intensity of the VSFS C=O (SSP and SPS) signal over the same concentration range rises analogously. The increases in intensity are most dramatic between 0.5 M and 3 M, which is also the concentration range where surface tension measurements show the greatest change. Considering the unchanging frequency response in the VSFS signals and surface tension trends, the adsorption that occurs at the surface as a function of concentration does not significantly change the orientation of the carboxylic C=O modes, but does increase the total number of modes at the surface.

### 6.4.3. pH Effects on Adsorption

The two different VSFS polarization schemes show differing frequency responses for the C=O signal (1740 $cm^{-1}$ versus 1730 $cm^{-1}$). C=O bonds oriented perpendicular to the interface (sensitive to SSP) have a different bonding environment than those parallel to the interface (sensitive to SPS). To test this, studies were performed by adjusting the pH, causing the protonated carboxylic acid to turn into a resonance-stabilized carboxylate ion that completely removes the carboxylic C=O

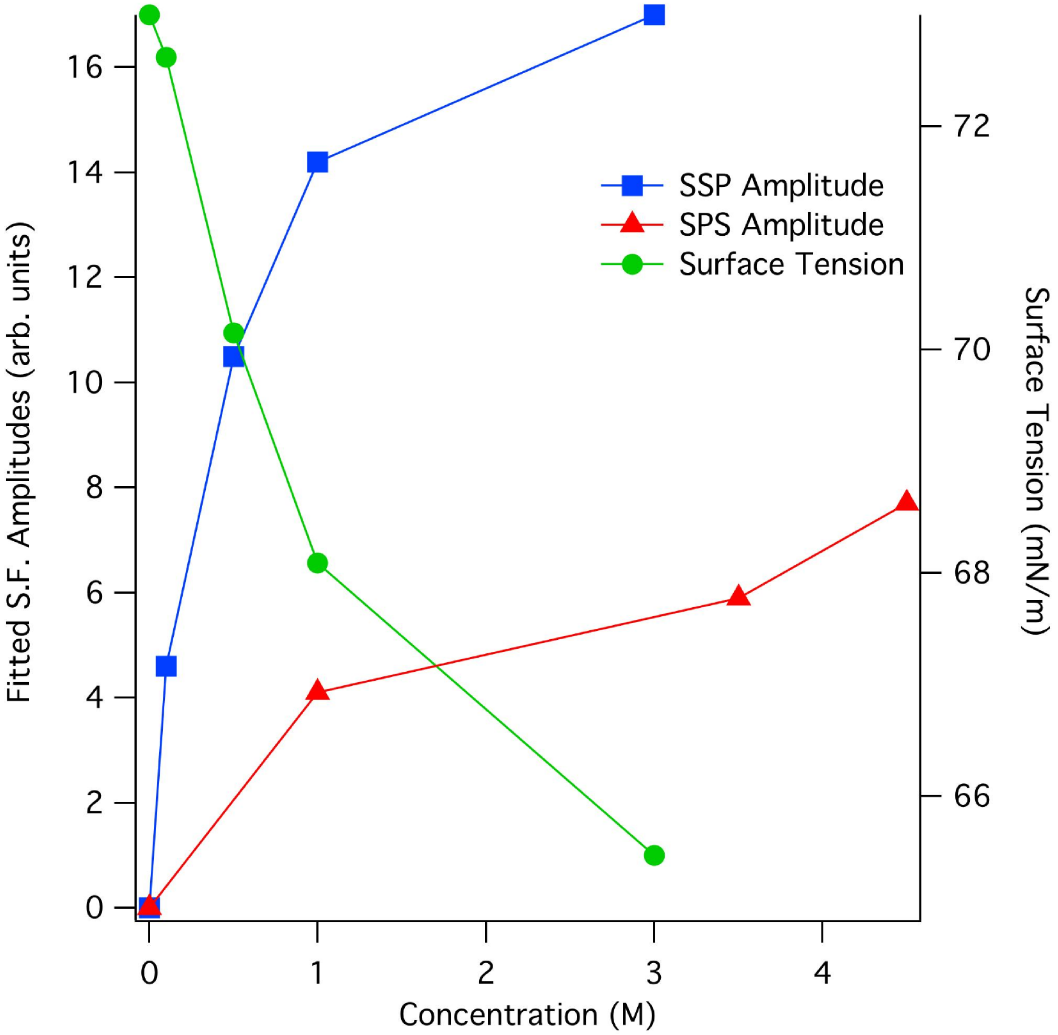

FIGURE 6.4. Plot of malonic acid concentration vs fitted VSFS amplitudes (left axis) and surface tension (right axis).

spectral response. At a constant concentration of acid (1 M), the bulk pH was adjusted and spectra of the C=O region were recorded in both SSP and SPS schemes. The pKa values for MA are 2.85 and 5.70.[175] At a pH of 3, the bulk percentage of the fully protonated MA approaches 40% with the singly protonated form near 60%. At a pH of 4, the fully protonated form should account for approximately 7%, the singly protonated form 91%, and the completely dissociated form near 2%. At a pH of 6, the fully protonated form should not exist, a third of the acid molecules are singly protonated, and the remaining two thirds are completely dissociated. Figures 6.5. and 6.6. show the spectral response of the MA C=O as a function of bulk adjusted pH as well as corresponding spectral fits. The VSFS signal intensity of the carboxylic C=O region decreases as the bulk-adjusted pH is increased, but does not track the bulk pKa closely. At a bulk pH value of 3, the SSP scheme (Figure 6.5.) clearly shows signal with fitted amplitude near that of the native pH solution. In the SPS scheme (Figure 6.6.), the signal at pH 3 is very low in intensity, making it difficult to obtain. At a bulk value of pH 6, the SSP scheme has a dramatic decrease in signal (especially noticeable from pH 4 to pH 5). The resulting signal, while small, is still detectable at pH 7 and does not completely disappear until values of pH above 8. In the SPS scheme, signal is not detected above pH 3.

The SPS data of Figure 6.6. are all fit to the same peak parameters as that of the native 1 M solutions. The SSP data of Figure 6.5. are similarly fit, however the fit quality deteriorates above pH 4. The deterioration is remedied by increasing the Gaussian widths. This is indicative of a change in environment and is most likely due to signal originating from the singly protonated form as opposed to the fully protonated form of MA. By combining the results from the SSP and SPS schemes, it is clear that these schemes probe carboxylic C=O modes that are non-equivalent and that the pH behavior (protonation state) at the surface is not the same as the bulk pH.

### 6.4.4. pH Effects on Surface Tension

To the best of the authors' knowledge, the following constitutes the first published study of surface tension of bulk pH adjusted MA solutions. Surface tension values are

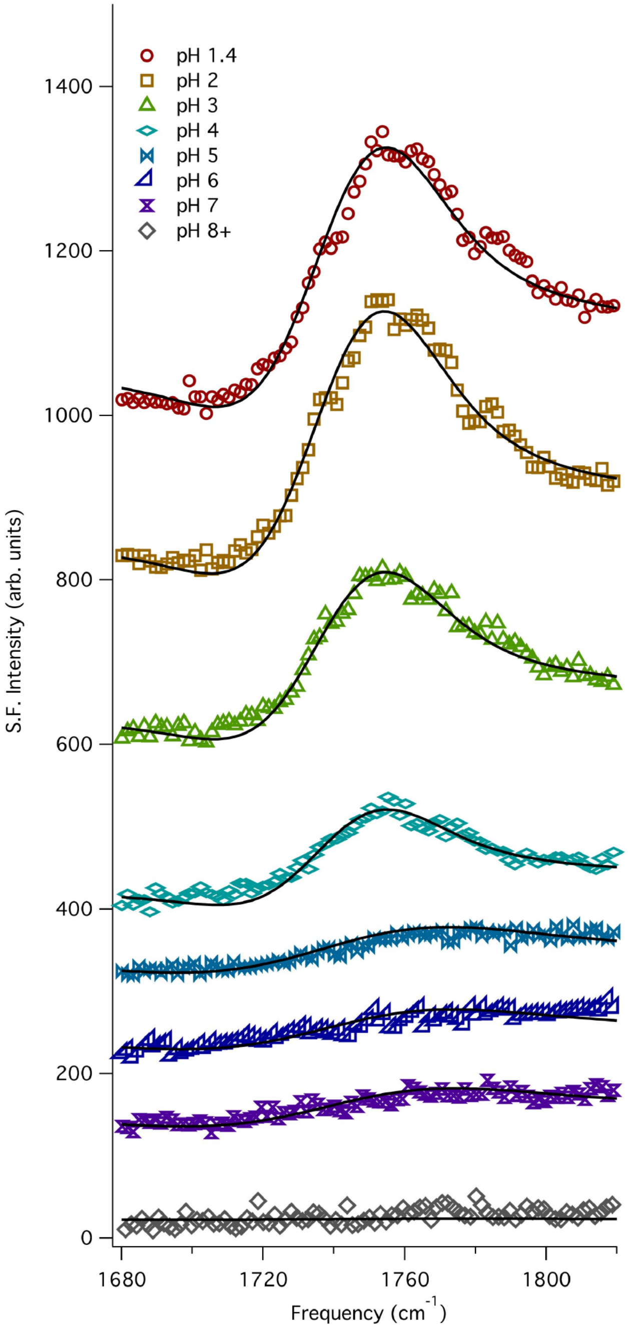

FIGURE 6.5. VSFS-SSP spectra of carboxylic C=O of aqueous malonic acid at 1 M with bulk adjusted pH values from native (top) to >8 (bottom). The spectra are offset for clarity.

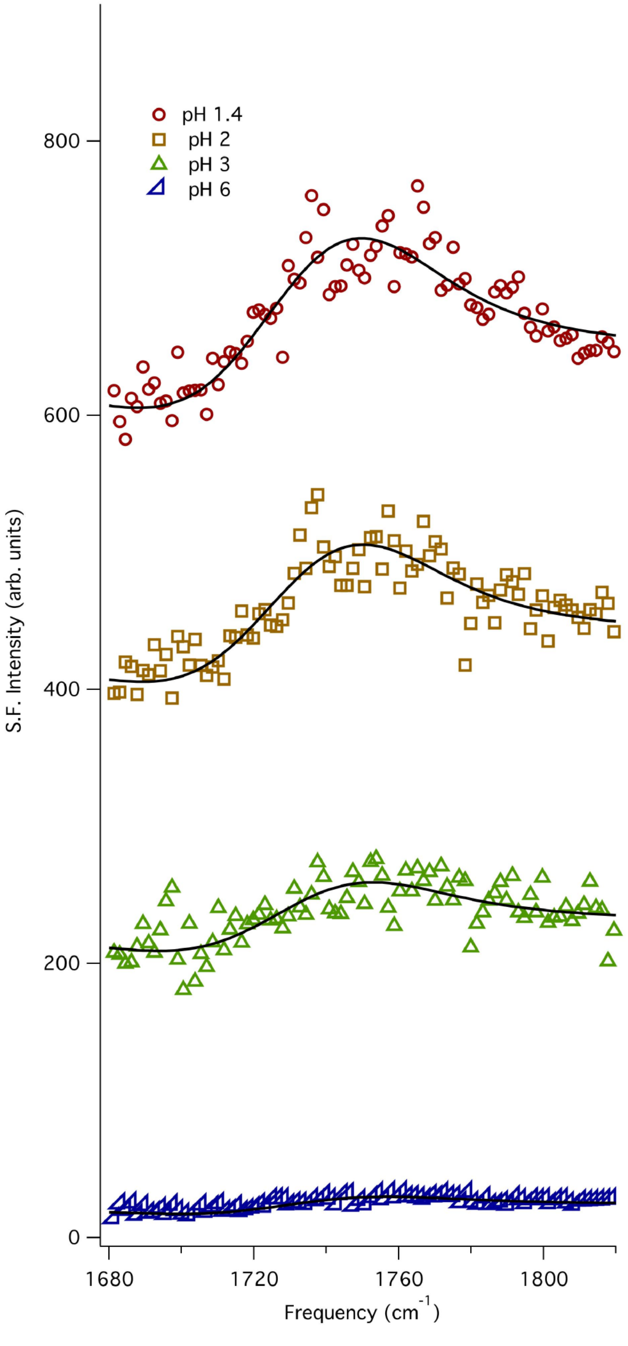

FIGURE 6.6. VSFS-SPS spectra of carboxylic C=O of aqueous malonic acid at 1 M with bulk adjusted pH values from native (top) to 6 (bottom). The spectra are offset for clarity.

plotted in Figure 6.7.. Also plotted is an integrated intensity for VSFS measurements performed in SSP and SPS. As the pH is adjusted to 2, there is a slight increase in surface pressure as well as SSP polarized VSFS signal. As the bulk adjusted pH increases, the surface pressure and the VSFS intensity decrease. The surface pressure drops to zero after pH 7 while the SSP VSFS intensity drops very slowly in the range of pH 5 to 7 until finally decreasing to zero above pH 8. The surface tension experiments exhibit an almost linear decrease as the pH is increased from pH 2 to pH 7. Classically, this behavior indicates desorption, whereby malonic acid is no longer adsorbing to the surface at higher pH values. However, the results combined with VSFS give us a much more interesting picture. It is obvious that MA is still adsorbed at high pH values as seen by the SSP VSFS results. In addition, the malonic acid molecules present at the interface at these high pH values are at least singly protonated due to the presence of a detectable carboxylic C=O signal.

### 6.5. Malonic Acid Orientation

Discussion of the molecular orientation of malonic acid begins with a description of the angles used in the following analyses. Because the carbon atoms form the backbone of the malonic acid molecular structure, determining the orientation of the three atoms is the first step in understanding the overall orientation of the molecule in space with respect to a water surface. Two angles describe the orientation of the carbon chain backbone, and two dihedral angles orient the molecule internally. All the angle definitions described below are depicted in Figure 6.8.

The group of three carbon atoms forms a moiety with a $C_{2v}$ symmetry. The two C-C bond vectors have a bisector between them. This chapter refers to the bisector as a vector pointing out from the central carbon in the direction of the other two carbon

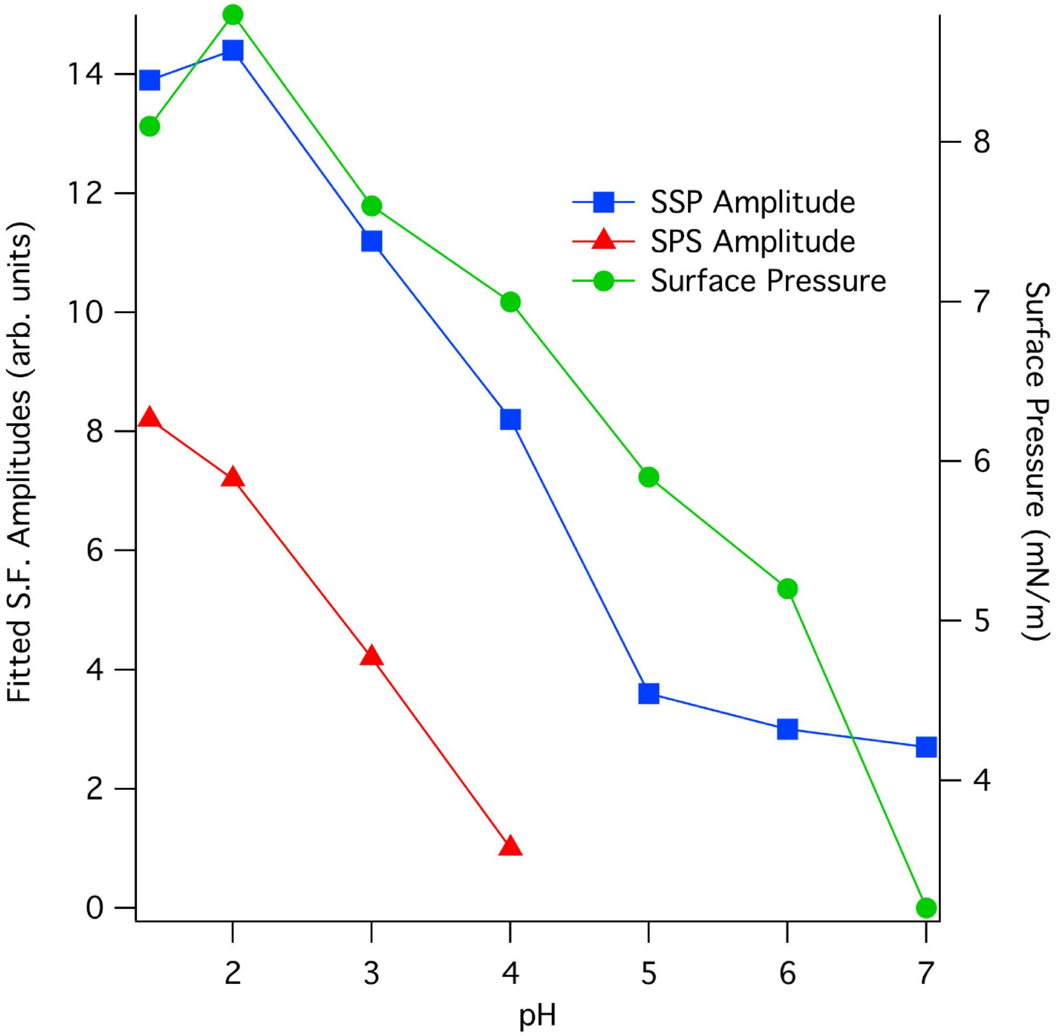

FIGURE 6.7. Plot of fitted VSFS amplitude vs surface pressure for bulk adjusted pH 1M malonic acid.

atoms. The first angle defined, $\theta$, describes the "tilt" of the triatomic carbon chain that forms the acid's backbone. The angle $\theta$ is calculated as the angle formed between the carbon group bisector vector and a reference axis oriented perpendicularly to the water surface, pointing out of the water bulk towards the gas phase side of the water interface. When $\theta = 0°$, the bisector vector aligns with the reference axis. A value of $\theta = 90°$ places the bisector vector in the plane of the water surface, perpendicular to the reference axis. Rotating the bisector to $\theta = 180^\circ$ makes the bisector anti-aligned with the reference axis, pointing in towards the water side of the interface.

The second angle used to orient the malonic acid carbon backbone, $\phi$, describes a molecular “twist” of the malonic acid. This twist angle is defined as a rotation of the plane formed by the three carbon atoms around the bisector axis. For different orientations of the angle $\theta$, the distribution of $\phi$ will necessarily become isotropic because of the symmetries of the plane of the aqueous slab surface. However, the value of $\phi$ is necessary to describe the overall molecular orientation for $\theta$ values near $90^\circ$. When $\theta = 90^\circ$, the bisector of the carbon atom group lies parallel to the water surface. In such a configuration, $\phi = 0^\circ$ means the plane of the carbon atoms orients perpendicularly to the plane of the water surface. Likewise, $\phi = 90^\circ$ lays the plane of the carbon atom group flat on the surface, parallel to the plane of the water interface.

The planes formed by the atoms of the carboxylic acid groups orient by rotation of two dihedral angles, collectively referred to as $\psi$ because they are not uniquely identified, referenced to the plane of the three backbone carbon atoms. The dihedral angle $\psi$ is the angle of rotation of the C-C bond between the central methylene carbon, and a carbonyl carbon of a carboxylic acid moiety. The reference orientation that sets $\psi = 0^\circ$ is defined by two conditions: 1) the plane of the atoms of the carboxylic acid orients parallel to the plane of the three carbon atoms, and 2) the carbonyl C=O bond vector (pointing from the C to the O) points to the same side as the C-C-C bisector vector (i.e. the inner product of the bisector vector and the carbonyl bond vector has a positive value: $\overline{C = O} \cdot \overline{bisector} > 0$). A dihedral angle of $\psi = 90^\circ$ rotates the O=C-O plane perpendicular to the C-C-C plane. Lastly, $\psi = 180^\circ$ rotates the carboxylic acid such that the carbonyl is anti-aligned with the C-C-C bisector. The various orientations of the dihedral angles are depicted in Figure 6.8., and characterize

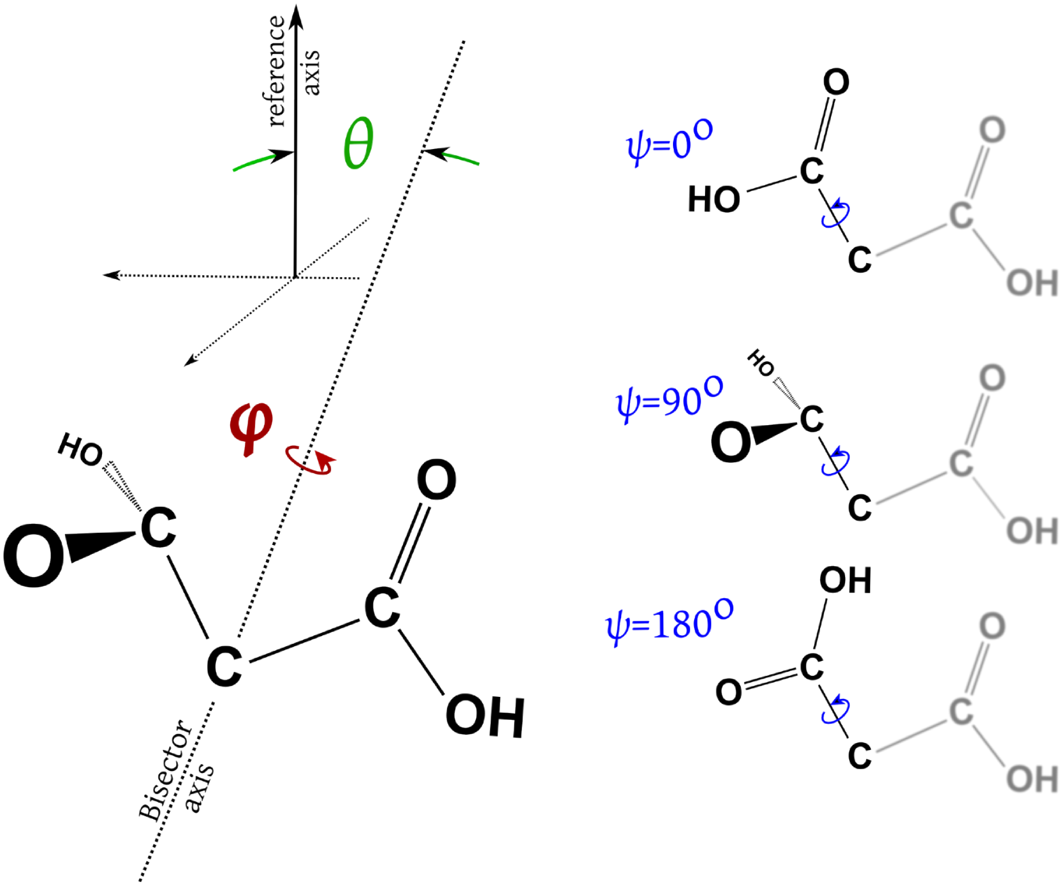

FIGURE 6.8. Definitions of the angles used to orient malonic acid molecules in space, (left) $\theta$ and $\phi$, and (right) internally, $\psi$.

the internal orientation of malonic acid. By combining all four of the described angles with information about the acid position within the simulation box, we are able to develop a nearly complete picture of the orientational behavior of malonic acid relative to a nearby water surface.

### 6.5.1. Carbon Backbone Orientation

Bivariate angle distributions of $\theta$ and $\phi$ were calculated for the three carbon backbone atoms, and are shown in Figure 6.9. The set of plots represents slices through the interface parallel to the water surface. Each slice is located at the distance labeled in the top-right of the respective plot. Positive positions are further into the vacuum phase, and negative positions are further into the water side of the interface. A distance of 0 Å is located at the water surface location. The location of the surface, and all calculations performed to relate interfacial position are done using a method of averaging top-most water molecule positions, fully described in our previous publication.[19] The molecular center of mass determined the position of each malonic acid.

In each set of axes of Figure 6.9., the values of $\theta$ and $\phi$ are plotted along the horizontal and vertical, respectively. The plots are two-dimensional histograms colored by the intensity (i.e. population) of the location in the angle space. Intensities for all plots were normalized such that the highest intensity (1.0) is colored in dark red, and lowest intensity (0.0) is dark blue. Areas in the plots characterized by uniform coloration indicate an isotropic distribution of angles. A concentrated region of uniform coloration indicates an orientational preference in one or both of the angular degrees of freedom.

The plot at a position of 2 Å in Figure 6.9. shows the orientation of the acid carbon backbones just above the water surface. These acid molecules are most likely less solvated than those further in to the water bulk. The most distinguishing feature is the vertically-running band of intensity to the right of the plot centered between 135° and 180°. This results from a population of acid molecules with their three carbon atoms oriented with the bisector vector pointed more than 45° into the water bulk. $\phi$ is spread nearly isotropically in this distribution. However, due to the symmetry of the $\theta$ angle as a spherical coordinate (i.e. a single $\theta$ value describes a cone in space) $\phi$ will necessarily become more isotropic relative to the interface, or spread

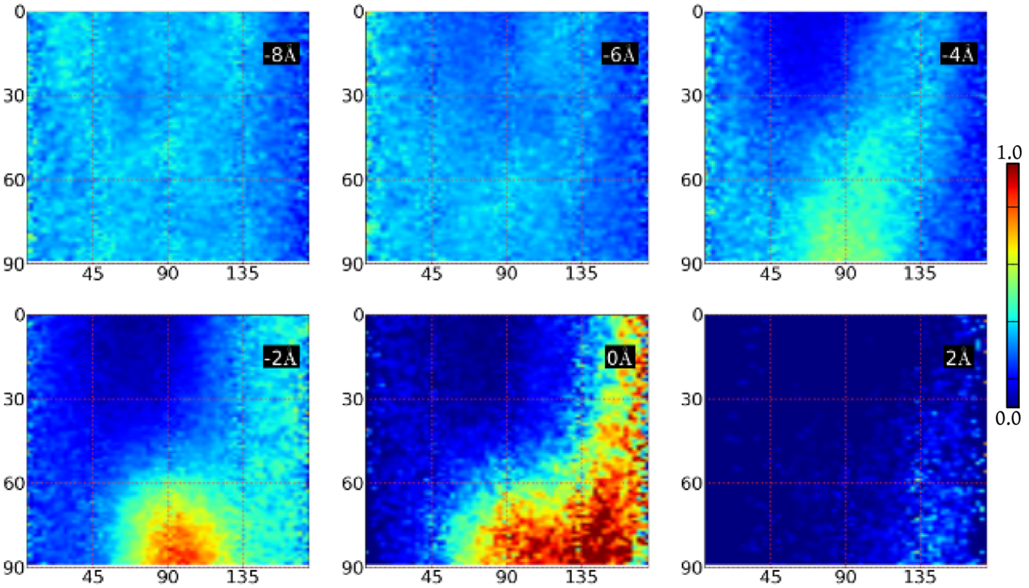

FIGURE 6.9. Bivariate distributions of the "tilt" and "twist" of the malonic acid carbon chain at different interfacial depths.

out across the two-dimensional plots, as $\theta$ takes values near its extrema. $\theta$ values closer to 90° require $\phi$ to fully describe the orientation.

At 0 Å and below, acid carbon backbone orientations are more complex. A second population of orientations forms at 0 Å, manifested in the plots as a region of intensity centered at $\theta = 90°$, with $\phi$ also concentrated towards 90°. This indicates a carbon atom group lying flat in the plane of the water surface. Additionally, as the depth of the molecules increases from 0 Å to -4 Å, the population above $\theta = 135°$ decreases, shifting intensity to the peak at $\theta = 90°$. The distribution spreads out both in $\theta$ and in $\phi$. For acid molecules deeper into the water bulk, likely more solvated by waters, the orientational freedom expands in $\theta$ and $\phi$, until at -6 Å there is a loss of orientational preference, resulting in a flat (evenly colored) distribution, and isotropy of the carbon backbone group orientation.

At -4 Å the $\theta$ distribution expands below $\theta = 45°$. This is due to a population of submerged malonic acid molecules with their bisectors aimed slightly up towards the water surface. Thus, we establish that the influence of the interface on molecular orientation extends both above and below the water surface, and lasts to a depth of at least 4 Å into the water bulk.

### 6.5.2. $CH_2$ Orientation

For each acid molecule, the orientation ($\theta$) of the carbon backbone affects the position and orientation of the molecule's methylene hydrogens. An orientation of $\theta = 90°$, and for all $\phi$ values, there are two hydrogens (one from each methylene) in a rather symmetrical configuration with one above and one below the backbone's plane, which is itself parallel to the plane of the water interface. With $\theta = 90°$, variation in $\phi$ results in the plane formed by each H-C-H rotating from perpendicular ($\phi = 0°$) to parallel ($\phi = 90°$) to that of the water surface. Consider acid orientations near $\theta = 90°$ and further consider the vector defined by each methylene's C-H bond. The geometry of the acid is such that each of these C-H bond vectors has a component perpendicular to the plane of the interface and whose magnitudes are identical. Effectively, these 'perpendicular to the water interface' components are mirrors or each other.

Furthermore, if the $\theta$ distribution is symmetric around $\theta = 90°$ (as in the -2 Å plot of Figure 6.9.), then the perpendicular components of the two methylene C-H bonds negate each other. The carbon group $\theta - \phi$ distributions at or below the water surface ($\leq 0$ Å) exhibit this quality. VSFS experiments failed to produce any spectral features related to the methylene $CH_2$ modes of malonic acid. We propose that the aforementioned orientational symmetry of the methylene C-H bonds about the water surface, and the low population of malonic acids above the surface location, manifests spectrally in polarized VSFS experiments as a lack of intensity where the C-H bond features are expected.

### 6.5.3. Carbon Backbone Dihedral Angles

Having established the orientation of the carbon backbone atom group from the $\theta - \phi$ distributions of Figure 6.9., we now turn to analysis of the internal geometry of carboxylic acid moieties near the water surface. The two carboxylic acid groups rotate around the two C-C bonds, quantified by their dihedral angles. The magnitudes of the dihedral angles fall in the range $0° \leq \psi \leq 180°$. The O=C-O atomic plane is parallel to the C-C-C plane at $\psi = 0°$ and $\psi = 180°$, and the two planes are perpendicular at $\psi = 90°$, as discussed above and depicted in Figure 6.8. The two dihedral angles are plotted in a set of bivariate distributions in Figure 6.10. The arrangement of the axes in the figure is identical to that of Figure 6.9., but with each axis representing one of the two $\psi$ angles.

Figure 6.10. shows that the dihedral orientations are strongly related with a preferred rotation of 90° apart from each other. The two very concentrated peaks in the plots are located at $\psi = 0°$ and $\psi = 90°$. This results from the carboxylic O=C-O atomic planes of the two carboxylic acids aligning perpendicularly to each other. The topmost plot at 2 Å is not symmetric between the two dihedral angles with only a single peak in the distribution (located at the left-center of the axis). This is an artifact of how the carboxylic acid groups were enumerated computationally, and indicates that the top-most malonic acids above the water surface take on a fixed dihedral orientation, rarely switching values (i.e. rotating the molecule to flip the alignment of both carboxylic acid groups).

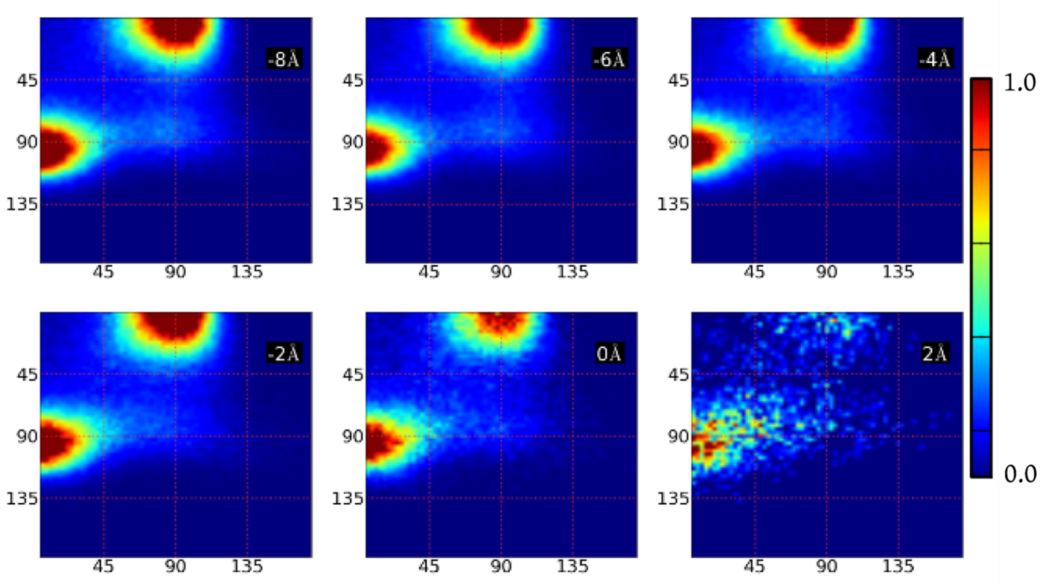

FIGURE 6.10. Bivariate orientation distributions of the two internal dihedral angles of malonic acid.

One of the carbonyl C=O bonds is preferentially aligned in the same direction as the carbon group bisector ($\psi = 0°$), and in the plane of the three carbons. The other carbonyl C=O bond points perpendicular to the plane of the carbon group atoms. The strong orientational preference is observed both in the bulk of the water and at the water surface location.

There remains one final set of orientational data necessary to fully characterize the interfacial malonic acid. The $\theta - \phi$ distributions of the carbon atoms show that the acid carbon chain lies flat when at the water surface (0 Å), and tilts with the bisector pointing further into the water bulk when the malonic acid is slightly above the water surface. The $\psi - \psi$ dihedral distributions show one C=O carbonyl bond mostly aligned with the carbon group bisector and the other carbonyl aligned normal to the plane of the carbon atoms. The question remains as to which direction does the latter carbonyl C=O bond vector point? Is it pointed into the water side of the interface, or does it point out towards the gas phase away from the water bulk?

The tilt angle of the C=O bond, $\theta_{C=O}$, determines this carbonyl orientation. Like the carbon group bisector tilt angle, $\theta_{C=O}$ is referenced to the axis normal to the plane of the water surface, pointing out towards the gas phase side of the interface.

Figure 6.11. shows the angle distribution of $\theta_{C=O}$ plotted as a function of the malonic acid molecular center of mass position. Most of the distribution is isotropic in the tilt angle up to positions several Å beneath the water surface location.

Starting above the surface (positions $> 0$ Å), the distribution bifurcates into two distinct angle regions. There is a protrusion in the distribution (region 'A' in Figure 6.11.) beginning just below 0 Å and extending above the surface, centered at $\theta_{C=O} = 90°$. A second peak in the distribution (region 'B') is concentrated towards the bottom of the plot near $\theta_{C=O} = 180°$. At this position slightly above the water surface, it is more clear that one of the carbonyl C=O bonds points into the water (the bond oriented near $\theta_{C=O} = 180°$), and the other points more out into the plane of the surface and often slightly angled out from the water phase. When an acid molecule located at, or just above, the water interface exhibits this internal orientation, it means that one carbonyl bond is oriented pointing more towards bulk water while the other is oriented towards the gas phase. It is reasonable to presuppose then, that the bond oriented towards the bulk water will have more interaction with the water environment than its partner carbonyl on the other end of the acid.

Further down into the water surface, the angle distribution spreads over a much larger range until becoming isotropic near -2 Å. However, a feature appears at -3 Å and extends down slightly past -8 Å into the water phase (region 'C' in Figure 6.11.). In this region there is a decreased intensity in the histogram for $\theta_{C=O} > 120°$.

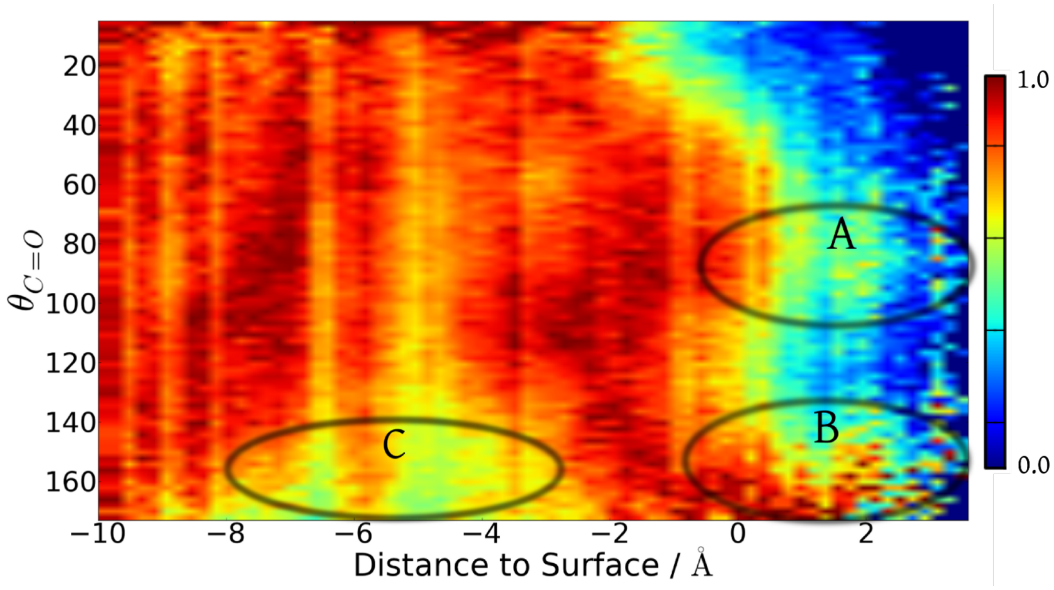

FIGURE 6.11. Orientational depth profile of malonic acid carbonyl C=O tilt angle, $\theta_{C=O}$, plotted against the molecular center of mass position.

This shows a population of malonic acid carbonyl C=O bonds pointing less into the water bulk. At this depth, the carbon backbone orientation distribution becomes relatively more isotropic, but there remains a population of acids with $\theta_{CCC} < 90°$ (i.e. the carbon group bisector aims further towards the water surface), in agreement with the carbonyl bond behavior, and the carboxylic dihedral orientations.

These orientational distributions paint the following picture of malonic acid orientation broken into interfacial depth regions: 1) Above the water surface the carbon group bisector tilts down towards the water, and the carbonyl bonds orient with one bond pointing towards the water phase (potentially increasing the interactions with surface waters), and the other carbonyl bond pointed out of the water either parallel to the plane of the surface, or slightly out towards the gas phase. 2) At the water surface location (0 Å) the carbon group lies mostly flat in the plane of the surface. The methylene C-H bonds align symmetrically above and below the surface. Also, the carbonyl C=O bonds have a similar orientation to those further out of the water, but the carbonyl bond tilt distribution quickly becomes isotropic just a few Å under the surface location. 3) At -4 Å and down to approximately -6 Å, the carbon group $\theta - \phi$ distributions broaden and quickly become isotropic. The distribution of the carbonyl bond tilt, $\theta_{C=O}$, shifts intensity at this lower depth leaving a low-intensity region at approximately $120° \leq \theta_{C=O}$. Both carbonyls orient to point more towards the water surface at this depth than slightly above or below. 4) Further down in the water bulk, below -8 Å, the distributions become isotropic and malonic acid assumes bulk-like behavior.

## 6.6. Summary

Malonic acid has interesting surface behavior that is not fully revealed solely by macroscopic experimental measurements. VSFS results demonstrate that carboxylic C=O oscillators can have two distinct frequencies, implying distinct hydration and bonding environments. If the carbonyl dipole is parallel to the plane of the interface a lower energy frequency is recorded, while if the oscillator is perpendicular to the plane, a higher energy frequency is recorded. pH studies of malonic acid adsorption corroborate the distinct environments of carboxylic C=O moieties, and also provide evidence that surface malonic acid likely has different pKa values from bulk. Computational results confirm the conclusions from the VSFS results and provide quantifiable distributions of malonic acid orientation as a function of depth into the water surface.

The results reported herein indicate a malonic acid molecule that lies mostly flat on the surface of an aqueous solution. There is a competition at the interface between the hydrophobic alkane spacer removing itself from the water, and the hydrophilic carboxylic ends further solvating in water. This results in the frequency shift of the carboxylic C=O modes that has not been seen previously for bulk aqueous malonic acid. In addition, malonic acid adsorbs to an aqueous interface, as evidenced by experimental and computational techniques.

There have been spectroscopic studies showing shifts of the carboxylic C=O mode up to 1740 $cm^{-1}$, but these samples were either crystalline malonic acid[176, 177] or deliquesced samples.[178] For these samples, the splitting of the carboxylic C=O is due to intermolecular hydrogen bonding (cyclic dimerization) and subsequent splitting of the C=O spectral features into an out of phase mode (IR active) located at higher wavelengths, and an in phase (Raman active) mode that is located at lower wavelengths.[176] The VSFS results here present a feature that matches the high frequency value but there was no signal arising from the lower frequency region. Finally, at high concentrations of malonic acid, there was a drop in intensity in the VSFS signal. Since there is an inversion center with a cyclic dimer, any dimerized malonic acid molecules would no longer be sum frequency active.[90] It may be that as the concentration is increased to near the solubility limit, dimers begin to form. The drop in intensity of the VSFS signal from desorption can be ruled out due to surface tension measurements.

It is possible that malonic acid can form a six-membered ring involving a hydrogen bond between the alcoholic hydrogen on one carboxylic moiety and the carbonyl oxygen on the other carboxylic moiety. Computational studies have shown that while this may occur in the gas phase, there is no evidence for ring formation in solution unlike the mono-anion which has been shown to adopt a ring structure.[179, 180] While the VSFS studies herein do not show evidence of a ring structure at the interface, there is computational evidence for ring formation at the interface. This will be discussed in more detail in a later publication.[20]

While much work has been done on the thermodynamic aspects of aqueous malonic acid in order to predict and describe the properties of a binary aqueous malonic acid aerosol, these results provide a complete picture of how this acid adsorbs and orients at a vapor/water interface, and also fascinating insights into how the chemistry at an interface can greatly differ from that of the bulk.

Chapter VII presents the follow-up DFT-MD computational study of malonic acid on a water surface. The DFT-MD simulation analyses are compared to the classical interaction potential results. Additionally, a noteworthy intramolecularly bound form of malonic acid is documented, and its behavior at the water interface is compared to the unbonded form.

# CHAPTER VII

# MALONIC ACID CONFORMERS AND HYDRATION

This work was co-authored, and the manuscript is in preparation to be submitted for review for publication. Dr. Geraldine Richmond supplied computational resources and project support. Eric Shamay was the principle investigator for this work.

## 7.1. Introduction

Despite our recent experimental and theoretical achievements with simple organic acids in environmentally relevant systems, it is clear that our scientific understanding has far to go. The interfacial region of an aqueous solution is a turbulent and dynamic environment where the behaviors of even small organic molecules evade definition. How does the interfacial region alter behavior and strength of organic acid solutes? Do acid molecules interact with water at a surface as they do in bulk? What hydrate species and behavioral differences occur at an interface that are not found deeper in a liquid phase? Experiments addressing these types of questions give us valuable insight and information, but have not to date fully captured actual microscopic behaviors and events. Computationally, however, these systems can be more fully characterized. Coupling computational results with previous experimental work provides a much more complete picture of acid behavior throughout aqueous interfacial regions.

Organic acids are a particularly interesting candidates for studying aqueous acid behavior. Dicarboxylic acids are a pertinent class of hygroscopic, water-soluble, and atmospherically relevant bolaamphiphilic molecules, receiving much attention in recent years both experimentally,[147–155, 181–194] and in theoretical computational studies.[183, 186, 194–201] They vary in size from the smaller oxalic acid to larger humic-like substances.[145, 146] Dicarboxylic acids make up an appreciable amount of the atmospheric organic particulate matter, and are implicated in the nucleating condensation of clouds.[156, 192, 195, 196, 202, 203] Because of their presence in the atmosphere from biogenic and industrial processes, in various types of particulates and aerosols, they are known to affect climate conditions and atmospheric chemistry.[142–144, 181, 187–193, 195, 196, 202–204]

Malonic acid, the second-smallest of the dicarboxylic acids, has been studied in binary and heterogeneous reactions, and in aerosols to develop cloud nucleation models.[163, 164] It has previously been studied experimentally with several recent publications attesting to its importance.[157–159, 161, 162] Many computational theoretical works have also probed the nature of malonic acid in small cluster systems, at aqueous surfaces, and in gas phase.[179, 180, 201]

Ab initio molecular dynamics (MD) techniques are used to model and simulate the hydrating water structures that form around an interfacial malonic acid in water. The quantum MD technique described herein allows more realistic and accurate simulation than the previous classical MD study reported in chapter VI.[21] That work determined net orientational behavior of malonic acid, coupled with experimental spectroscopic results to build a refined model of the acid's behavior at the air/$H_2O$ interface. However, the classical interaction potential used needs to be tested against accurate quantum potentials to further verify the validity of the results obtained.

Quantum DFT MD simulation is the natural follow-up to the classical MD study as the interaction potential accurately reproduces hydration geometry around surface acid molecules. From the simulation data we examine in detail the specific bonding interactions that occur between surface waters and the carboxylic acid moieties of the malonic acid molecule, and look at the geometries and orientations of the hydrated acid molecule. Five concurrent simulations have been performed in this work, each of a malonic acid molecule bound to a water system surface. Each system was simulated at a temperature, solution concentration, and pH set to match the conditions of the complementary experimental studies.[21] The experiments showed that an aqueous malonic acid has a surface propensity in low-pH conditions. Although conclusions regarding the specific nature of those surface-bound hydrate complexes could only be inferred from experimental results, previous and current computational simulations provide insights about the hydrated geometries of the acid molecules, and their orientational behavior.

This computational study is a necessary step in the development of models of malonic acid, and to continue building the picture of aqueous acid behavior. This chapter presents a comparison between the classical and DFT interaction potentials to verify the validity of fully atomistic classical potential. Documented here is the internal geometry of surface malonic acid molecules, and behavioral implications of an interesting intramolecularly hydrogen-bonded species of malonic acid. These results complement several experimental and computational studies of the intramolecular interaction in several organic diacid conformers.[179, 180, 183, 194, 196, 198, 200, 205–208] Also shown is the orientational behavior of the aqueous surface acid molecule interacting with neighboring waters, specifying how the acid orients both with respect to the water surface, and internally by twisting about the carbon backbone bonds. The final analysis is of the vibrational behavior of the carbonyl modes of the acid to compare with and complement the previous experimental results, and to further strengthen the link between computational and experimental efforts.

## 7.2. Computational Methods

On-the-fly ab initio molecular dynamics simulations were performed with the QUICKSTEP package, which is an implementation of the Gaussian plane wave method using the Kohn-Sham formulation of density functional theory (KS-DFT).[13] The Kohn-Sham orbitals are expanded using a linear combination of atom-centered Gaussian-type orbital functions. The electronic charge density was described using an auxiliary basis set of plane waves. Energies and forces from on-the-fly simulation sampling of the Born-Oppenheimer surface were calculated for each MD step using the Gaussian DZVP basis set, the exchange-correlation functional of Becke, Lee, Yang, and Parr (BLYP),[34] and the atomic pseudo-potentials of the Goedecker, Teter, and Hutter type.[33] A simulation timestep of 1 fs was used, with a Nose-Hoover thermostat set at 300K. These computational parameters were verified to yield a reasonable description of bulk room temperature water both when simulating a neat-water system, and in our previous computational studies with additional constituents.[14]

Five acid-water systems of unit cells sized 10x10x15 $\text{Å}^3$ were created as starting points for concurrent simulation. Each unit cell was initially randomly packed with 34 water molecules, and 2 HCl molecules. The system size was then expanded by an additional 10 Å in the long cell dimension to final dimensions of 10x10x25 $\text{Å}^3$. Periodic boundaries were then set on all axes to form an infinite aqueous slab configuration. A single malonic acid molecule was then added onto the top of each water cell within 2 Å of the topmost water molecule to simulate a malonic acid at the topmost point of contact with a water surface. Each of the five system energies were then minimized through a geometry optimization procedure. Subsequently, each system was equilibrated for 1 ps in canonical ensemble (NVT) conditions. Using the equilibrated systems as starting points, each was simulated for a further 40 ps in the microcanonical ensemble (NVE), with coordinate snapshots recorded every 1 fs. This simulation process resulted in 40,000 time steps of system trajectory for analysis in each of the five system replicas.

### 7.3. Hydration Structure

To compare the KS-DFT and classical interaction potentials, the $O_{mal}$-$H_{wat}$ radial distribution functions (RDF) are given in Figure 7.1. (where the subscripts “mal” refers to one of the malonic acid oxygens, either alcohol or carbonyl, and “wat” refers to water hydrogens). Both the KS-DFT (black) and classical (green) interaction potential RDFs are plotted in Figure 7.1. The two RDFs shown are of the $O_{alcohol}$-$H_{wat}$ (left) and the $O_{carb}$-$H_{wat}$ (right). There is reasonable agreement between the hydration structures calculated using the different interaction potentials. This similarly is an indication that some features of the water packing around the carboxylic acid groups are reproduced by the less exact classical potential, in comparison with the more accurate KS-DFT interaction potential. Differences in the RDFs suggest the two interaction potentials disagree mostly in the first solvation shell. In the alcohol oxygen plot, the classical potential results in significantly more structure in the first peak, while the trend is reversed in the plot of the double-bonded carbonyl oxygen RDF. This is likely due to the inability of the classical potential to fully reproduce resonance structures of the carboxylic acids, which would lead to a more symmetric solvation structure than the KS-DFT. The inability of the classical interaction potential to capture the asymmetry of the solvation structure will becomes more apparent on examining restricted regions near the interface. Thus, although the classical potential produces a similar average structure, it does not fully capture the resonance structure that is likely very important in the hydrogen bonded states of the malonic acid.

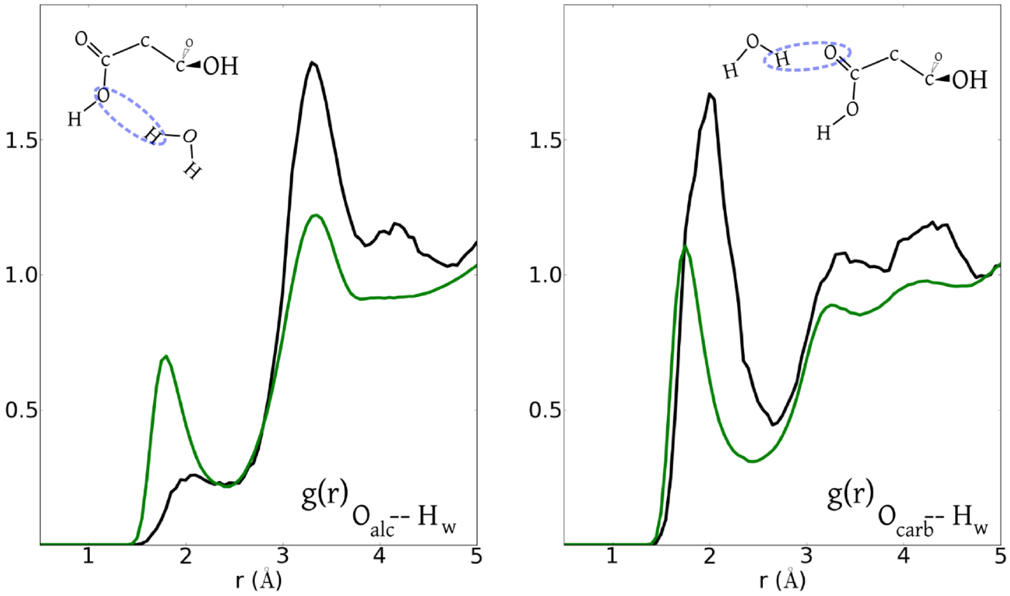

FIGURE 7.1. RDFs of malonic acid oxygens and water hydrogens.

## 7.4. Bond Lengths

Our first analysis is of atomic distances within the malonic acid molecules in an effort to study the internal geometry of the acid. Looking at the acid alcohol moiety's O-H distance also verifies the protonation state to ensure that the imposed low-pH conditions effectively keep the surface malonic acid fully protonated throughout the simulations. The bondlength trajectory (i.e. the inter-atomic distance as a function of time) of each of the acids O-H bonds is plotted in Figure 7.2. (dark blue and green traces) for both of the carboxylic acid moieties of two representative simulations. Color-coded markers around each bond of the molecular graphic to the right of the plots designates the atom pair used to calculate each trace. Both O-H distance traces remain very close to the expected equilibrium O-H covalent bondlength of 1 Å for the entire trajectory, indicative of a protonated acid. All five simulated malonic acids were verified by this method to be fully protonated throughout the trajectories.

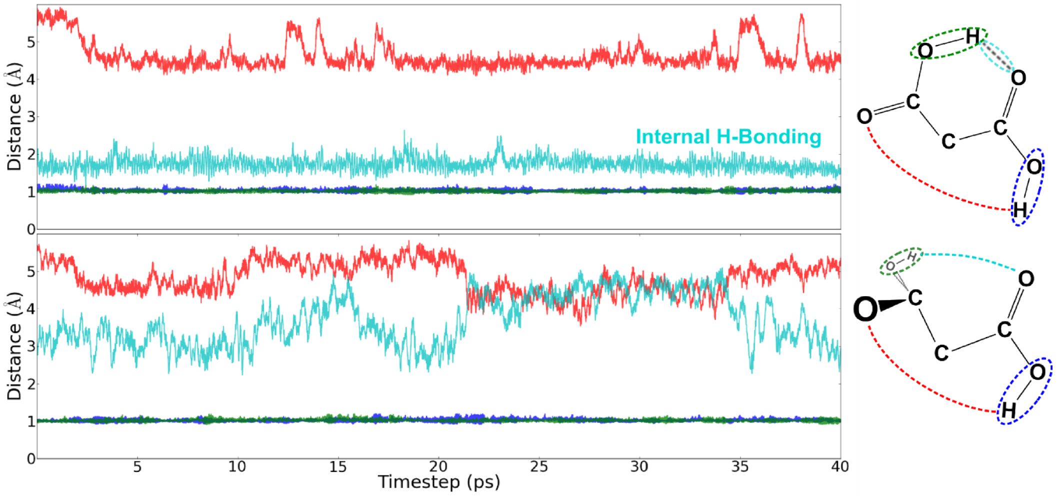

FIGURE 7.2. Bond trajectories of malonic acid intramolecular distances between the acid (green and dark blue) O-H distances, and (light blue and red) protons and carbonyl oxygens on the opposite ends of the molecule. (top) an example of an IHB bond trajectory, and (bottom) an IUB trajectory.

The distances between atoms of malonic acid were inspected for the simulated trajectories, and a noteworthy atomic bonding pattern occurred in two of the five simulations. Figure 7.2. also shows the plots of distances between each acid proton and the carbonyl oxygen on the opposite end of the molecule (in red and light blue). The top plot of Figure 7.2. shows the case where one of the two $O_{carb}$-$H_{acid}$ distances is significantly shorter than the other, spending nearly the entire trajectory at a distance close to that of a strong hydrogen bond (e.g. $< 2.4$ Å). The bottom plot shows a simulation where both $O_{carb}$-$H_{acid}$ distances remain longer than an H-bond. The former case (top plot) is hereafter referred to as the "internally bonded" or "intramolecularly H-bonding" (IHB) molecule, and the latter case (bottom plot of Figure 7.2.) is referred to as the "internally unbonded" (IUB). These two stable conformers were predicted in early computational studies, where the IHB conformation was found to have the lowest energy.[179, 208, 209] However, only the IUB conformer was predicted to be stable when in aqueous solution. A graphic depiction of the proposed structure of these two conformers is shown in Figure 7.3., with the IHB form exhibiting an interaction between one acid hydrogen and a carbonyl oxygen at the opposite end of the molecule.

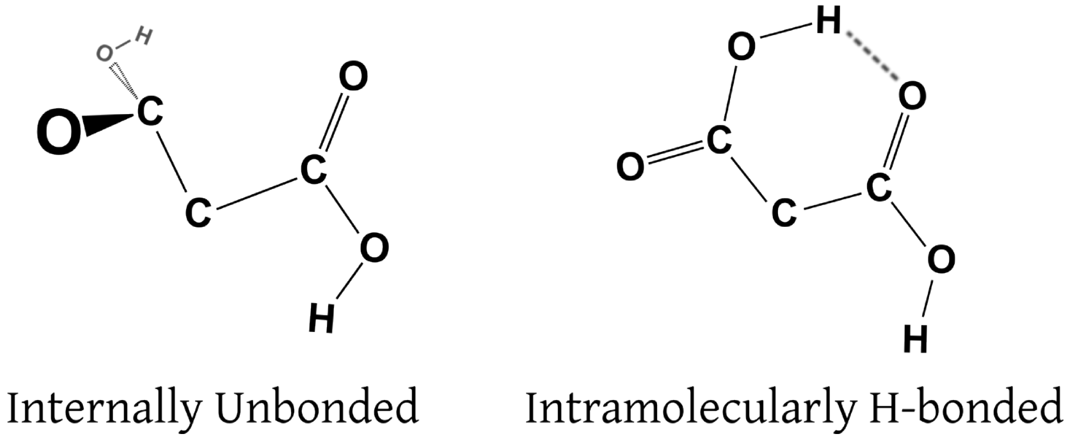

FIGURE 7.3. Two conformations of malonic acid encountered during simulation. (left) IUB and (right) IHB conformations.

Referring to Figure 7.3., the presence of a hydrogen bond internal to the acid causes the molecule to fold into a ring-like structure of six atoms. The intramolecular H-bond initially formed during the equilibration phase in two of the five simulations. Clearly, it is strong as once formed it remained for the entirety of the simulations. Conversely, in the simulations exhibiting IUB molecules, the intramolecular H-bond forms only briefly, or not at all in the simulated trajectories. Additionally, all simulation cells were initialized with malonic acids with identical internal geometries, albeit randomly placed and oriented on the water surface. This suggests that the formation of the IHB configuration is a result of the initial placement of the acid with respect to the simulated water molecules in the system, i.e. the initial solvation of the acid.

The unique internal bonding behavior of malonic acid is thus demonstrated with two of the five simulations exhibiting the IHB configuration. The other three simulated acids remained IUB. To highlight differences and similarities in the remainder of this report, and to show trends in behavior of malonic acid on a water surface, the analysis proceeds to present results that differentiate between both sets (IHB and IUB conformations) of simulations, as well as the sum-total of data from all the simulations.

Figure 7.4. shows the distribution of bondlengths for the covalent O-H bonds, the $O_{carb}$-$H_{acid}$ distances, and also the C=O carbonyl bonds, using the same color scheme as in Figure 7.2. The top plot shows the bondlength distribution for the IUB malonic acid simulations, and the bottom plot shows the distributions for the IHB acid molecules. The insets of Figure 7.4. expand on the region containing the O-H alcohol, and C=O carbonyl moieties. The bondlength distribution plots further emphasize trends noted earlier, and show other configurational changes in the malonic acid molecules.

In the top plot of Figure 7.4., each pair of distributions corresponding to each bond type, are of similar width and mostly overlap because they each have very similar peak locations. This is indicative of a malonic acid where both ends of the molecule behave similarly, most likely due to similar hydration environments. This also suggests that the IUB malonic acid orients symmetrically with respect to the water surface in order to achieve equal solvation for both carboxylic acid groups (i.e. the acid likely lies flat in the plane of the surface keeping both carboxylic acid ends at equal depths).

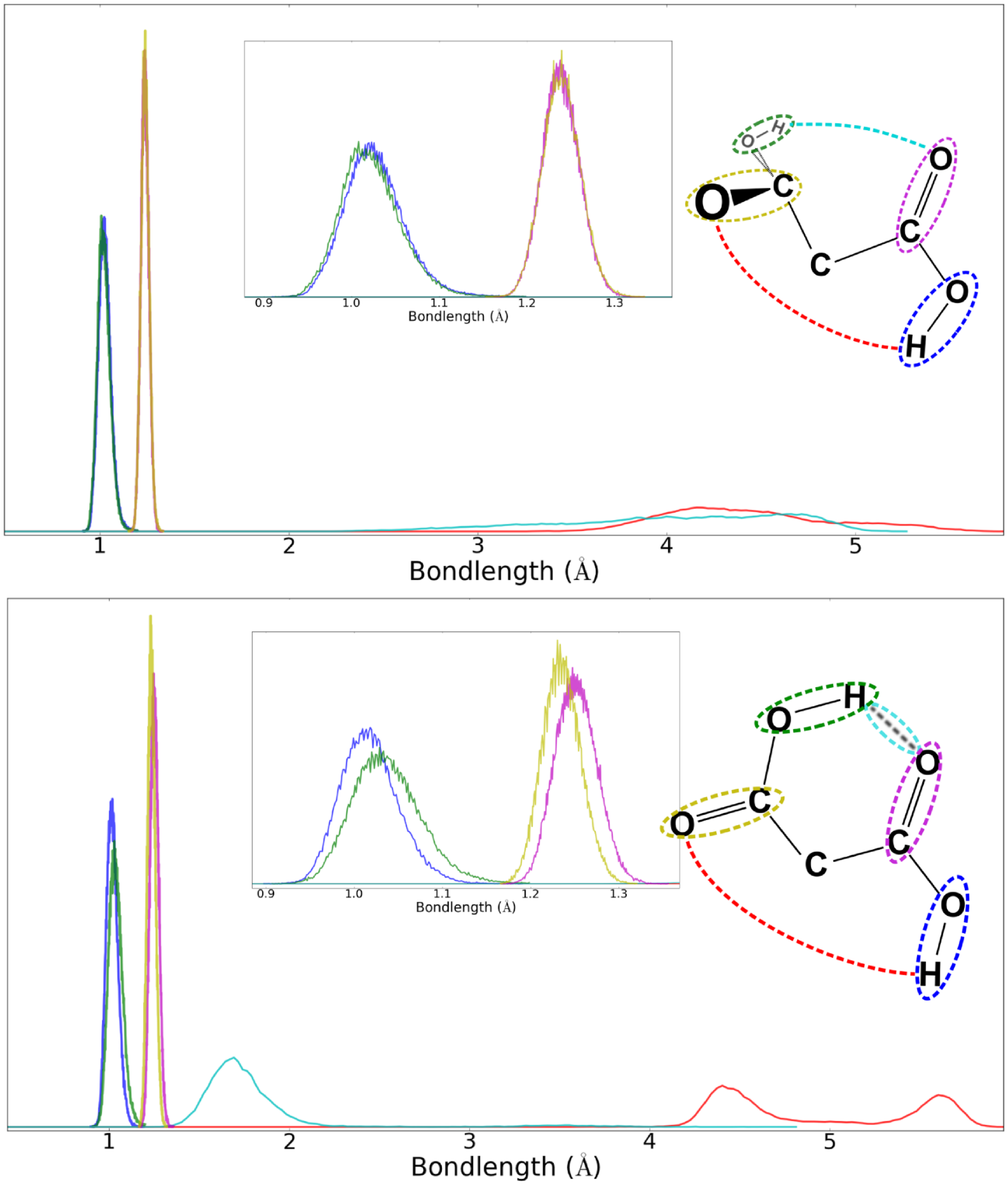

FIGURE 7.4. Distributions of inter-atomic distances for the O-H and $O_{carb}$-$H_{acid}$ bonds, and also for the two carbonyl C=O bonds of each malonic acid. (top) IUB, (bottom) IHB. (insets) expanded regions of the two alcohol O-H, and carbonyl C=O bondlengths.

The case of the internally bonded acid molecule (bottom plot of Figure 7.4.) is different in many respects. The distribution of the lengths of bonds at both ends of the molecule are not overlapped as in the IUB case. The distribution of one of the bonds of a given type (e.g. the carbonyl C=O bond) is shifted to longer lengths than the same bond at the other end of the molecule (e.g. one of the C=O carbonyl bondlength distributions is shifted to longer distances relative to the distribution of the other carbonyl in the opposite carboxylic acid group). With regards to the internal hydrogen bond, the light blue peak is entirely shorter than a typical H-bond length in water (approximately 2.4 Å), whereas the other $O_{carb}$-$H_{acid}$ distance is greater than 4 Å. Interestingly, there are two distinct peaks in the non-bonding $O_{carb}$-$H_{acid}$ distribution (red trace) indicating two distinct conformations of the internally bonded malonic acid. These conformations shorten or lengthen the unbound $O_{carb}$-$H_{acid}$ distance at different times during the simulations.

The presence of the intramolecular H-bond affects covalent bonding geometry throughout the malonic acid. Looking at the two O-H peaks in the bottom plot of Figure 7.4., centered near 1 Å, one is shifted to longer bondlengths (green) than the other (dark blue). The green colored trace corresponds to the alcohol moiety that is participating in the IHB. The delocalization of the bonding electrons in a hydrogen bond allows the hydrogen proton to move further from its covalently bound oxygen, shifting the bondlength distribution to the right relative to the unbonded O-H (colored dark blue). Interestingly, the C=O carbonyl bonds behave similarly. The maroon colored bondlength distribution corresponds to the internally H-bonded carbonyl oxygen. The entire bondlength distribution is shifted to longer distances compared to that of the carbonyl not participating in the internal H-bond (yellow trace). The bondlength averages and standard deviations of the distributions are listed in Table 7.5., quantifying the changes to the bondlengths. These geometric changes result in other behavioral differences, both orientationally and spectrally, as described later in this work.

|  | Unbonded |  | H-bonded |  |
|---|---|---|---|---|
| Bond | Length | std | Length | std |
| $C_1O_1$ | 1.239 | 0.021 | 1.252 | 0.024 |
| $C_2O_2$ | 1.239 | 0.022 | 1.236 | 0.022 |
| $H_1O_2$ | 4.455 | 0.444 | 4.938 | 0.545 |
| $H_2O_1$ | 4.054 | 0.606 | 1.793 | 0.374 |
| $H_1O_a$ | 1.023 | 0.034 | 1.038 | 0.039 |
| $H_2O_b$ | 1.027 | 0.034 | 1.019 | 0.033 |

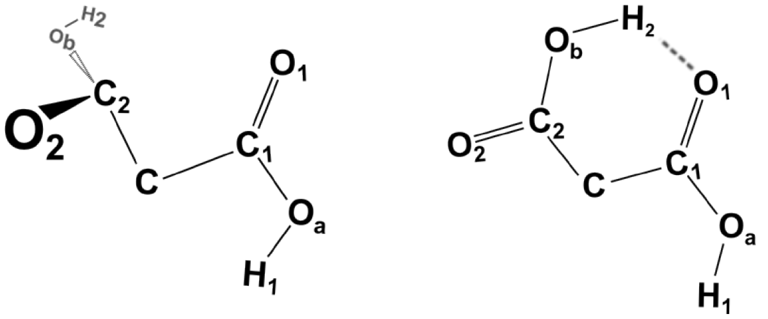

FIGURE 7.5. Average inter-atomic distances (i.e. bondlengths) between various pairs of atoms in malonic acid, and their standard deviations.

### 7.5. Molecular Orientation

Hydration of malonic acid by neighboring surface waters strongly affects its surface behavior. A change in the water environment around the acid can strongly alter the overall orientation of the molecule with respect to a water interface. The following analysis examines molecular orientation of malonic acid using a set of angles to define the molecule's orientation in space at an aqueous interface, and the acid molecule's internal orientation.

Here is briefly introduced the angles used in the analysis, and a graphical depiction of their definitions in Figure 6.8. for reference. For a complete discussion of the angles used in the analysis, the reader is referred to the previous publication that fully defines them.[21] First, consider the molecular orientation of the three carbon atoms that form the acid's backbone. Two angles, $\theta$ and $\phi$, describe the carbon backbone "tilt" and "twist", respectively. The tilt angle, $\theta$, is measured from a reference axis (herein defined as the vector normal to the plane of the water interface, pointing away from the water phase) to the carbon-group bisector axis (bisecting the two C-C bonds, and pointing from the central carbon towards the direction of the other two carbon atoms). The backbone twist, $\phi$, is rotation of the carbon group about the bisector axis. If the bisector lies in the plane of the water interface such that $\theta$=90°, the twist will have a value of $\phi$=0° when the plane of the three carbons is perpendicular to the plane of the water surface. A combination of $\theta$=90° and $\phi$=90° indicates an orientation with the plane of the carbon group lying flat to the plane of the water surface.

Furthermore, it is possible to orient the carboxylic acid moieties in the molecule by quantifying the dihedral angle, $\psi$, for each of the two acid groups. The angle $\psi$ is a rotation of the plane of the O=C-O atoms of a carboxylic acid group relative to the plane of the three carbon atoms. An orientation aligning the carbonyl bond vector (pointing from C to O) of a carboxylic acid group parallel to the carbon group bisector results in a dihedral of $\psi$=0°. Depictions of the angle definitions, and various values of $\psi$ for one of the carboxylic acid groups, are shown in Figure 6.8. for reference.

Plots of the $\theta$-$\phi$ distributions are provided in Figure 7.6. Three bivariate histograms are shown, depicting the orientational trends of the carbon backbone group. In these normalized intensity plots, highest intensity regions are colored darker red (1.0), and low intensity regions are colored dark blue (0.0). Regions of the plots exhibiting uniform coloration indicate isotropic behavior, whereas concentrated regions of high intensity show a preference for a particular orientation given by the specific angle combinations.

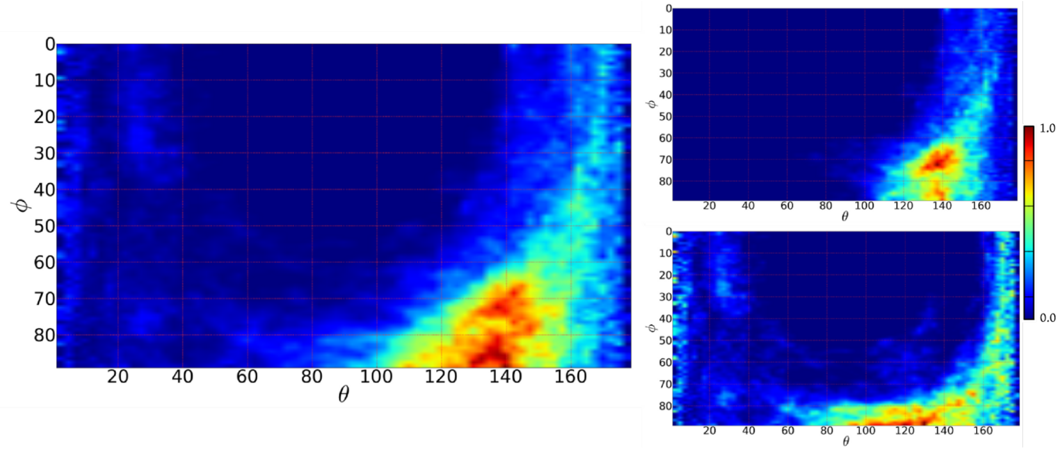

FIGURE 7.6. Intensity plots of the bivariate distributions of the two carbon group angles, $\theta$ and $\phi$. (right) plots of the contributions from the (top) IUB and (bottom) IHB malonic acids.

The larger plot on the left of Figure 7.6. shows the distribution collected from the data of all five simulations. The highest intensity region is centered at $\theta$=135°, and $\phi$=90°. This indicates an orientation of the plane of the carbon backbone group tilted 45° from the plane of the water surface with the central carbon further out towards the gas-phase side of the interface than the two carbonyl carbons. Additionally, the $\phi$ values show that the two carbonyl carbons are both at similar depths into the water side of the interface.

Although the entire range of $\theta$ and $\phi$ values are found in the distribution, the bulk of the intensity is concentrated around $\theta$=135°, and very little appears in the region below $\theta$=90°. Thus, there is a clear orientational preference established for the carbon group atoms, and this has a direct effect on the orientation of the other atoms in the molecule.

These orientational results complement those found in our previous classical force field simulation study of malonic acid.[21] In that study the behavior of the top-most malonic acid molecules on a water surface exhibited a very similar $\theta$-$\phi$ distribution as in the results shown in Figure 7.6. However, in the classical simulations, acids located deeper into the water bulk reoriented, resulting in interfacial layering of orientational preferences that changed with depth. In the present work, none of the simulated molecules moved into the water side of the interface (i.e. penetrated the water bulk). Likely, this is because of the length of the simulations. Hence, only the top-most acids on a water surface are represented in the simulations, and comparison with the results from the previous classical simulations are limited, accordingly.

The results of the $\theta$-$\phi$ analysis were further broken down to differentiate between IUB and IHB systems. These are plotted on the top-right and bottom-right of Figure 7.6., respectively. IUB systems exhibit a very strong orientational preference in $\theta$. The IUB set of acids are entirely oriented with $\theta > 90°$, and the distribution is tightly concentrated around $\theta$=135°. The twist, $\phi$, is concentrated around a value of $\phi$=75°, with a smaller high-intensity region at $\phi > 80°$. As the twist angle decreases from 90° the two ends of the carbon atom chain move to different depths in the interface. Upper values of $\phi$ in the most intense region of the distribution reach near $\phi$=60°, resulting from a twist that sends one end of the molecule 30° further out of the aqueous surface than the other. Thus, each carboxylic group (as they occupy the end positions) will experience a unique solvation environment. One being more bulk-like, the other less so.

Turning now to the IHB malonic acid $\theta$-$\phi$ plot of Figure 7.6., slightly different orientational preferences occur. The region of highest intensity is concentrated at $\phi$=90°, but spread over a wide range of $\theta$, approximately between $90° < \theta < 150°$. Furthermore, $\theta$ values in the plot span the entire range down to $\theta$=0°. Clearly the intramolecular bonding leads to greater orientational freedom of the carbon backbone as evidenced by the broader distribution and greater range of orientations. This is intuitively expected for a molecule that has less bonding to neighboring waters due to an internal hydrogen bond partially occupying both carboxylic acid functional groups. Water is less likely to interact with a malonic acid that has fewer binding sites, and will not stabilize the acid's position or orientation as strongly as it would an IUB molecule. Thus, the internal H-bond gives the acid molecule access to many more orientations on the water surface than its counterpart: the IUB acid.

The internal geometry of malonic acid is defined here by the two dihedral angles that quantify rotations of the carboxylic acid groups about the molecule's two C-C bonds. As mentioned earlier, the angle $\psi$ is referenced by the co-planar alignment of the C=O carbonyl bond with the C-C-C group bisector. Figure 6.8. depicts various orientations of a carboxylic acid group and the accompanying values of $\psi$. The overall $\psi$-$\psi$ distribution is plotted on the left of Figure 7.7. with the plots of the IUB and IHB systems to the right in the figure on top and bottom, respectively. It is not distinguished here between the two carboxylic acid groups of the acid molecules. Consequently, the horizontal and vertical axes of the $\psi$-$\psi$ plots are arbitrarily assigned to one of the two acid dihedral angles. The larger plot of all simulation data is overwhelmed by the high intensity concentration at the $\psi$-$\psi$ region of 0°-180° at the bottom left of the plot. Much lower intensity regions appear throughout the $\psi$-$\psi$ range.

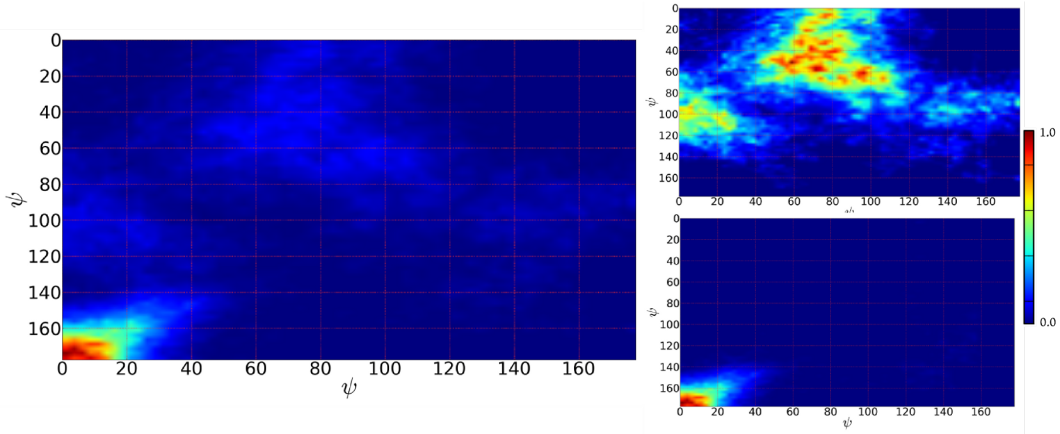

FIGURE 7.7. Intensity plots of the bivariate $\psi$-$\psi$ distribution of the two malonic acid O=C-C-C dihedral angles.

Looking to the IHB plot at the bottom right of Figure 7.7. it is clear why the larger plot of all the data sets is similarly concentrated at the bottom left of the plot. All of the intensity of the IHB acids indicates that the two carbonyl C=O bonds are aligned anti-parallel to each other. The strong H-bond holds the internal geometry nearly fixed with very little distortion through bending of the acid's six-atom ring structure, or twisting of the carboxylic acids around the C-C bonds. An intense and highly concentrated region of the dihedral angle distribution is indicative of a stable, virtually rigid form of the IHB malonic acid.

The IUB malonic acids exhibit a very different behavior in their carboxylic acid orientations. The top-right plot of Figure 7.7. shows the much broader, less concentrated distribution resulting from acids without the internal H-bonding constraints. The broad regions of low intensity throughout the distribution demonstrates the molecule's much greater flexibility, a consequence of having the two carboxylic acid ends of the molecule much more decoupled. However, a trend is apparent in the distribution of the two dihedral angles. Note the two regions of intensity in the plot located at the center-left and top-center. In our previously published results of the complementary classical interaction potential simulations,[21] the $\psi$-$\psi$ distributions throughout the interfacial region had two similarly located regions. In that study the regions of the plot were more concentrated over small areas at $\psi$-$\psi$ values of 0° and 90°. That combination is indicative of the dihedrals aligning 90° from each other, i.e. perpendicularly. One of the C=O bonds is aligned parallel to the C-C-C bisector ($\psi$=0°), and the other is perpendicular to the plane formed by the C-C-C atoms ($\psi$=90°). The correspondence of the two regions in the distribution of the present work to those of the classical simulations is noteworthy. The classical force field reproduces the dihedral trend of two peaks in the distribution, but the much smaller range of $\psi$ angles suggests that the corresponding dihedral term in the classical potential needs to be adjusted to better recreate the KS-DFT results for higher accuracy. The present results, however, demonstrate that without further modifications, there is reasonable agreement between the KS-DFT and classical interaction potentials with regards to the overall orientation of surface malonic acid molecules. The shortcoming of the classical interaction potential is its inability to properly capture the IHB conformation.

Having now established the $\theta$-$\phi$ orientational trend of the carbon backbone atoms, and the $\psi$-$\psi$ dihedral relationships, this establishes a nearly complete orientational picture of malonic acid on a water surface. What remains is to determine the absolute orientation of both carboxylic acid groups with respect to the plane of the water surface. In order to compare the computed orientational results with recent experimental results,[21] determined by the SFG spectra of the carbonyl modes of malonic acid, the configuration of the carboxylic acid groups is now discussed.

Specifically, the analysis presented shows how the carbonyl C=O bond vectors orient relative to the reference axis normal to the plane of the interface, forming a carbonyl tilt angle, $\theta_{C=O}$.

The distribution of $\theta_{C=O}$ is presented in Figure 7.8. The black plot shows the distribution of angles from all simulation datasets. The red and blue plots correspond to the $\theta_{C=O}$ data collected only from the IHB, and IUB simulations, respectively. In all the distributions two angle regions dominate in intensity, appearing as peaks from approximately 50°-120°, and 150°-180°. The former angle range corresponds to carbonyl C=O bonds pointing in the plane of the water surface ($\theta_{C=O} = 90°$ indicates a carbonyl parallel to the plane), slightly above, or slightly below the plane. The latter range indicates carbonyl bonds pointing directly in towards the water side of the interface ($\theta_{C=O} = 180°$) or within a cone of approximately 30° tilt from the reference axis into the water bulk.

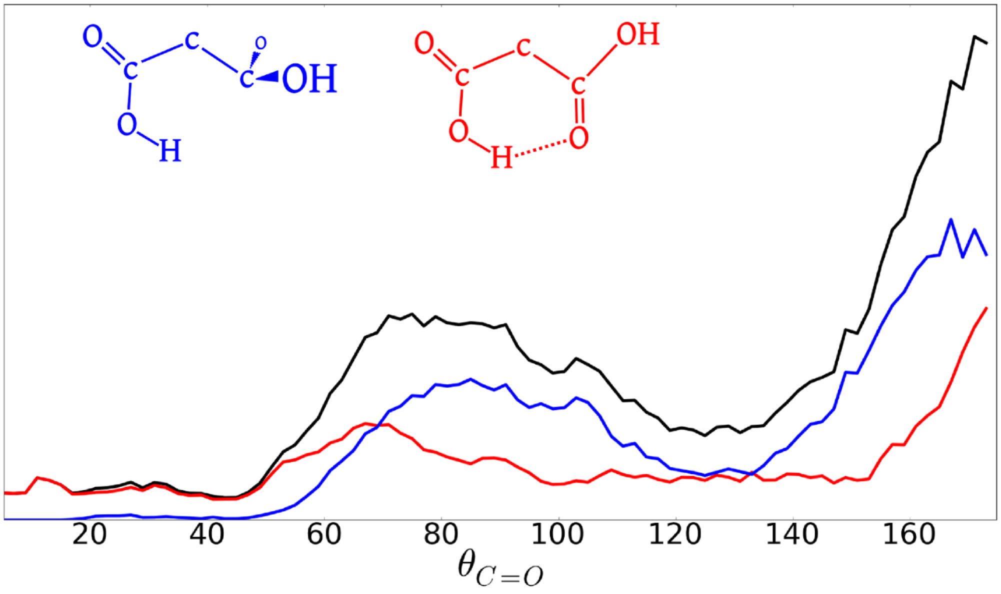

FIGURE 7.8. The tilt angle, $\theta_{C=O}$, of the two carbonyl C=O bonds of malonic acid (black) for all simulations, (blue) for IUB simulations, (red) IHB simulations.

Looking at the individual red and blue plots, there are some differences between how the internal bonding conformations behave. The lower peak of the blue plot is centered at approximately $\theta_{C=O} = 90°$, extending up to 30° to either side. The peak near 180° extends down to 130°. Between the two peaks there is a small intensity, whereas for $\theta_{C=O} < 50°$, there is no intensity as the distribution drops to zero.

The red plot, representing the IHB acids, is lower in overall magnitude than the blue plot because only two of the five simulations are represented. Additionally, there is intensity throughout the entire $\theta_{C=O}$ range, as compared to the blue plot which shows little intensity at the lower angles. The location of the lower red peak is centered near $\theta_{C=O} = 70°$, which is almost 20° lower than the equivalent blue distribution peak. The width of the red peak is smaller, narrower by approximately 20°. The peak at 180° similarly narrows by nearly 20°.

In both sets of simulations there is a clear trend for malonic acid to point one of its carbonyl bonds into the water side of the interface ($\theta_{C=O} = 180°$), while the other bond points in the plane of the interface, or slightly above of below it ($\theta_{C=O} \approx 90°$). The formation of the internal H-bond slightly shifts the angle of the in-plane carbonyl to point further out away from the water side of the interface ($\theta_{C=O} \approx 70°$). Also, the IHB acids enjoy a greater orientational freedom in their carbonyls overall (i.e. the distribution has intensity throughout all angle regions), but the peaks in the distribution are narrower than for the IUB molecules. It is likely that the orientation of the carbonyl bonds on the water surface is affected by their solvation environments, and hydration by surface waters. The IHB malonic acid has a peak in the distribution of $\theta_{C=O}$ that lies slightly further to the left (i.e. lower angle values) than its unbonded counterpart. Lower angle values indicate a carbonyl bond tilt further out from the surface, away from the water bulk. This slight orientational difference likely leads to a difference in the strength, or amount of hydration on this particular carbonyl bond. The effect of this will become apparent spectrally, and may lead to interesting chemical differences between the two conformations.

## 7.6. Bond Spectra

Knowing the orientational behavior of malonic acid helps to establish a model for how the molecule behaves on an aqueous surface. To link this computationally derived model to the experimental work, the computed spectra of one of the functional moieties of the acid molecules is examined. The bondlengths of the carbonyl C=O bonds were calculated for each simulation at each timestep (similar to the results presented earlier in Figure 7.2.) to generate a time-dependent function, $f(t)$. A calculation was then performed on the time function to generate the power spectrum of the bond lengths, $I(t)$, hereafter referred to as a “bond spectrum”. While not fully encapsulating the response of dipole transition moments or recreating IR or SFG spectra, the frequencies captured in a bond spectrum are representational of the local mode frequencies expected from experimental spectroscopic studies, and are directly comparable.

Figure 7.9. shows the C=O carbonyl bond spectrum averaged from all the simulations (top, black spectrum). The two colored spectra in Figure 7.9. show the contributions of the IHB and IUB malonic acids, in the bottom and middle spectra, respectively. The coloration of the bottom two plots matches that of Figure 7.4., where the spectral contribution of the carbonyl taking part in the internal H-bond is colored maroon, and the other carbonyl bond response is colored yellow. The color-coded graphic of the molecule for both internal bonding conformations has been reproduced next to the corresponding spectra for reference. For the IUB malonic

acids, the coloring is more arbitrarily assigned because of the interchangeability of the two carbonyl C=O bonds.

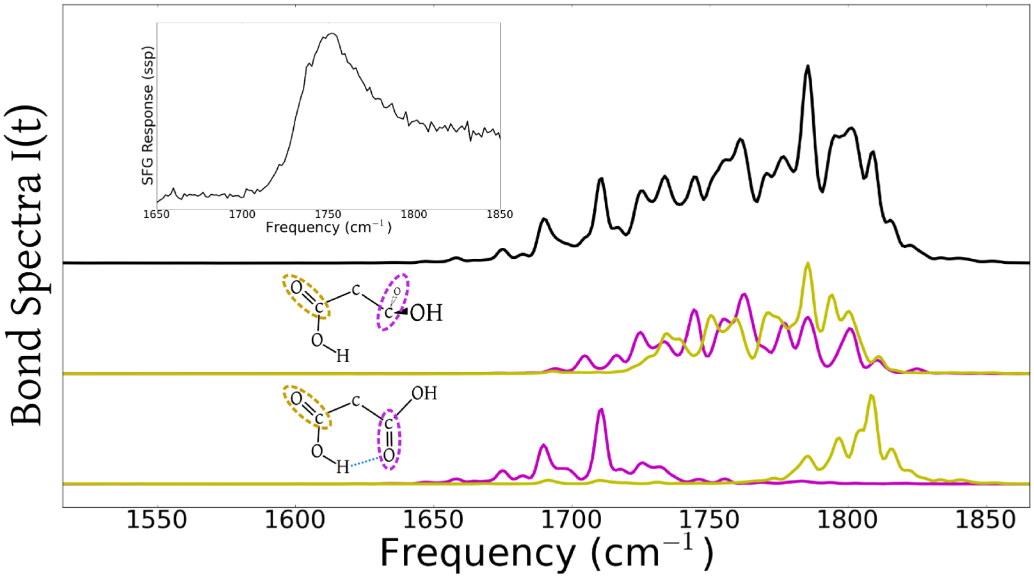

FIGURE 7.9. Vibrational power spectra of the carbonyl C=O bond trajectories with (inset) experimental results.

The top spectrum of Figure 7.9. spans approximately 130 $cm^{-1}$, with a maximum located towards the upper frequencies near 1800 $cm^{-1}$. The width of the spectrum suggests a large distribution of solvation environments in which the carbonyl bonds are interacting with surface waters. In our previous SFG spectroscopic experiments, the response of surface malonic acid molecules was determined to lie within the same spectral range, with a peak centered at 1745 $cm^{-1}$. The experimental results are very well reproduced in these bond spectra calculations, increasing confidence in the computational method employed for the simulations, and also the consequent model developed for the orientation and other behaviors of the acid molecules.

To further emphasize the differences between the IHB and IUB configurations of malonic acid, the bottom two spectra of Figure 7.9. show the contributions from each of the two sets of simulations. The IUB acids have the two ends of the molecule acting more independently than would be the case if there had been an internal bond. The two carbonyls can thus both experience a full range of solvation environments. The spectral response of these two carbonyls are expected to be similar, or overlapped in frequencies. As shown in the middle spectrum of Figure 7.9., the two carbonyl spectra are mostly overlapped, and form the central contributions to the overall spectrum from the collection of all simulation datasets (top of Figure 7.9.). Looking to the bottom spectrum in Figure 7.9., there is a dramatic splitting of the two carbonyl peaks. The C=O bond involved in the IHB is red-shifted, and the other carbonyl is blue-shifted compared to the IUB spectra. This shift in frequencies shows the strong effect of an internal H-bond on both the bonded carbonyl, and the outer uninvolved carbonyl bond.

In this study, the statistical distribution of the two internal bonding conformations could not be established because of the limited data collected and computational resources used. Thus, the intensities of the spectra can not be directly compared to experimental results, but the frequencies themselves are representational of those for carbonyl bonds. Future studies employing larger data sets will further establish the spectral response of these surface-hydrated malonic acids. Furthermore, it will be possible to establish whether the IHB conformation is a statistically relevant species at aqueous surfaces. However, it is possible to conclude that the higher and lower frequency carbonyl responses arise from malonic acids with specific geometric conformations (e.g. internal bonding), or some other form of solvation that constrains the motions and interactions of the acid.

## 7.7. Summary

The adsorption of small organic and chemically active molecules has gained great interest in recent years. Understanding their reactivities, orientations, adsorption pathways, and surface behaviors is of primary concern in building accurate atmospheric climate models, and in defining the many aqueous environments found on earth. Yet, the specific microscopic nature of such organics, their surface geometries, orientations, and water interactions remain poorly understood. Although our comprehension of surface processes and interfacial chemistry is still in its infancy, we are beginning to gain new insights that are key to understanding environmentally important processes at aqueous surfaces.

Presented herein are results of KS-DFT MD simulations that focus on how malonic acid behaves on a water surface, and the resulting orientations, geometries, and structures formed because of its interactions with interfacial water molecules. This computational study complements and expands on experimental studies from this laboratory that elucidated the molecular behavior of malonic acid.[21] Furthermore, these computations build upon and enhance our understanding of malonic acid from the computational study on interfacial orientation and geometry of aqueous surface malonic acid molecules.

Our simulations show that the previously used classical interaction potential captures the orientation and hydration structure of the KS-DFT model. The complementary simulations studies using both interaction potentials show strong agreement for the surface-bound malonic acid behaviors. However, the classical model does not fully capture the resonance structures of the carboxylic acids, leading to minor discrepancies between the water structures that form to hydrate the acids.

Our analysis of intramolecular atomic distances resulted in the discovery of two dominant conformations of surface malonic acid: an intramolecularly hydrogen-bonded species, and an acid in which neither carboxylic acid end-group takes part in internal bonding. The hydrogen bonded structure forms a ring-like internal geometry due to the folding of one carboxylic acid end towards the other, and subsequent hydrogen-bonding. The internal H-bond is strong and persistent throughout 40 ps of simulation, and warrants further experimental study to verify the existence of the species. The distribution of bondlengths in the surface malonic acid indicate that the two conformations of the acid have non-equivalent carboxylic acid moieties. In the hydrogen-bonded form, the bondlengths in one carboxylic acid end of the molecule differ from those at the other end. Delocalization of the atoms involved in the hydrogen bond causes elongation of the interacting bonds. The bondlengths and molecular geometry are accompanied with orientational and spectral changes brought on by the internal bonding of the molecule.

This chapter shows the results of an orientational analysis defining the overall molecular orientation of malonic acid on a water surface, and the configuration of the two carboxylic acids. The carbon backbone was found to lie slightly tilted from the plane of the interface. The hydrogen-bonded conformation has much more orientational freedom than its unbonded counterpart. Analysis of the dihedral angles of the carboxylic acids showed two distinct trends dependent on the specific molecular bonding conformation. The internally unbonded molecule's carboxylic acids orient very similarly to those found in our previous computational study, with one aligning perpendicular to the other. However, the internally H-bonded acid has a very defined internal orientation, with one carbonyl aligned anti-parallel to the other due to a rigid backbone structure reinforced by the intramolecular bonding.

The orientation of the carbonyl bonds was analyzed to complete the picture of the molecular orientation of surface malonic acid. Two distinct carbonyl C=O behaviors were found to be preferred, with one C=O bond pointing more in the plane of the water surface, and the other pointing more perpendicularly, in towards the water bulk. This result agrees well with our previous classical simulation results, and also complements the conclusions from our VSFS experiments showing two preferred net orientations of the carbonyl C=O modes. As with the other computational results, the H-bonded form has greater orientational freedom overall for the carbonyl C=O bonds.

Lastly, to compare the KS-DFT vibrational modes with experiment, the local mode bond spectra were calculated for the carbonyl C=O bonds. The frequencies and spectral shape agree with what we found experimentally via VSFS of the surface-bound C=O modes. The frequency response of the carbonyl calculated here is not a spectroscopic signal computation; it is not directly comparable to the experimental SFG spectral modes. However, the computed local-mode frequencies reinforce the predictions of our simulations. Additionally, the C=O spectra of the internally H-bonded conformation show a splitting of the two C=O modes because of the drastically different environments surrounding each bond.

These studies build upon our computational and experimental research in this area, seeking to understand how small organic molecules behave while bound to, and reacting with an aqueous/air interface. Such knowledge is our key to understanding atmospheric aerosol and land water systems where small and reactive organic acid molecules bind to aqueous surfaces, and form platforms for further chemical reactions. Further studies of these systems will aid us in better understanding water surfaces where molecular behavior can surprise us, and often defies our physical intuitions.

## CHAPTER VIII

## CONCLUSIONS

This dissertation is a collection of scientific explorations that help to better understand, and reaffirm the importance of interfacial aqueous environments. Unlike bulk water solutions, the surface and phase boundaries with other systems are environments characterized by a break in isotropy leading to unique electric fields, molecular layering, orientations, and resultant chemical reactions. The water surface is vital to life processes within living cells, and an endless number of reactions that define our Earth's environmnets and atmosphere. The aqueous interface is the gateway to chemical adsorption into water, and a platform for the chemistry that defines out world.

Experiments to probe air-water and liquid-liquid interfaces have revealed many of the macroscopic properties of those systems; they have also made some important advances towards understanding the microscopic nature of the chemicals leading to those results. However, many properties of water systems remain inaccessible to experiment, but are studied in a straightforward manner via computational MD simulations. MD allows the researcher to examine the specific geometries and energies of molecular systems as they evolve over time. This technique complements experimental work, and also expands the possibilities of properties to be studied.

This dissertation applies many computational analysis techniques in pursuit of understanding the behaviors of water and various solutes throughout an aqueous interface. Many of the studies made use of orientational analysis to describe the change to molecular orientation as a function of depth in the interface. Similarly, density profiling was used to establish the surface affinity of constituent molecules, and their location preferences within a water surface.

Bondlength trajectories and distributions provide a direction examination of how molecular, or specific functional moiety geometries change over time. These structural changes can be stimulated by solvation from neighboring waters, or by the interactions with other solutes. Furthermore, bondlength trajectories are used to define acid protonation states, hydrogen bond strength and lifetimes, and other properties that can be examined by looking at inter-atomic distances, such as the coordination state of a hydrated molecule.

A technique used in some of the projects reported herein is the calculation of spectral response from MD simulation data. The vibrational frequency response of a local mode (e.g. a covalent bond) provides data that can be directly compared to experimental results from spectroscopic studies. Furthermore, the calculation of VSFS response from MD data forms a link to the surface-specific spectroscopic experiments taking place in the Richmond laboratory. This computational technique complements and validates the experimental conclusions, and expands on them with new insights that are impossible or difficult to obtain using traditional spectroscopic experiments.

Molecular dynamics studies have increased in number, scope, and complexity since the early days of simple ideal gas calculations. It is rare to find a research effort in chemistry that is not making use of computational simulations. The importance of MD comes from its ability to confirm what we find in the laboratory and also the potential to save time and physical resources from expensive and complicated experiments, and in the predictive power of calculations. The MD simulations described in this dissertation expanded upon and validated a number of experiments on small environmentally relevant, interfacially active molecules. These few simulation studies help us to better understand the nature of water surfaces, and the interesting behaviors that take place within them.

# APPENDIX

# HETERODYNE DETECTED SFG

Recent developments in vibrational sum frequency generation (VSFG) spectroscopy have enabled researchers to experimentally determine both real and imaginary contributions to the second-order nonlinear susceptibility, $\chi^{(2)}$. Heterodyne-detected VSFG (HD-VSFG) experiments provide both the phase and sign of $\chi^{(2)}$, which are subsequently used to unambiguously determine the direction of a dipole transition with respect to an experimental geometry. This experimental method was first presented by Shen and coworkers.[210–214] Many recent experimental and computational studies employed HD-VSFG to probe the structure of the air/water interface, confirming or helping to rethink many conclusions from conventional SFG studies, while also allowing for a direct comparison with MD predictions based on calculating the components of $\chi^{(2)}$.[89, 215–221]

Conventional VSFG is a coherent optical process where the signal intensity decreases quadratically with dilution or number density of the modes being probed. The spectra are thus often overwhelmed by a contribution from the non-resonant background. HD-VSFG overcomes the issues of SFG by making use of an interference of the SFG signal with an experimental reference beam. This interference process amplifies the SFG intensity, and provides higher overall sensitivity with a much improved signal-to-noise ratio. This has been shown to work well on sub-monolayer surface coverage, and without the use of surface enhancement phenomena, using only the electronic resonances probed.[216] Additionally, the response of HD-VSFG is linear with the number density of the probed modes. The direct benefit of employing HD-VSFG is that the resonant signal and non-resonant background are separated, and both amplitude and phase responses are captured for direct assignment of directionality of the various modes in a system.

Molecular dynamics studies have been performed to recreate $\chi^{(2)}$ for a number of water interfaces, as was done in Chapter III of this dissertation.[215, 217, 219–221] In one case many of the same ions in Chapter III were introduced to a water-air interfacial system and the imaginary part of $\chi^{(2)}$, Im[$\chi^{(2)}$], was presented along with the conventional SFG response.[218] Interestingly, the study confirmed the conclusions regarding the locations of the anions throughout the interface as relates to their size, charge, and polarizability, but went further to examine the flipping of the electric field as a result of cation surface propensity. Another HD-VSFG study confirmed that the surface of a water region does not show ice-like behavior in the water bonding interactions.[215]

In regards to the current dissertation, the work of Chapter III represents a modest attempt to link the MD simulations performed using a rigid and polarizable water model, POL3, to the conventional SFG experiments of similar systems. Before the adoption of HD-VSFG, calculation of Im[$\chi^{(2)}$] would have predicted the phase of various modes in the water vibrational spectra, but would not have a direct means for comparison to experiment. Because the Richmond lab has not yet employed phase sensitive techniques the original spectra presented for the water-oil region did not explicitly show the phase response or imaginary components. Current MD studies, however, now have a more powerful and directly comparable experimental mechanism, and the several studies cited above have made use of this ability.

An additional factor regarding the computed SFG response in this dissertation is the water model used for simulations. The POL3 model used is a rigid point charge model that makes use of fluctuating charges dependent on computed local fields to simulate molecular polarizabilities. Newer water models developed specifically for calculating SFG response are better suited for the computations, and show quantitative agreement with the spectra obtained experimentally. These models include the Morita-Ishiyama water model,[68, 69, 219, 220] and a new model that includes a three-body interaction potential that accounts for a nearly 20% difference in the potential term as compared to the analogous pair-wise potential.[215, 222] The water model developed by Marti et al. was used in a successful study of the SFG response from waters hydrating a lipid, and also subsequent analysis using a truncated response function to decouple the auto- and cross-correlation parts of the $\chi^{(2)}$ spectrum.[221, 223, 224] These new models accurately reproduce the sign and phase, as well and the overall frequency response of the SFG spectra, while maintaining the accurate intermolecular interaction geometries with other water molecules, and the various solutes introduced to the water surface.

Due to time and computational restraints the real and imaginary components of $\chi^{(2)}$ were not presented in this dissertation for the water systems documented in Chapter III. Future studies by the Richmond group may calculate the components of $\chi^{(2)}$ (i.e. modeling heterodyne-detected SFG response) to better relate the orientational and electric field phenomena that take place at water's surface, and couple with future HD-VSFG experiments for further confirmation. Application of this new and exciting computational method, and comparison with experiment, will doubtlessly change the way surface studies are performed, and will lead to more direct confirmation of molecular behaviors at aqueous surfaces.

# REFERENCES CITED

[1] C. L. McFearin and G. L. Richmond. The role of interfacial molecular structure in the adsorption of ions at the liquid-liquid interface. *Journal of Physical Chemistry C*, 113(50):21162–21168, DEC 17 2009. ISSN 1932-7447. doi: 10.1021/jp906616c.

[2] D. Sholl and J.A. Steckel. *Density Functional Theory: A Practical Introduction*. John Wiley & Sons, 2011. ISBN 9781118211045. URL `http://books.google.com/books?id=_f994dmAdv0C`.

[3] D. Frenkel and B. Smit. *Understanding molecular simulation: from algorithms to applications*. Computational science. Academic Press, 2002. ISBN 9780122673511. URL `http://books.google.com/books?id=XmyO2oRUg0cC`.

[4] E.G. Lewars. *Computational Chemistry: Introduction to the Theory and Applications of Molecular and Quantum Mechanics*. Springer, 2011. ISBN 9789048138609. URL `http://books.google.com/books?id=zwDCWvnbrQwC`.

[5] D. Marx and J. Hutter. *Ab initio molecular dynamics: basic theory and advanced methods*. Cambridge University Press, 2009. ISBN 9780521898638. URL `http://books.google.com/books?id=1Ijmiw_EchIC`.

[6] P. Nielaba, M. Mareschal, and G. Ciccotti. *Bridging time scales: molecular simulations for the next decade*. Lecture notes in physics. Springer, 2002. ISBN 9783540443179. URL `http://books.google.com/books?id=d4YROr5SNY4C`.

[7] D. C. Rapaport. *The Art of Molecular Dynamics Simulation*. Cambridge University Press, Cambridge, 1995.

[8] D. C. Rapaport. An introduction to interactive molecular-dynamics simulations. *Computers in Physics*, 11(4):337–347, 1997.

[9] A. Satoh. *Introduction to Practice of Molecular Simulation: Molecular Dynamics, Monte Carlo, Brownian Dynamics, Lattice Boltzmann and Dissipative Particle Dynamics*. Elsevier Insights. Elsevier, 2010. ISBN 9780123851482. URL `http://books.google.com/books?id=nx6_aH-JRWwC`.

[10] D. A. Case, T. E. Cheatham, T. Darden, H. Gohlke, R. Luo, K. M. Merz, A. Onufriev, C. Simmerling, B. Wang, and R. J. Woods. The amber biomolecular simulation programs. *Journal of Computational Chemistry*, 26 (16):1668–1688, December 2005. doi: 10.1002/jcc.20290.

[11] Case, T.A. Darden, T.E. Cheatham III, C.L. Simmerling, J. Wang, R.E. Duke, R. Luo, R.C. Walker, W. Zhang, K.M. Merz, B. Roberts, B. Wang, S. Hayik, A. Roitberg, G. Seabra, I. Kolossvry, K.F. Wong, F. Paesani, J. Vanicek, J. Liu, X. Wu, S.R. Brozell, T. Steinbrecher, H. Gohlke, Q. Cai, X. Ye, J. Wang, M.-J. Hsieh, G. Cui, D.R. Roe, D.H. Mathews, M.G. Seetin, C. Sagui, V. Babin, T. Luchko, S. Gusarov, A. Kovalenko, , and P.A. Kollman. *Amber 11*. University of California, San Francisco., 2010.

[12] CP2K. http://cp2k.berlios.de, 2007.

[13] J. VandeVondele, M. Krack, F. Mohamed, M. Parrinello, T. Chassaing, and J. Hutter. Quickstep: Fast and accurate density functional calculations using a mixed gaussian and plane waves approach. *Computer Physics Communications*, 167(2):103–128, April 2005. URL `http://cp2k.berlios.de`.

[14] E. S. Shamay, V. Buch, M. Parrinello, and G. L. Richmond. At the water's edge: Nitric acid as a weak acid. *Journal Of The American Chemical Society*, 129 (43):12910–+, October 2007.

[15] E. S. Shamay and G. L. Richmond. Ionic disruption of the liquid-liquid interface. *Journal of Physical Chemistry C*, 114(29):12590–12597, JUL 29 2010. ISSN 1932-7447. doi: 10.1021/jp1023668.

[16] T. L. Tarbuck and G. L. Richmond. SO2 : H2O surface complex found at the vapor/water interface. *Journal Of The American Chemical Society*, 127(48): 16806–16807, DEC 7 2005. ISSN 0002-7863.

[17] T. L. Tarbuck and G. L. Richmond. Adsorption and reaction of CO2 and SO2 at a water surface. *Journal Of The American Chemical Society*, 128(10): 3256–3267, MAR 15 2006. ISSN 0002-7863. doi: 10.1021/ja057375a.

[18] S. T. Ota and G. L. Richmond. Chilling out: A cool aqueous environment promotes the formation of gas-surface complexes. *Journal of the American Chemical Society*, 133(19):7497–7508, 2011. doi: 10.1021/ja201027k.

[19] E. S. Shamay, K. E. Johnson, and G. L. Richmond. Dancing on water: The choreography of sulfur dioxide adsorption to aqueous surfaces. *Journal of Physical Chemistry C*, 115:25304–25314, November 2011. doi: 10.1021/jp2064326.

[20] E. S. Shamay and G. L. Richmond. Staying hydrated: The molecular journey of gaseous sulfur dioxide to a water surface. *Under revision*, 2012.

[21] P. Blower, E. S. Shamay, S. T. Ota, and G. L. Richmond. Malonic acid behavior on a water surface: a combined experimental and md approach. *Manuscript in preparation*, 2012.

[22] E. S. Shamay and G. L. Richmond. Ab initio molecular dynamics study of malonic on a water surface. *Manuscript in preparation*, 2012.

[23] E. R. Gibson, P. K. Hudson, and V. H. Grassian. Physicochemical properties of nitrate aerosols: Implications for the atmosphere. *Journal Of Physical Chemistry A*, 110(42):11785–11799, October 2006.

[24] A. M. Rivera-Figueroa, A. L. Sumner, and B. J. Finlayson-Pitts. Laboratory studies of potential mechanisms of renoxification of tropospheric nitric acid. *Environmental Science & Technology*, 37(3):548–554, February 2003.

[25] Jennie L Thomas, Martina Roeselova, L. X. Dang, and Douglas J. Tobias. Molecular dynamics simulations of the solution - air interface of aqueous sodium nitrate. *Journal of Physical Chemistry A*, 111(16):3091–3098, 2007. ISSN 1089-5639.

[26] R. Bianco, S. Z. Wang, and J. T. Hynes. Theoretical study of the dissociation of nitric acid at a model aqueous surface. *Journal Of Physical Chemistry A*, 111 (43):11033–11042, November 2007.

[27] C. Schnitzer, S. Baldelli, D. J. Campbell, and M. J. Shultz. Sum frequency generation of o-h vibrations on the surface of h2o/hno3 solutions and liquid hno3. *Journal Of Physical Chemistry A*, 103(32):6383–6386, August 1999.

[28] H. S. Yang and B. J. Finlayson-Pitts. Infrared spectroscopic studies of binary solutions of nitric acid and water and ternary solutions of nitric acid, sulfuric acid, and water at room temperature: Evidence for molecular nitric acid at the surface. *Journal Of Physical Chemistry A*, 105(10):1890–1896, March 2001.

[29] B. J. Finlayson-Pitts, L. M. Wingen, A. L. Sumner, D. Syomin, and K. A. Ramazan. The heterogeneous hydrolysis of no2 in laboratory systems and in outdoor and indoor atmospheres: An integrated mechanism. *Physical Chemistry Chemical Physics*, 5(2):223–242, 2003.

[30] Y. Dubowski, A. L. Sumner, E. J. Menke, D. J. Gaspar, J. T. Newberg, R. C. Hoffman, R. M. Penner, J. C. Hemminger, and B. J. Finlayson-Pitts. Interactions of gaseous nitric acid with surfaces of environmental interest. *Physical Chemistry Chemical Physics*, 6(14):3879–3888, July 2004.

[31] K. A. Ramazan, L. M. Wingen, Y. Miller, G. M. Chaban, R. B. Gerber, S. S. Xantheas, and B. J. Finlayson-Pitts. New experimental and theoretical approach to the heterogeneous hydrolysis of no2: Key role of molecular nitric acid and its complexes. *Journal Of Physical Chemistry A*, 110(21):6886–6897, June 2006.

[32] M. C. K. Soule, P. G. Blower, and G. L. Richmond. Nonlinear vibrational spectroscopic studies of the adsorption and speciation of nitric acid at the vapor/acid solution interface. *Journal of Physical Chemistry A*, 111(17): 3349–3357, 2007.

[33] S. Goedecker, M. Teter, and J. Hutter. Separable dual-space gaussian pseudopotentials. *Physical Review B*, 54(3):1703–1710, July 1996.

[34] C. T. Lee, W. T. Yang, and R. G. Parr. Development of the colle-salvetti correlation-energy formula into a functional of the electron-density. *Physical Review B*, 37(2):785–789, January 1988.

[35] M. D. Elola, E. J. Marceca, D. Laria, and D. A. Estrin. Computer simulation study of hno3 dissociation in aqueous clusters. *Chemical Physics Letters*, 326 (5-6):509–514, August 2000.

[36] J. P. Devlin, N. Uras, J. Sadlej, and V. Buch. Discrete stages in the solvation and ionization of hydrogen chloride adsorbed on ice particles. *Nature*, 417 (6886):269–271, May 2002.

[37] R. Bianco and J. T. Hynes. A theoretical study of the h2so4+h2o -¿ hso4-+h3o+ reaction at the surface of aqueous aerosols. *Theoretical Chemistry Accounts*, 111(2-6):182–187, March 2004.

[38] Kevin Charreteur, Francois Quentel, Catherine Elleouet, and Maurice L'Her. Transfer of highly hydrophilic ions from water to nitrobenzene, studied by three-phase and thin-film modified electrodes. *Analytical Chemistry*, 80(13): 5065–5070, JUL 1 2008. ISSN 0003-2700. doi: 10.1021/ac800204u.

[39] Xin Chen, Tinglu Yang, Sho Kataoka, and Paul S. Cremer. Specific ion effects on interfacial water structure near macromolecules. *Journal of the American Chemical Society*, 129(40):12272–12279, OCT 10 2007. ISSN 0002-7863. doi: 10.1021/ja07386gr.

[40] GM Luo, S Malkova, J Yoon, DG Schultz, BH Lin, M Meron, I Benjamin, P Vanysek, and ML Schlossman. Ion distributions near a liquid-liquid interface. *Science*, 311(5758):216–218, JAN 13 2006. ISSN 0036-8075. doi: 10.1126/science.1120392.

[41] B. Schnell, R. Schurhammer, and G. Wipff. Distribution of hydrophobic ions and their counterions at an aqueous liquid-liquid interface: A molecular dynamics investigation. *Journal of Physical Chemistry B*, 108(7):2285–2294, FEB 19 2004. ISSN 1520-6106. doi: 10.1021/jp036896m.

[42] KE Wardle, DJ Henderson, and RL Rowley. Molecular dynamics simulation of surfactant effects on ion transport through a liquid-liquid interface between partially miscible liquids. *Fluid Phase Equilibria*, 233(1):96–102, JUN 15 2005. ISSN 0378-3812. doi: 10.1016/j.fluid.2005.03.033.

[43] C. D. Wick and L. X. Dang. Recent advances in understanding transfer ions across aqueous interfaces. *Chemical Physics Letters*, 458(1-3):1–5, JUN 6 2008. ISSN 0009-2614. doi: 10.1016/j.cplett.2008.03.097.

[44] D. K. Hore, D. S. Walker, L. MacKinnon, and G. L. Richmond. Molecular structure of the chloroform - water and dichloromethane - water interfaces. *Journal of Physical Chemistry C*, 111(25):8832–8842, JUN 28 2007. ISSN 1932-7447. doi: 10.1021/jp067176t.

[45] D. K. Hore, D. S. Walker, and G. L. Richmond. Water at hydrophobic surfaces: When weaker is better. *Journal of the American Chemical Society*, 130(6): 1800+, FEB 13 2008. ISSN 0002-7863. doi: 10.1021/ja0755616S0002-7863(07)05561-8.

[46] D. K. Hore, D. S. Walker, and G. L. Richmond. Layered organic structure at the carbon tetrachloride-water interface. *Journal of the American Chemical Society*, 129(4):752–753, JAN 31 2007. ISSN 0002-7863. doi: 10.1021/ja067473b.

[47] D. S. Walker, D. K. Hore, and G. L. Richmond. Understanding the population, coordination, and orientation of water species contributing to the nonlinear optical spectroscopy of the vapor-water interface through molecular dynamics simulations. *Journal of Physical Chemistry B*, 110(41):20451–20459, OCT 19 2006. ISSN 1520-6106. doi: 10.1021/jp063063y.

[48] D. S. Walker and G. L. Richmond. Depth profiling of water molecules at the liquid-liquid interface using a combined surface vibrational spectroscopy and molecular dynamics approach. *Journal of the American Chemical Society*, 129 (30):9446–9451, AUG 1 2007. ISSN 0002-7863. doi: 10.1021/ja071740b.

[49] D. S. Walker, F. G. Moore, and G. L. Richmond. Vibrational sum frequency spectroscopy and molecular dynamics simulation of the carbon tetrachloride-water and 1,2-dichloroethane-water interfaces. *Journal of Physical Chemistry C*, 111(16):6103–6112, APR 26 2007. ISSN 1932-7447. doi: 10.1021/jp068700z.

[50] TM Chang, KA Peterson, and LX Dang. Molecular-dynamics simulations of liquid, interface, and ionic solvation of polarizable carbon-tetrachloride. *Journal of Chemical Physics*, 103(17):7502–7513, NOV 1 1995. ISSN 0021-9606.

[51] Becky L. Eggimann and J. Ilja Siepmann. Size effects on the solvation of anions at the aqueous liquid-vapor interface. *Journal of Physical Chemistry C*, 112(1): 210–218, JAN 10 2008. ISSN 1932-7447. doi: 10.1021/jp076054d.

[52] Hao Du, Jin Liu, Orhan Ozdemir, Anh V. Nguyen, and Jan D. Miller. Molecular features of the air/carbonate solution interface. *Journal of Colloid and Interface Science*, 318(2):271–277, FEB 15 2008. ISSN 0021-9797. doi: 10.1016/j.jcis.2007.09.097.

[53] CD Wick and LX Dang. Distribution, structure, and dynamics of cesium and iodide ions at the h2o-ccl4 and h2o-vapor interfaces. *Journal of Physical Chemistry B*, 110(13):6824–6831, APR 6 2006. ISSN 1520-6106. doi: 10.1021/jp055427c.

[54] PB Petersen, RJ Saykally, M Mucha, and P Jungwirth. Enhanced concentration of polarizable anions at the liquid water surface: Shg spectroscopy and md simulations of sodium thiocyanide. *Journal of Physical Chemistry B*, 109(21): 10915–10921, JUN 2 2005. ISSN 1520-6106. doi: 10.1021/jp050864c.

[55] M Matsumoto and Y Kataoka. Study on liquid vapor interface of water 1. simulational results of thermodynamic properties and orientational structure. *Journal of Chemical Physics*, 88(5):3233–3245, MAR 1 1988. ISSN 0021-9606.

[56] PB Petersen and RJ Saykally. On the nature of ions at the liquid water surface. *Annual Review of Physics Chemistry*, 57:333–364, 2006. ISSN 0066-426X. doi: 10.1146/annurev.physchem.57.032905.104609.

[57] Heather C. Allen, Nadia N. Casillas-Ituarte, M. Roxana Sierra-Hernandez, Xiangke Chen, and Cheng Y. Tang. Shedding light on water structure at air-aqueous interfaces: ions, lipids, and hydration. *Physical Chemistry Chemical Physics*, 11(27):5538–5549, 2009. ISSN 1463-9076. doi: 10.1039/b901209e.

[58] O Hofft, A Borodin, U Kahnert, V Kempter, LX Dang, and P Jungwirth. Surface segregation of dissolved salt ions. *Journal of Physical Chemistry B*, 110 (24):11971–11976, JUN 22 2006. ISSN 1520-6106. doi: 10.1021/jp061437h.

[59] JK Beattie, AM Djerdjev, GV Franks, and GG Warr. Dipolar anions are not preferentially attracted to the oil/water interface. *Journal of Physical Chemistry B*, 109(33):15675–15676, AUG 25 2005. ISSN 1520-6106. doi: 10.1021/jp0528941.

[60] Hong-tao Bian, Ran-ran Feng, Yuan Guo, and Hong-fei Wang. Specific na+ and k+ cation effects on the interfacial water molecules at the air/aqueous salt solution interfaces probed with nonresonant second harmonic generation. *Journal of Chemical Physics*, 130(13), APR 7 2009. ISSN 0021-9606. doi: 10.1063/1.3104609.

[61] LX Dang. Computational study of ion binding to the liquid interface of water. *Abstracts of Papers of the American Chemical Society*, 228(Part 2):86–PHYS, AUG 22 2004. ISSN 0065-7727.

[62] C. D. Wick, I-Feng W. Kuo, C. J. Mundy, and L. X. Dang. The effect of polarizability for understanding the molecular structure of aqueous interfaces. *Journal of Chemical Theory and Computation*, 3(6):2002–2010, NOV-DEC 2007. ISSN 1549-9618. doi: 10.1021/ct700098z.

[63] Y. B. Fan, X. Chen, L. J. Yang, P. S. Cremer, and Y. Q. Gao. On the structure of water at the aqueous/air interface. *Journal of Physical Chemistry B*, 113 (34):11672–11679, 2009. doi: 10.1021/jp900117t.

[64] N. Galamba and B. J. Costa Cabral. The changing hydrogen-bond network of water from the bulk to the surface of a cluster: A born-oppenheimer molecular dynamics study. *Journal of the American Chemical Society*, 130(52): 17955–17960, DEC 31 2008. ISSN 0002-7863. doi: 10.1021/ja807111y.

[65] T. Ishiyama and A. Morita. Molecular dynamics study of gas-liquid aqueous sodium halide interfaces. ii. analysis of vibrational sum frequency generation spectra. *Journal Of Physical Chemistry C*, 111(2):738–748, January 2007.

[66] A Morita and JT Hynes. A theoretical analysis of the sum frequency generation spectrum of the water surface. *Chemical Physics*, 258(2-3):371–390, AUG 15 2000. ISSN 0301-0104.

[67] D. S. Walker and G. L. Richmond. Interfacial depth profiling of the orientation and bonding of water molecules across liquid-liquid interfaces. *Journal of Physical Chemistry C*, 112(1):201–209, JAN 10 2008. ISSN 1932-7447. doi: 10.1021/jp075469w.

[68] A Morita and JT Hynes. A theoretical analysis of the sum frequency generation spectrum of the water surface. ii. time-dependent approach. *Journal of Physical Chemistry B*, 106(3):673–685, JAN 24 2002. ISSN 1520-6106. doi: 10.1021/jp0133438.

[69] Tatsuya Ishiyama and Akihiro Morita. Vibrational spectroscopic response of intermolecular orientational correlation at the water surface. *Journal of Physical Chemistry C*, 113(37):16299–16302, SEP 17 2009. ISSN 1932-7447. doi: 10.1021/jp9060957.

[70] TM Chang and LX Dang. Ion solvation in polarizable chloroform: A molecular dynamics study. *Journal of Physical Chemistry B*, 101(49):10518–10526, DEC 4 1997. ISSN 1089-5647.

[71] LX Dang. Computer simulation studies of ion transport across a liquid/liquid interface. *Journal of Physical Chemistry B*, 103(39):8195–8200, SEP 30 1999. ISSN 1089-5647.

[72] Tomas Hrobarik, Lubos Vrbka, and Pavel Jungwirth. Selected biologically relevant ions at the air/water interface: A comparative molecular dynamics study. *Biophysical Chemistry*, 124(3):238–242, DEC 1 2006. ISSN 0301-4622.

[73] J. W. Caldwell and P. A. Kollman. Structure and properties of neat liquids using nonadditive molecular-dynamics - water, methanol, and n-methylacetamide. *Journal of Physical Chemistry*, 99(16):6208–6219, April 1995. doi: 10.1021/j100016a067.

[74] Jose L. Rivera, Francis W. Starr, Patrice Paricaud, and Peter T. Cummings. Polarizable contributions to the surface tension of liquid water. *Journal of Chemical Physics*, 125(9), SEP 7 2006. ISSN 0021-9606. doi: 10.1063/1.2345063.

[75] PB Petersen and RJ Saykally. Adsorption of ions to the surface of dilute electroyte solutions: The jones-ray effect revisited. *Journal of the American Chemical Society*, 127(44):15446–15452, NOV 9 2005. ISSN 0002-7863.

[76] P. Salvador, J. E. Curtis, D. J. Tobias, and P. Jungwirth. Polarizability of the nitrate anion and its solvation at the air/water interface. *Physical Chemistry Chemical Physics*, 5(17):3752–3757, 2003.

[77] LX Dang. Importance of polarization effects in modeling the hydrogen bond in water using classical molecular dynamics techniques. *Journal of Physical Chemistry B*, 102(3):620–624, JAN 15 1998. ISSN 1089-5647.

[78] TM Chang and LX Dang. Molecular dynamics simulations of ccl4-h2o liquid-liquid interface with polarizable potential models. *Journal of Chemical Physics*, 104(17):6772–6783, MAY 1 1996. ISSN 0021-9606.

[79] CD Wick and LX Dang. Computational observation of enhanced solvation of the hydroxyl radical with increased nacl concentration. *Journal of Physical Chemistry B*, 110(18):8917–8920, MAY 11 2006. ISSN 1520-6106. doi: 10.1021/jp061221f.

[80] C. Wick and L. X. Dang. Molecular mechanism of transporting a polarizable iodide anion across the water-ccl4 liquid/liquid interface. *Journal of Chemical Physics*, 126(13):134702, APR 7 2007. ISSN 0021-9606. doi: 10.1063/1.2717164.

[81] P Jungwirth and DJ Tobias. Specific ion effects at the air/water interface. *Chemical Reviews*, 106(4):1259–1281, APR 2006. ISSN 0009-2665. doi: 10.1021/cr0403741.

[82] Y. Miller, J. L. Thomas, D. D. Kemp, B. J. Finlayson-Pitts, M. S. Gordon, D. J. Tobias, and R. B. Gerber. Structure of large nitrate-water clusters at ambient temperatures: Simulations with effective fragment potentials and force fields with implications for atmospheric chemistry. *Journal of Physical Chemistry A*, 113(46):12805–12814, NOV 19 2009. ISSN 1089-5639. doi: 10.1021/jp9070339.

[83] Dale E. Otten, Poul B. Petersen, and Richard J. Saykally. Observation of nitrate ions at the air/water interface by uv-second harmonic generation. *Chemical Physics Letters*, 449(4-6):261–265, DEC 5 2007. ISSN 0009-2614. doi: 10.1016/j.cplett.2007.10.081.

[84] C. Schnitzer, S. Baldelli, and MJ. Shultz. Sum frequency generation of water on nacl, nano3, khso4, hcl, hno3, and h2so4 aqueous solutions. *Journal of Physical Chemistry B*, 104(3):585–590, JAN 27 2000. ISSN 1089-5647.

[85] Man Xu, Cheng Y. Tang, Aaron M. Jubb, Xiangke Chen, and Heather C. Allen. Nitrate anions and ion pairing at the air-aqueous interface. *Journal of Physical Chemistry C*, 113(6):2082–2087, FEB 12 2009. ISSN 1932-7447. doi: 10.1021/jp805376x.

[86] Matthew A. Brown, Bernd Winter, Manfred Faubel, and John C. Hemminger. Spatial distribution of nitrate and nitrite anions at the liquid/vapor interface of aqueous solutions. *Journal of the American Chemical Society*, 131(24):8354, JUN 24 2009. ISSN 0002-7863. doi: 10.1021/ja901791v.

[87] S Gopalakrishnan, P Jungwirth, DJ Tobias, and HC Allen. Air-liquid interfaces of aqueous solutions containing ammonium and sulfate: Spectroscopic and molecular dynamics studies. *Journal of Physical Chemistry B*, 109(18): 8861–8872, MAY 12 2005. ISSN 1520-6106. doi: 10.1021/jp0500236.

[88] L. F. Scatena and G. L. Richmond. Orientation, hydrogen bonding, and penetration of water at the organic/water interface. *Journal of Physical Chemistry B*, 105(45):11240–11250, NOV 15 2001. ISSN 1089-5647. doi: 10.1021/jp0132174.

[89] Satoshi Nihonyanagi, Shoichi Yamaguchi, and Tahei Tahara. Direct evidence for orientational flip-flop of water molecules at charged interfaces: A heterodyne-detected vibrational sum frequency generation study. *Journal of Chemical Physics*, 130(20), MAY 28 2009. ISSN 0021-9606. doi: 10.1063/1.3135147.

[90] Alex G. Lambert, Paul B. Davies, and D. J. Neivandt. Implementing the theory of sum frequency generation vibrational spectroscopy: A tutorial review. *Applied Spectroscopy Reviews*, 40:103–145, 2005.

[91] D. J. Donaldson, J. A. Guest, and M. C. Goh. Evidence for adsorbed so2 at the aqueous air interface. *Journal of Physical Chemistry*, 99(23):9313–9315, June 1995. doi: 10.1021/j100023a002.

[92] V. Lattanzi, P. Thaddeus, M. C. McCarthy, and S. Thorwirth. Laboratory detection of protonated so2 in two isomeric forms. *Journal of Chemical Physics*, 133(19), 2010. doi: 10.1063/1.3491510.

[93] P. S. Shah, T. Balkhair, and Knowledge Synth Grp Determinants P. Air pollution and birth outcomes: A systematic review. *Environment International*, 37(2):498–516, 2011. doi: 10.1016/j.envint.2010.10.009.

[94] L. Tzivian. Outdoor air pollution and asthma in children. *Journal of Asthma*, 48(5):470–481, 2011. doi: 10.3109/02770903.2011.570407.

[95] D. O. Johns and W. S. Linn. A review of controlled human so2 exposure studies contributing to the us epa integrated science assessment for sulfur oxides. *Inhalation Toxicology*, 23(1):33–43, 2011. doi: 10.3109/08958378.2010.539290.

[96] I. Faloona. Sulfur processing in the marine atmospheric boundary layer: A review and critical assessment of modeling uncertainties. *Atmospheric Environment*, 43(18):2841–2854, 2009. doi: 10.1016/j.atmosenv.2009.02.043.

[97] T. Jurkat, C. Voigt, F. Arnold, H. Schlager, H. Aufmhoff, J. Schmale, J. Schneider, M. Lichtenstern, and A. Dornbrack. Airborne stratospheric itcims measurements of so2, hcl, and hno3 in the aged plume of volcano kasatochi. *Journal of Geophysical Research-atmospheres*, 115, 2010. doi: 10.1029/2010JD013890.

[98] C. M. Wu, J. Baltrusaitis, E. G. Gillan, and V. H. Grassian. Sulfur dioxide adsorption on zno nanoparticles and nanorods. *Journal of Physical Chemistry C*, 115(20):10164–10172, 2011. doi: 10.1021/jp201986j.

[99] J. T. Jayne, P. D.ovits, D. R. Worsnop, M. S. Zahniser, and C. E. Kolb. Uptake of so2(g) by aqueous surfaces as a function of ph - the effect of chemical-reaction at the interface. *Journal of Physical Chemistry*, 94(15):6041–6048, 1990.

[100] J. T. Jayne, J. A. Gardner, P. D.ovits, D. R. Worsnop, M. S. Zahniser, and C. E. Kolb. The effect of h2o2 content on the uptake of so2(g) by aqueous droplets. *Journal of Geophysical Research-atmospheres*, 95(D12):20559–20563, November 1990. doi: 10.1029/JD095iD12p20559.

[101] H. S. Yang, N. J. Wright, A. M. Gagnon, R. B. Gerber, and B. J. Finlayson-Pitts. An upper limit to the concentration of an so2 complex at the air water interface at 298 k: infrared experiments and ab initio calculations. *Physical Chemistry Chemical Physics*, 4(10):1832–1838, 2002. doi: 10.1039/b108907b.

[102] J. Baltrusaitis, P. M. Jayaweera, and V. H. Grassian. Sulfur dioxide adsorption on tio2 nanoparticles: Influence of particle size, coadsorbates, sample pretreatment, and light on surface speciation and surface coverage. *Journal of Physical Chemistry C*, 115(2):492–500, 2011. doi: 10.1021/jp108759b.

[103] G. Rubasinghege, S. Elzey, J. Baltrusaitis, P. M. Jayaweera, and V. H. Grassian. Reactions on atmospheric dust particles: Surface photochemistry and size-dependent nanoscale redox chemistry. *Journal of Physical Chemistry Letters*, 1(11):1729–1737, 2010. doi: 10.1021/jz100371d.

[104] L. Li, Z. M. Chen, Y. H. Zhang, T. Zhu, S. Li, H. J. Li, L. H. Zhu, and B. Y. Xu. Heterogeneous oxidation of sulfur dioxide by ozone on the surface of sodium chloride and its mixtures with other components. *Journal of Geophysical Research-atmospheres*, 112(D18), 2007. doi: 10.1029/2006JD008207.

[105] M. S. Madsen, A. Gross, H. Falsig, J. Kongsted, A. Osted, K. V. Mikkelsen, and O. Christiansen. Determination of rate constants for the uptake process involving so2 and an aerosol particle. a quantum mechanics/molecular mechanics and quantum statistical investigation. *Chemical Physics*, 348(1-3): 21–30, 2008. doi: 10.1016/j.chemphys.2008.02.008.

[106] J. Boniface, Q. Shi, Y. Q. Li, J. L. Cheung, O. V. Rattigan, P. D.ovits, D. R. Worsnop, J. T. Jayne, and C. E. Kolb. Uptake of gas-phase so2, h2s, and co2 by aqueous solutions. *Journal of Physical Chemistry A*, 104(32):7502–7510, 2000.

[107] Marcel Baer, C. J. Mundy, Tsun-Mei Chang, Fu-Ming Tao, and L. X. Dang. Interpreting vibrational sum-frequency spectra of sulfur dioxide at the air/water interface: A comprehensive molecular dynamics study. *Journal of Physical Chemistry B*, 114(21):7245–7249, JUN 3 2010. ISSN 1520-6106. doi: 10.1021/jp100310s.

[108] D. P. Lide, editor. *CRC Handbook of Chemistry and Physics.* CRC PRESS, 81 edition, 2000.

[109] B Isralewitz, J Baudry, J Gullingsrud, D Kosztin, and K Schulten. Steered molecular dynamics investigations of protein function. *Journal of Molecular Graphics & Modelling*, 19(1):13–25, 2001. ISSN 1093-3263.

[110] T. Giorgino and G. De Fabritiis. A high-throughput steered molecular dynamics study on the free energy profile of ion permeation through gramicidin a. *Journal of Chemical Theory and Computation*, 7(6):1943–1950, 2011. doi: 10.1021/ct100707s.

[111] A. R. Bizzarri. Steered molecular dynamics simulations of the electron transfer complex between azurin and cytochrome c(551). *Journal of Physical Chemistry B*, 115(5):1211–1219, 2011. doi: 10.1021/jp107933k.

[112] J. Strzelecki, K. Mikulska, M. Lekka, A. Kulik, A. Balter, and W. Nowak. Afm force spectroscopy and steered molecular dynamics simulation of protein contactin 4. *Acta Physica Polonica A*, 116:S156–S159, 2009.

[113] G. Patargias, H. Martay, and W. B. Fischer. Reconstructing potentials of mean force from short steered molecular dynamics simulations of vpu from hiv-1. *Journal of Biomolecular Structure & Dynamics*, 27(1):1–12, 2009.

[114] Z. W. Liu, Y. Xu, and P. Tang. Steered molecular dynamics simulations of na+ permeation across the gramicidin a channel. *Journal of Physical Chemistry B*, 110(25):12789–12795, 2006. doi: 10.1021/jp060688n.

[115] Janamejaya Chowdhary and Branka M. Ladanyi. Water-hydrocarbon interfaces: Effect of hydrocarbon branching on interfacial structure. *Journal of Physical Chemistry B*, 110(31):15442–15453, AUG 10 2006. ISSN 1520-6106. doi: 10.1021/jp060440y.

[116] L. X. Dang and T. M. Chang. Molecular dynamics study of water clusters, liquid, and liquid-vapor interface of water with many-body potentials. *Journal of Chemical Physics*, 106(19):8149–8159, 1997.

[117] William Humphrey, Andrew Dalke, and Klaus Schulten. VMD – Visual Molecular Dynamics. *Journal of Molecular Graphics*, 14:33–38, 1996.

[118] D. R. Worsnop, M. S. Zahniser, C. E. Kolb, J. A. Gardner, L. R. Watson, J. M. Vandoren, J. T. Jayne, and P. D.ovits. Temperature-dependence of mass accommodation of so2 and h2o2 on aqueous surfaces. *Journal of Physical Chemistry*, 93(3):1159–1172, 1989.

[119] Ulrich Heber and Katja Hueve. Action of so2 on plants and metabolic detoxification of so2. *International Review of Cytology*, pages 255–286, 1997.

[120] S. M. Clegg and J. P. D. Abbatt. Uptake of gas-phase so2 and h2o2 by ice surfaces: Dependence on partial pressure, temperature, and surface acidity. *Journal of Physical Chemistry A*, 105(27):6630–6636, 2001. doi: 10.1021/jp010062r.

[121] E. Bishenden and D. J. Donaldson. Ab initio study of so2+h2o. *Journal of Physical Chemistry A*, 102(24):4638–4642, June 1998. doi: 10.1021/jp980160l.

[122] Ralf Steudel and Yana Steudel. Sulfur dioxide and water: Structures and energies of the hydrated species so(2)center dot nh(2)o, [hso(3)](-)center dot nh(2)o, [so(3)h](-)center dot nh(2)o, and h(2)so(3)center dot nh(2)o (n=0-8). *European Journal of Inorganic Chemistry*, (10):1393–1405, April 2009. doi: 10.1002/ejic.200801158.

[123] V. Buch. Molecular structure and oh-stretch spectra of liquid water surface. *Journal of Physical Chemistry B*, 109(38):17771–17774, 2005. doi: 10.1021/jp052819a.

[124] Shinichi Hirabayashi, Fumiyuki Ito, and Koichi M. T. Yamada. Infrared spectra of the (h2o)(n)-so2 complexes in argon matrices. *Journal of Chemical Physics*, 125(3):034508, July 2006. doi: 10.1063/1.2214716.

[125] S Hayashi, M Oobatake, T Ooi, and K Machida. Molecular dynamics using internal coordinates .i. infrared spectra of sulfur dioxide. *Bulletin of the Chemical Society of Japan*, 58(4):1105–1108, 1985. ISSN 0009-2673.

[126] S. T. Moin, L. H. V. Lim, T. S. Hofer, B. R. Randolf, and B. M. Rode. Sulfur dioxide in water: Structure and dynamics studied by an ab initio quantum mechanical charge field molecular dynamics simulation. *Inorganic Chemistry*, 50(8):3379–3386, 2011. doi: 10.1021/ic102240p.

[127] B. Eckl, J. Vrabec, and H. Hasse. Set of molecular models based on quantum mechanical ab initio calculations and thermodynamic data. *Journal of Physical Chemistry B*, 112(40):12710–12721, 2008. doi: 10.1021/jp803341h.

[128] DJ Anick. Polyhedral water clusters, i: Formal consequences of the ice rules. *Journal of Molecular Structure-Theochem*, 587:87–96, JUL 5 2002. ISSN 0166-1280.

[129] Wolfgang Huber, Vincent J. Carey, Li Long, Seth Falcon, and Robert Gentleman. Graphs in molecular biology. *BMC Bioinformatics*, 8(Suppl. 6), 2007. ISSN 1471-2105. doi: 10.1186/1471-2105-8-S6-S8.

[130] TP Radhakrishnan and WC Herndon. Graph theoretical-analysis of water clusters. *Journal of Physical Chemistry*, 95(26):10609–10617, DEC 26 1991. ISSN 0022-3654.

[131] Q Shi, S Kais, and JS Francisco. Graph theory for fused cubic clusters of water dodecamer. *Journal of Physical Chemistry A*, 109(51):12036–12045, DEC 29 2005. ISSN 1089-5639. doi: 10.1021/jp0550154.

[132] G. C. Garcia, I. L. Ruiz, and M. A. Gomez-Nieto. Representation of the molecular topology of cyclical structures by means of cycle graphs. 1. extraction of topological properties. *Journal of Chemical Information and Computer Sciences*, 44(2):447–461, 2004. doi: 10.1021/ci034256a.

[133] S. McDonald, L. Ojamae, and S. J. Singer. Graph theoretical generation and analysis of hydrogen-bonded structures with applications to the neutral and protonated water cube and dodecahedral clusters. *Journal of Physical Chemistry A*, 102(17):2824–2832, 1998.

[134] W T Tutte. *Graph Theory, Encyclopedia of Mathematics and its Applications*, volume Vol. 21. Addison-Wesley, Menlo Park, CA, 1984.

[135] R. Balakrishnan and K. Ranganathan. *A textbook of graph theory*. Universitext (1979). Springer, New York, 2000. ISBN 9780387988597. URL `http://books.google.com/books?id=ERgLpQgQx4cC`.

[136] F. Harary and E.M. Palmer. *Graphical enumeration*. Academic Press, 1973. URL `http://books.google.com/books?id=yqr98zXOalcC`.

[137] L. Dury, T. Latour, L. Leherte, F. Barberis, and D. P. Vercauteren. A new graph descriptor for molecules containing cycles. application as screening criterion for searching molecular structures within large databases of organic compounds. *Journal of Chemical Information and Computer Sciences*, 41(6): 1437–1445, 2001.

[138] Donald E. Knuth. *Art of Computer Programming, Volume 1: Fundamental Algorithms (3rd Edition)*. Addison-Wesley Professional, 3 edition, July 1997. ISBN 0201896834. URL `http://www.worldcat.org/isbn/0201896834`.

[139] Thomas H. Cormen, Charles E. Leiserson, Ronald L. Rivest, and Clifford Stein. *Introduction to Algorithms*. MIT Press and McGraw-Hill, 2001.

[140] J Ellson, E R Gansner, E Koutsofios, S C North, and G Woodhull. Graphviz and dynagraph static and dynamic graph drawing tools. In *Graph Drawing Software*, pages 127–148. Springer-Verlag, 2004.

[141] Gansner and S C North. An open graph visualization system and its applications to software engineering. *Software - Practice and Experience*, (30): 1203–1233, 1999.

[142] M. Kanakidou, J. H. Seinfeld, S. N. Pandis, I. Barnes, F. J. Dentener, M. C. Facchini, R. Van Dingenen, B. Ervens, A. Nenes, C. J. Nielsen, E. Swietlicki, J. P. Putaud, Y. Balkanski, S. Fuzzi, J. Horth, G. K. Moortgat, R. Winterhalter, C. E. L. Myhre, K. Tsigaridis, E. Vignati, E. G. Stephanou, and J. Wilson. Oragnic aerosol and global climate modelling: a review. *Atmospheric Chemistry and Physics*, 5:1053–1123, 2005.

[143] J. H. Seinfeld and S. N. Pandis. *Atmospheric Chemistry and Physics*. Wiley-Interscience, New York, 1998.

[144] Barbara J. Finlayson-Pitts and Jr. James N. Pitts. *Chemistry of the Lower and Upper Atmosphere*. Academic Press, San Diego, 2000.

[145] A. Chebbi and P. Carlier. Carboxylic acids in the trospospphere, occurrence, sources, and sinks: A review. *Atmospheric Environment*, 30(24):4233–4249, 1996.

[146] C. L. Badger, I. George, P. T. Griffiths, C. F. Braban, R. A. Cox, and J. P. D. Abbatt. Phase transitions and hygroscopic growth of aerosol particles containing humic acid and mixtures of humic acid and ammonium sulphate. *Atmospheric Chemistry and Physics Discussions*, 5:9581–9620, 2005.

[147] Changgeng Peng, Man Nin Chan, and Chak K. Chan. The hygroscopic properties of dicarboxylic and multifunctional acids: Measurements and unifac predictions. *Environmental Science & Technology*, 35:4495–4501, 2001.

[148] Kimitaka Kawamura and Kouchi Usukura. Distributions of low molecular weight dicarboxylic acids in the north pacific aerosol samples. *Journal of Oceanography*, 49:271–283, 1993.

[149] Kimitaka Kawamura, Hideki Kasukabe, and Leonard A. Barrie. Source and reaction pathways of dicarboxylic acids, ketoacids and dicarbonyls in arctic aerosols: One year of observations. *Atmospheric Environment*, 30(10/11): 1709–1722, 1996.

[150] Kimitaka Kawamura and Futoshi Sakaguchi. Molecular distributions of water soluble dicarboxylic acids in marine aerosols over the pacific ocean including tropics. *Journal of Geophysical Research*, 104(D3):3501–3509, 1999.

[151] Richard Senpere and Kimitaka Kawamura. Comparative distributions of dicarboxylic acids and related polar compounds in snow, rain, and aerosols from urban atmosphere. *Atmospheric Environment*, 28(3):449–459, 1994.

[152] Richard Senpere and Kimitaka Kawamura. Low molecular weight dicarboxylic acids and related polar compounds in the remote marine rain samples collected from western pacific. *Atmospheric Environment*, 30(10/11):1609–1619, 1996.

[153] Shankar G. Aggarwal and Kimitaka Kawamura. Molecular distributions and stable carbon isotopic compositions of dicarboxylic acids and related compounds in aerosols from sapporo, japan: Implications for photochemical aging during long-range atmospheric transport. *Journal of Geophysical Research*, 113(D14301):13, 2008.

[154] Li-Ying Hsieh, Su-Ching Kuo, Chien-Lung Chen, and Ying I. Tsai. Size distributions of nano/micron dicarboxylic acids and inorganics ions in suburban pm episode and non-episodic aerosol. *Atmospheric Environment*, 43:4396–4406, 2009.

[155] Chandra Mouli Pavuluri, Kimitaka Kawamura, and T. Swaminathan. Water-soluble organic carbon, dicarboxylic acids, ketoacids, and -dicarbonyls in the tropical indian aerosols. *Journal of Geophysical Research*, 115(D11302):15, 2010.

[156] Celia N. Cruz and Spyros N. Pandis. A study of the ability of pure secondary organic aerosol to act as cloud condensation nuclei. *Atmospheric Environment*, 31(15):2205–2214, 1997.

[157] Matthew T. Parsons, Jackson Mak, Sarah R. Lipetz, and Allan K. Bertram. Deliquescence of malonic, succinic, glutaric, and adipic acid particles. *Journal of Geophysical Research*, 109(D06212):8, 2004.

[158] Christine F. Braban, Matthew F. Carroll, Sarah A. Styler, and Jonathan P. D. Abbatt. Phase transitions of malonic and oxalic acid aerosols. *Journal of Physical Chemistry A*, 107:6594–6602, 2003.

[159] Anne R. Hansen and Keith D. Beyer. Experimentally determined thermochemical properties of the malonic acid/water system: Implications for atmospheric aerosols. *Journal of Physical Chemistry A*, 108:3457–3466, 2004.

[160] Alastair Murray Booth, D. Owen Topping, Gordon McFiggans, and Carl John Percival. Surface tension of mixed inorganic and dicarboxylic acid aqueous solutions at 298.15 k and their importance for cloud activation predictions. *Physical Chemistry Chemical Physics*, 11:8021–8028, 2009.

[161] Antti-Pekka Hyvarinen, Heikki Lihavainen, Anca Gaman, Laura Vairila, Heikki Ojala, Markku Kulmala, and Yrja Viiasnen. Surface tensions and densities of oxalic, malonic, succinic, maleic, malic, and cis-pinonic acids. *Journal of Chemical and Engineering Data*, 51:255–260, 2006.

[162] Ilona Riipinen, Ismo K. Koponen, Gran P. Frank, Antti-Pekka Hyrinen, Joonas Vanhanen, Heikki Lihavainen, Kari E. J. Lehtinen, Merete Bilde, and Kulmala Markku. Adipic and malonic acid aqueous solutions: Surface tensions and saturation vapor pressures. *Journal of Physical Chemistry A*, 111:12995–13002, 2007.

[163] H. Giebl, A. Berner, G. Reischl, H. Puxbaum, A. Kasper-Giebl, and R. Hitzenberger. Ccn activation of oxalic and malonic acid test aerosols with the university of vienna cloud condensation nuclei counter. *Aerosol Science*, 33: 1623–1634, 2002.

[164] Barbara J. Finlayson-Pitts. Reactions at surfaces in the atmosphere: integration of experiments and theory as necessary (but not necessarily sufficient) for predicting the physical chemistry of aerosols. *Physical Chemistry Chemical Physics*, 11:7760–7779, 2009.

[165] Sayaka Hayase, Akihiro Yabushita, Masahiro Kawasaki, Shinichi Enami, Michael R. Hoffman, and Agustin J. Colussi. Weak acids enhance halogen activation on atmospheric water's surfaces. *Journal of Physical Chemistry A*, 115:4935–4940, 2011.

[166] C. D. Bain, P. B. Davies, T. H. Ong, R. N. Ward, and M. A. Brown. Quantitative-analysis of monolayer composition by sum-frequency vibrational spectroscopy. *Langmuir*, 7(8):1563–1566, August 1991. doi: 10.1021/la00056a003.

[167] M. C. K. Soule, P. G. Blower, and G. L. Richmond. Effects of atmospherically important solvated ions on organic acid adsorption at the surface of aqueous solutions. *Journal of Physical Chemistry B*, 111(49):13703–13713, 2007.

[168] J. T. Davies and E. K. Rideal. *Interfacial Phenomena*. Academic Press, New York, 2nd edition, 1963.

[169] D. A. Pearlman, D. A. Case, J. W. Caldwell, W. S. Ross, T. E. Cheatham, S. Debolt, D. Ferguson, G. Seibel, and P. Kollman. Amber, a package of computer-programs for applying molecular mechanics, normal-mode analysis, molecular-dynamics and free-energy calculations to simulate the structural and energetic properties of molecules. *Computer Physics Communications*, 91(1-3): 1–41, September 1995. doi: 10.1016/0010-4655(95)00041-D.

[170] L. Martinez, R. Andrade, E. G. Birgin, and J. M. Martinez. Packmol: A package for building initial configurations for molecular dynamics simulations. *Journal of Computational Chemistry*, 30(13):2157–2164, October 2009. doi: 10.1002/jcc.21224.

[171] S.E. Cabaniss, J.A. Leenheer, and I.F. McVey. Aqueous infrared carboxylate absorbances: aliphatic di-acids. *Spectrochimica Acta Part A*, 54:449–458, 1998.

[172] George Socrates. *Infrared Characteristic Group Frequencies*. Wiley Interscience, Chichester, 2nd edition, 1994.

[173] C. Magnus Johnson, Eric Tyrode, Steve Baldelli, Mark W. Rutland, and Christofer Leygraf. A vibrational sum frequency spectroscopy study of the liquid-gas interface of acetic acid-water mixtures: 1. surface speciation. *Journal of Physical Chemistry B*, 109:321–328, 2005.

[174] Eric Tyrode, C. Magnus Johnson, Steve Baldelli, Christofer Leygraf, and Mark W. Rutland. A vibrational sum frequency spectroscopy study of the liquid-gas interface of acetic acid-water mixtures: 2. orientation analysis. *Journal of Physical Chemistry B*, 109:329–341, 2005.

[175] *CRC Handbook of Chemistry and Physics*. CRC Press, Boca Raton, 85 edition, 2004.

[176] Ilse Wolfs and Herman O. Dessyn. Characteristic vibrational pattern for the cyclic dimer carboxylic acid function in the solid state. *Applied Spectroscopy*, 50(8):1000–1006, 1996.

[177] D. Bougeard, J. De Villepin, and A. Novak. Vibrational spectra and dynamics of crystalline malonic acid at room temperature. *Spectrochimica Acta*, 44A(12): 1281–1286, 1988.

[178] Suman Ghorai, Alexander Laskin, and Alexei V. Tivanski. Spectroscopic evidence of keto-enol tautomerism in deliquesced malonic acid particles. *Journal of Physical Chemistry A*, 115:4373–4380, 2011.

[179] T. H. Nguyen, D. E. Hibbs, and S. T. Howard. Conformations, energies, and intramolecular hydrogen bonds in dicarboxylic acids: Implications for the design of synthetic dicarboxylic acid receptors. *Journal of Computational Chemistry*, 26(12):1233–1241, September 2005. doi: 10.1002/jcc.20259.

[180] M. Merchan, F. Tomas, and I. Nebot-Gil. An ab initio study of intramolecular hydrogen bonding in malonic acid and its monoanion. *Journal of Molecular Structure (Theochem)*, 109:51–60, 1984.

[181] K. Kawamura, R. Semere, Y. Imai, Y. Fujii, and M. Hayashi. Water soluble dicarboxylic acids and related compounds in antarctic aerosols. *Journal of Geophysical Research-atmospheres*, 101(D13):18721–18728, August 1996. doi: 10.1029/96JD01541.

[182] Li-Ying Hsieh, Su-Ching Kuo, Chien-Lung Chen, and Ying I. Tsai. Origin of low-molecular-weight dicarboxylic acids and their concentration and size distribution variation in suburban aerosol. *Atmospheric Environment*, 41: 6648–6661, 2007.

[183] J. Nieminen, M. Rasanen, and J. Murto. Matrix-isolation and abinitio studies of oxalic-acid. *Journal of Physical Chemistry*, 96(13):5303–5308, June 1992. doi: 10.1021/j100192a024.

[184] Z. Nahalovsk, B Nahalovsk, and T. G. Strand. Molecular structure of gaseous oxalic acid from electron diffraction and ir data. *Acta Chemica Scandinavica*, 24(7):2617–&, 1970. doi: 10.3891/acta.chem.scand.24-2617.

[185] J. Dam, S. Harkema, and D. Feil. The electron-density of alpha-oxalic acid dihydrate at 100-k by x-ray-diffraction - a contribution to the iucr commission on charge, spin and momentum densities project on the accurate determination of electron-densities. *Acta Crystallographica Section B-structural Science*, 39 (DEC):760–768, 1983. doi: 10.1107/S0108768183003377.

[186] Sekh Mahiuddin, Babak Minofar, Jayanta M. Borah, Manash R. Das, and Pavel Jungwirth. Propensities of oxalic, citric, succinic, and maleic acids for the aqueous solution/vapour interface: Surface tension measurements and molecular dynamics simulations. *Chemical Physics Letters*, 462(4-6):217–221, September 2008. doi: 10.1016/j.cplett.2008.07.085.

[187] J. R. Odum, T. Hoffmann, F. Bowman, D. C.s, R. C. Flagan, and J. H. Seinfeld. Gas/particle partitioning and secondary organic aerosol yields. *Environmental Science & Technology*, 30(8):2580–2585, August 1996. doi: 10.1021/es950943+.

[188] J. R. Odum, T. P. W. Jungkamp, R. J. Griffin, R. C. Flagan, and J. H. Seinfeld. The atmospheric aerosol-forming potential of whole gasoline vapor. *Science*, 276(5309):96–99, April 1997. doi: 10.1126/science.276.5309.96.

[189] S. N. Pandis, S. E. Paulson, J. H. Seinfeld, and R. C. Flagan. Aerosol formation in the photooxidation of isoprene and beta-pinene. *Atmospheric Environment Part A-general Topics*, 25(5-6):997–1008, 1991. doi: 10.1016/0960-1686(91)90141-S.

[190] S. H. Zhang, M. Shaw, J. H. Seinfeld, and R. C. Flagan. Photochemical aerosol formation from alpha-pinene- and beta-pinene. *Journal of Geophysical Research-atmospheres*, 97(D18):20717–20729, December 1992.

[191] T. Hoffmann, J. R. Odum, F. Bowman, D. C.s, D. Klockow, R. C. Flagan, and J. H. Seinfeld. Formation of organic aerosols from the oxidation of biogenic hydrocarbons. *Journal of Atmospheric Chemistry*, 26(2):189–222, February 1997. doi: 10.1023/A:1005734301837.

[192] M. Hori, S. Ohta, N. Murao, and S. Yamagata. Activation capability of water soluble organic substances as ccn. *Journal of Aerosol Science*, 34(4):419–448, April 2003. doi: 10.1016/S0021-8502(02)00190-8.

[193] M. Bilde, B. Svenningsson, J. Monster, and T. Rosenorn. Even-odd alternation of evaporation rates and vapor pressures of c3-c9 dicarboxylic acid aerosols. *Environmental Science & Technology*, 37(7):1371–1378, April 2003. doi: 10.1021/es0201810.

[194] J. A. Nilsson, A. Laaksonen, and L. A. Eriksson. Solvation and conformational dynamics of dicarboxylic suberic acid. *Journal of Chemical Physics*, 109(6): 2403–2412, August 1998. doi: 10.1063/1.476808.

[195] Maria Darvas, Sylvain Picaud, and Pal Jedlovszky. Molecular dynamics simulation of the adsorption of oxalic acid on an ice surface. *Chemphyschem*, 11 (18):3971–3979, December 2010. doi: 10.1002/cphc.201000513.

[196] Maria Darvas, Sylvain Picaud, and Pal Jedlovszky. Water adsorption around oxalic acid aggregates: a molecular dynamics simulation of water nucleation on organic aerosols. *Physical Chemistry Chemical Physics*, 13(44):19830–19839, 2011. doi: 10.1039/c1cp21901d.

[197] M. Dlugosz and J. M. Antosiewicz. pk(a)s in dicarboxylic acids by constant-ph molecular dynamics simulations. *Zeitschrift Fur Naturforschung Section A-a Journal of Physical Sciences*, 59(11):873–874, November 2004.

[198] A. Mohajeri and N. Shakerin. The gas-phase acidity and intramolecular hydrogen bonding in oxalic acid. *Journal of Molecular Structure-theochem*, 711 (1-3):167–172, December 2004. doi: 10.1016/j.theochem.2004.10.002.

[199] M. P. C. M. Krijn and D. Feil. Electron-density distributions in hydrogen-bonds - a local density-functional study of alpha-oxalic acid dihydrate and comparison with experiment. *Journal of Chemical Physics*, 89(7): 4199–4208, October 1988. doi: 10.1063/1.454855.

[200] C. Chen and S. F. Shyu. Conformers and intramolecular hydrogen bonding of the oxalic acid monomer and its anions. *International Journal of Quantum Chemistry*, 76(4):541–551, 2000. doi: 10.1002/(SICI)1097-461X(2000)76:4¡541.

[201] Xiaofei Ma, Purnendu Chakraborty, Brian J. Henz, and Michael R. Zachariah. Molecular dynamic simulation of dicarboxylic acid coated aqueous aerosol: strucutre and processing of water vapor. *Physical Chemistry Chemical Physics*, 13:9374–9384, 2011.

[202] B. Zobrist, C. Marcolli, T. Koop, B. P. Luo, D. M. Murphy, U. Lohmann, A. A. Zardini, U. K. Krieger, T. Corti, D. J. Cziczo, S. Fueglistaler, P. K. Hudson, D. S. Thomson, and T. Peter. Oxalic acid as a heterogeneous ice nucleus in the upper troposphere and its indirect aerosol effect. *Atmospheric Chemistry and Physics*, 6:3115–3129, July 2006.

[203] N. C. Shantz, W. R. Leaitch, and P. F. Caffrey. Effect of organics of low solubility on the growth rate of cloud droplets. *Journal of Geophysical Research-atmospheres*, 108(D5):4168, March 2003. doi: 10.1029/2002JD002540.

[204] Hui Yan and Liang T. Chu. Interactions of oxalic acid and ice on cu surface. *Langmuir*, 24(17):9410–9420, September 2008. doi: 10.1021/la8008706.

[205] Przemyslaw Dopieralski, Charles L. Perrin, and Zdzislaw Latajka. On the intramolecular hydrogen bond in solution: Car-parrinello and path integral molecular dynamics perspective. *Journal of Chemical Theory and Computation*, 7(11):3505–3513, November 2011. doi: 10.1021/ct200580c.

[206] Lennart Eberson. Studies on succinic acids iv. evidence for the existence of intramolecular hydrogen bonding in certain highly alkylated succinic acids by infrared spectra. *Acta Chemica Scandinavica*, 13:224–235, 1959.

[207] E. M. S. Macoas, R. Fausto, M. Pettersson, L. Khriachtchev, and M. Rasanen. Infrared-induced rotamerization of oxalic acid monomer in argon matrix rid b-2989-2010. *Journal of Physical Chemistry A*, 104(30):6956–6961, August 2000. doi: 10.1021/jp000634s.

[208] E. M. S. Macoas, R. Fausto, J. Lundell, M. Pettersson, L. Khriachtchev, and M. Rasanen. Conformational analysis and near-infrared-induced rotamerization of malonic acid in an argon matrix rid b-2989-2010. *Journal of Physical Chemistry A*, 104(50):11725–11732, December 2000. doi: 10.1021/jp002853j.

[209] P. Tarakeshwar and S. Manogaran. Conformations and vibrations of dicarboxylic acids. an ab initio study rid b-6609-2008. *Theochem-journal of Molecular Structure*, 362(1):77–99, February 1996.

[210] N. Ji, V. Ostroverkhov, C. S. Tian, and Y. R. Shen. Characterization of vibrational resonances of water-vapor interfaces by phase-sensitive sum-frequency spectroscopy. *Physical Review Letters*, 100(9):096102, March 2008. doi: 10.1103/PhysRevLett.100.096102.

[211] Chuanshan Tian, Na Ji, Glenn A. Waychunas, and Y. Ron Shen. Interfacial structures of acidic and basic aqueous solutions. *Journal of the American Chemical Society*, 130(39):13033–13039, October 2008. doi: 10.1021/ja8021297.

[212] C. S. Tian and Y. R. Shen. Sum-frequency vibrational spectroscopic studies of water/vapor interfaces. *Chemical Physics Letters*, 470(1-3):1–6, February 2009. doi: 10.1016/j.cplett.2009.01.016.

[213] C. S. Tian and Y. R. Shen. Structure and charging of hydrophobic material/water interfaces studied by phase-sensitive sum-frequency vibrational spectroscopy. *Proceedings of the National Academy of Sciences of the United States of America*, 106(36):15148–15153, September 2009. doi: 10.1073/pnas.0901480106.

[214] Chuan-Shan Tian and Y. Ron Shen. Isotopic dilution study of the water/vapor interface by phase-sensitive sum-frequency vibrational spectroscopy. *Journal of the American Chemical Society*, 131(8):2790–+, March 2009. doi: 10.1021/ja809497y.

[215] Piotr A. Pieniazek, Craig J. Tainter, and James L. Skinner. Surface of liquid water: Three-body interactions and vibrational sum-frequency spectroscopy. *Journal of the American Chemical Society*, 133(27):10360–10363, July 2011.

[216] Igor V. Stiopkin, Himali D. Jayathilake, Andrey N. Bordenyuk, and Alexander V. Benderskii. Heterodyne-detected vibrational sum frequency generation spectroscopy. *Journal of the American Chemical Society*, 130(7): 2271–2275, February 2008. doi: 10.1021/ja076708w.

[217] Igor V. Stiopkin, Champika Weeraman, Piotr A. Pieniazek, Fadel Y. Shalhout, James L. Skinner, and Alexander V. Benderskii. Hydrogen bonding at the water surface revealed by isotopic dilution spectroscopy. *Nature*, 474(7350): 192–195, June 2011. doi: 10.1038/nature10173.

[218] Wei Hua, Aaron M. Jubb, and Heather C. Allen. Electric field reversal of na(2)so(4), (nh(4))(2)so(4), and na(2)co(3) relative to cacl(2) and nacl at the air/aqueous interface revealed by heterodyne detected phase-sensitive sum frequency. *Journal of Physical Chemistry Letters*, 2(20):2515–2520, October 2011. doi: 10.1021/jz200888t.

[219] Hidekazu Watanabe, Shoichi Yamaguchi, Sobhan Sen, Akihiro Morita, and Tahei Tahara. "half-hydration" at the air/water interface revealed by heterodyne-detected electronic sum frequency generation spectroscopy, polarization second harmonic generation, and molecular dynamics simulation. *Journal of Chemical Physics*, 132(14):144701, April 2010. doi: 10.1063/1.3372620.

[220] Satoshi Nihonyanagi, Tatsuya Ishiyama, Touk-kwan Lee, Shoichi Yamaguchi, Mischa Bonn, Akihiro Morita, and Tahei Tahara. Unified molecular view of the air/water interface based on experimental and theoretical chi((2)) spectra of an isotopically diluted water surface. *Journal of the American Chemical Society*, 133(42):16875–16880, October 2011. doi: 10.1021/ja2053754.

[221] Yuki Nagata and Shaul Mukamel. Vibrational sum-frequency generation spectroscopy at the water/lipid interface: Molecular dynamics simulation study. *Journal of the American Chemical Society*, 132(18):6434–6442, May 2010. doi: 10.1021/ja100508n.

[222] C. J. Tainter, P. A. Pieniazek, Y. . S. Lin, and J. L. Skinner. Robust three-body water simulation model. *Journal of Chemical Physics*, 134(18): 184501, May 2011. doi: 10.1063/1.3587053.

[223] J. Marti, E. Guardia, and J. A. Padro. Dielectric-properties and infrared-spectra of liquid water - influence of the dynamic cross correlations. *Journal of Chemical Physics*, 101(12):10883–10891, December 1994.

[224] J. Marti, J. A. Padro, and E. Guardia. Molecular-dynamics calculation of the infrared-spectra in liquid h2o-d2o mixtures. *Journal of Molecular Liquids*, 62: 17–31, November 1994. doi: 10.1016/0167-7322(94)00769-1.